Title

Zika Virus Targets Glioblastoma Stem Cells through a SOX2-Integrin αvβ5 Axis



Journal

Cell Stem Cell, 26(2)

ISSN

1934-5909

Authors

Zhu, Zhe

Mesci, Pinar

Bernatchez, Jean A

et al.

Publication Date

2020-02-01

DOI

10.1016/j.stem.2019.11.016

Peer reviewed

Article

Cell Stem Cell

# Zika Virus Targets Glioblastoma Stem Cells through a SOX2-Integrin $\alpha_v\beta_5$ Axis

## Graphical Abstract

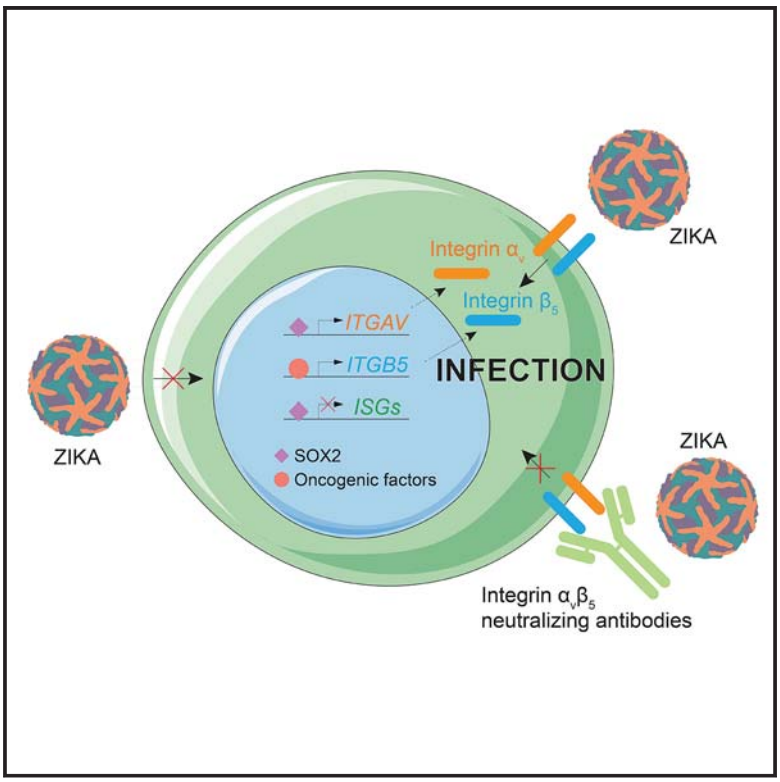


## Highlights

- ZIKV preferentially infects glioblastoma stem cells (GSCs) rather than neural precursor cells
- ZIKV kills SOX2$^+$ cells from a diverse array of malignant brain tumors
- SOX2 determines susceptibility to ZIKV infection with reduced antiviral responses
- Integrin $\alpha_v\beta_5$ is a GSC marker and promotes Zika virus infection of GSCs

## Authors

Zhe Zhu, Pinar Mesci, Jean A. Bernatchez, ..., Alysson R. Muotri, David A. Cheresh, Jeremy N. Rich

## Correspondence

jairlage@ucsd.edu (J.L.S.-N.), muotri@ucsd.edu (A.R.M.), dcheresh@ucsd.edu (D.A.C.), drjeremyrich@gmail.com (J.N.R.)

## In Brief

Zika virus causes microcephaly by killing neural precursor cells but also acts as an oncolytic virus against glioblastoma. Zika preferentially targets glioblastoma stem cells through core stem cell transcription factor downregulation of innate immunity and induction of internalization through an integrin heterodimer that marks cancer stem cells.

Zhu et al., 2020, Cell Stem Cell *26*, 187–204
February 6, 2020 
https://doi.org/10.1016/j.stem.2019.11.016

CellPress

Cell Stem Cell
Article

# Zika Virus Targets Glioblastoma Stem Cells through a SOX2-Integrin $\alpha_v\beta_5$ Axis

Zhe Zhu,[1,2,20] Pinar Mesci,[2,3,4,20] Jean A. Bernatchez,[5] Ryan C. Gimple,[1,2,6,7] Xiuxing Wang,[1,2] Simon T. Schafer,[8] Hiromi I. Wettersten,[2,9] Sungjun Beck,[5] Alex E. Clark,[10] Qiulian Wu,[1,2] Briana C. Prager,[1,2,6,7,11] Leo J.Y. Kim,[1,6,7] Rekha Dhanwani,[12] Sonia Sharma,[12] Alexandra Garancher,[13] Sara M. Weis,[2,9] Stephen C. Mack,[14] Priscilla D. Negraes,[2,3] Cleber A. Trujillo,[2,3] Luiz O. Penalva,[15] Jing Feng,[16] Zhou Lan,[16] Rong Zhang,[17] Alex W. Wessel,[17] Sanjay Dhawan,[18] Michael S. Diamond,[17] Clark C. Chen,[18] Robert J. Wechsler-Reya,[13] Fred H. Gage,[8] Hongzhen Hu,[16] Jair L. Siqueira-Neto,[4,*] Alysson R. Muotri,[2,3,*] David A. Cheresh,[9,*] and Jeremy N. Rich[1,2,19,21,*]

[1]Department of Medicine, Division of Regenerative Medicine, University of California School of Medicine, San Diego, La Jolla, CA 92037, USA
[2]Sanford Consortium for Regenerative Medicine, 2880 Torrey Pines Scenic Drive, La Jolla, CA 92037, USA
[3]Department of Pediatrics, Rady Children's Hospital San Diego, School of Medicine, University of California, San Diego, La Jolla, CA 92307, USA
[4]Department of Cellular and Molecular Medicine, Stem Cell Program, School of Medicine, University of California, San Diego, La Jolla, CA 92307, USA
[5]Center for Discovery and Innovation in Parasitic Diseases, Skaggs School of Pharmacy and Pharmaceutical Sciences, University of California, San Diego, La Jolla, CA 92037, USA
[6]Case Western Reserve University Medical Scientist Training Program, Case Western Reserve University School of Medicine, Cleveland, OH 44106, USA
[7]Department of Pathology, Case Western Reserve University School of Medicine, Cleveland, OH 44106, USA
[8]Laboratory of Genetics, Salk Institute for Biological Studies, 10010 North Torrey Pines Road, La Jolla, CA 92037, USA
[9]Department of Pathology, Moores Cancer Center, University of California, San Diego, La Jolla, CA 92037, USA
[10]Department of Cellular and Molecular Medicine and Skaggs School of Pharmacy and Pharmaceutical Sciences, University of California, San Diego, La Jolla, CA 92037, USA
[11]Cleveland Clinic Lerner College of Medicine, Cleveland Clinic, Cleveland, OH 44195, USA
[12]La Jolla Institute for Allergy and Immunology, 9420 Athena Circle, La Jolla, CA 92037, USA
[13]Tumor Initiation and Maintenance Program, NCI-Designated Cancer Center, Sanford Burnham Prebys Medical Discovery Institute, La Jolla, CA 92037, USA
[14]Department of Pediatrics, Baylor College of Medicine, Texas Children's Hospital, Houston, TX 77030, USA
[15]Children's Cancer Research Institute – UTHSCSA, San Antonio, TX 78229, USA
[16]Department of Anesthesiology, Center for the Study of Itch, Washington University School of Medicine in St. Louis, St. Louis, MO 63130, USA
[17]Departments of Medicine, Molecular Microbiology, Pathology, and Immunology and The Andrew M. and Jane M. Bursky Center for Human Immunology and Immunotherapy Programs, Washington University School of Medicine, St. Louis, MO 63130, USA
[18]Department of Neurosurgery, University of Minnesota, Minneapolis, MN 55455, USA
[19]Department of Neurosciences, University of California, San Diego, School of Medicine, La Jolla, CA 92037, USA
[20]These authors contributed equally
[21]Lead Contact
*Correspondence: jairlage@ucsd.edu (J.L.S.-N.), muotri@ucsd.edu (A.R.M.), dcheresh@ucsd.edu (D.A.C.), drjeremyrich@gmail.com (J.N.R.)
https://doi.org/10.1016/j.stem.2019.11.016

## SUMMARY

Zika virus (ZIKV) causes microcephaly by killing neural precursor cells (NPCs) and other brain cells. ZIKV also displays therapeutic oncolytic activity against glioblastoma (GBM) stem cells (GSCs). Here we demonstrate that ZIKV preferentially infected and killed GSCs and stem-like cells in medulloblastoma and ependymoma in a SOX2-dependent manner. Targeting SOX2 severely attenuated ZIKV infection, in contrast to AXL. As mechanisms of SOX2-mediated ZIKV infection, we identified inverse expression of antiviral interferon response genes (ISGs) and positive correlation with integrin $\alpha_v$ (ITGAV). ZIKV infection was disrupted by genetic targeting of ITGAV or its binding partner ITGB5 and by an antibody specific for integrin $\alpha_v\beta_5$. ZIKV selectively eliminated GSCs from species-matched human mature cerebral organoids and GBM surgical specimens, which was reversed by integrin $\alpha_v\beta_5$ inhibition. Collectively, our studies identify integrin $\alpha_v\beta_5$ as a functional cancer stem cell marker essential for GBM maintenance and ZIKV infection, providing potential brain tumor therapy.

## INTRODUCTION

Glioblastoma (GBM) ranks among the most lethal of all human cancers, with current therapies offering only palliation (Stupp et al., 2005). Replication-competent oncolytic viruses have been employed against GBM and other types of brain cancer (Foreman et al., 2017). Oncolytic viruses may offer selective targeting, internalization, and killing of tumor cells while sparing

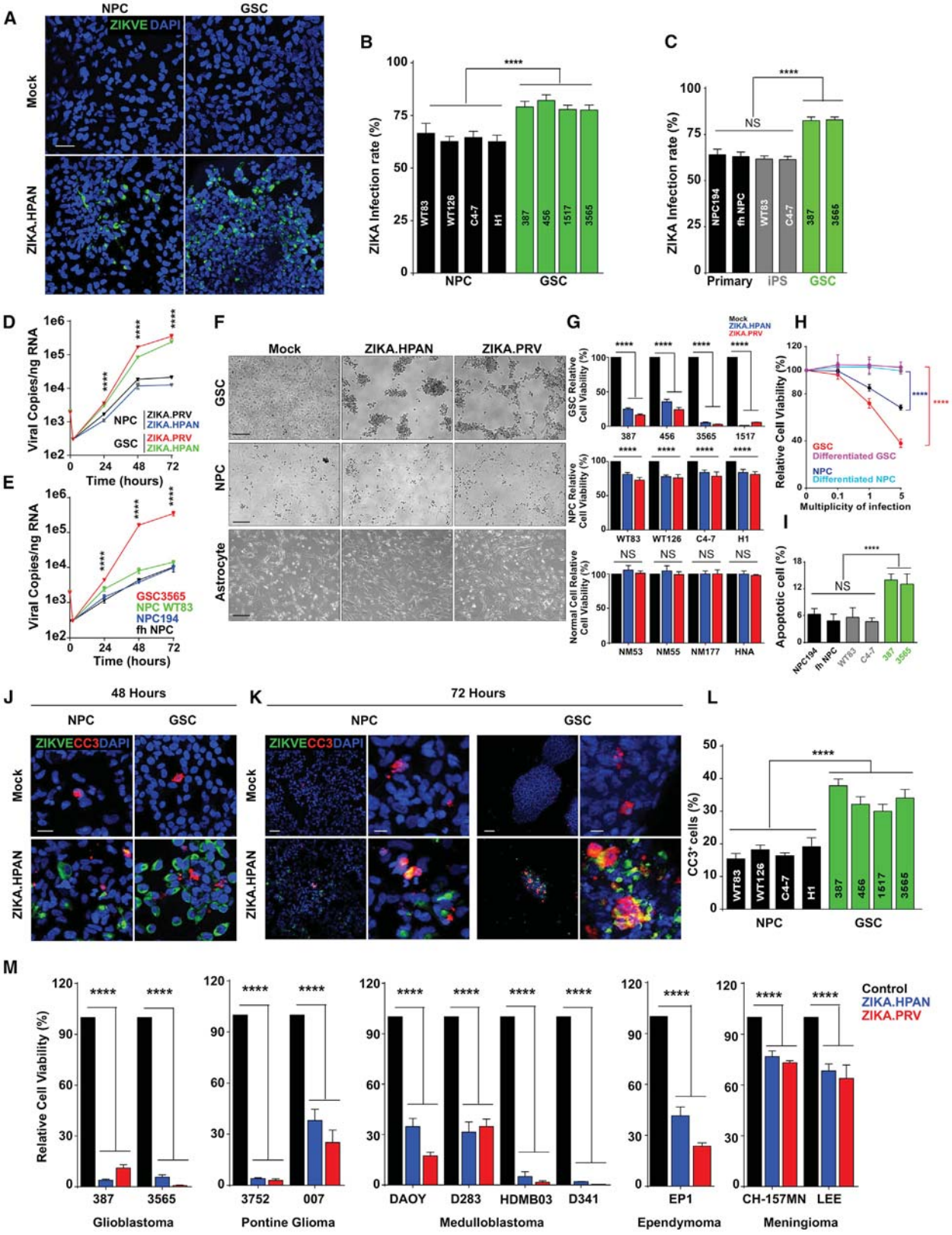


(legend on next page)

normal tissues. Because GBM cells are highly invasive, preventing complete surgical resection and cure, neurotropic viruses can target cells protected from chemotherapy and other systemic therapies by the blood-brain barrier. Several oncolytic viruses have been investigated in preclinical and clinical trials for brain tumors (Russell et al., 2012). GBMs contain self-renewing, highly tumorigenic stem-like cells, called GBM stem cells (GSCs), that display preferential therapeutic resistance, invasion into normal brain tissue, stimulation of neoangiogenesis, and tumor immune escape (Singh et al., 2003; Bao et al., 2006b; Wu et al., 2010; Bach et al., 2013). Previous studies have suggested that oncolytic viruses can be engineered to target GSCs (Wakimoto et al., 2009; Allen et al., 2013; Bach et al., 2013; Zemp et al., 2013; Josupeit et al., 2016). Thus, we hypothesized that an oncolytic virus targeting effort could be optimized by leveraging neurotropic viruses that preferentially target specific cell types, such as neural precursor cells (NPCs).

In 2015, a Zika virus (ZIKV) epidemic in Central and South America became a global health emergency (Heymann et al., 2016) following a dramatic increase in the number of newborns with microcephaly and other congenital anomalies (Nowakowski et al., 2016; Oliveira Melo et al., 2016; Schuler-Faccini et al., 2016). Infected adults are often asymptomatic, whereas ZIKV infection of pregnant mothers can be associated with developmental and neurological disorders in subsequent live births (Petersen et al., 2016). The neurotropism and neurovirulence of ZIKV have been appreciated in model systems, confirming a causal link between ZIKV and birth defects (Lazear et al., 2016; Li et al., 2016; Miner et al., 2016). Numerous studies have shown that different cell populations in the nervous and immune systems are differentially susceptible to ZIKV infection (Retallack et al., 2016; Tang et al., 2016; Foo et al., 2017; Michlmayr et al., 2017; Oh et al., 2017; Zhu et al., 2017; Chen et al., 2018a; Mesci et al., 2018). One challenge in predicting the tropism of ZIKV has been the lack of a consistent molecular pathway mediating cellular infection of ZIKV. AXL has been proposed to mediate ZIKV infection of astrocytes but not NPCs via bridging by its natural ligand, Gas6 (Meertens et al., 2017), but AXL may have only indirect effects on ZIKV infection of astrocytes because of its role in modulating antiviral immunity (Chen et al., 2018a). To date, the identity of the ZIKV entry factor remains controversial (Nowakowski et al., 2016; Wells et al., 2016; Chen et al., 2018a).

We recently reported that ZIKV selectively kills patient-derived GSCs compared with differentiated GBM cells (DGCs) in culture, tumor organoids, and slice cultures (Zhu et al., 2017). These observations have been confirmed by others (Kaid et al., 2018; Chen et al., 2018b). Although the use of wild-type ZIKV is unlikely to be directly translated into clinical use for GBM patients, we hypothesized that interrogating the molecular mechanisms of ZIKV in GSCs could not only improve the potential application of future modified ZIKV in neuro-oncology but also elucidate mechanisms by which ZIKV gains entry into brain cells.

## RESULTS

### ZIKV Preferentially Infects and Kills Brain Tumor Stem Cells

To determine the potential of ZIKV to achieve preferential anti-tumor efficacy against GSCs with limited toxicity for normal brain, we compared ZIKV infection of GSCs with human NPCs derived from either induced pluripotent stem cells (iPSCs) or primary tissues. ZIKV preferentially infected patient-derived GSCs, as quantified by both detection of ZIKV envelope protein (ZIKV-E) (Figures 1A–1C) and viral RNA (Figures 1D and 1E). Although the infection of GSCs was moderately higher than that of normal NPCs, ZIKV induced greater cell death in GSCs (Figures 1F–1I). ZIKV reduced GSC numbers through induction of apoptotic cell death and reduced proliferation (Figures 1J–1L, S1M, and S1N). These results were validated in a panel of 5 GSCs and 5 NPCs from different genetic backgrounds (Figures S1A–S1I and S1N). Although NPCs were less sensitive to ZIKV than GSCs, NPCs were killed by ZIKV, but over a longer time course than GSCs (Figures S1J–S1L and S1N), associated with mildly lower apoptosis (Figure S1O) and induction of differentiation (Figures S1O and S1P).

GBMs represent the brain cancer for which the tumor hierarchy is most clearly delineated, but other brain tumors, especially pediatric brain tumors, contain stem-like tumor cells (Bao et al., 2006a; Mack et al., 2018). We interrogated the anti-tumor efficacy of ZIKV against 2 pediatric pontine gliomas, 4

**Figure 1. Zika Virus (ZIKV) Infects and Kills GBM Stem Cells (GSCs) More Efficiently Than Neural Precursor Cells (NPCs)**

(A) Representative immunostaining for ZIKV envelope protein (ZIKV-E, green) and DAPI (blue) of GSCs and forebrain-specific NPCs 48 h post-infection (p.i.) with ZIKV. Scale bar, 50 μm.

(B) Quantification of infection efficiency in four GSC and NPC lines 48 h p.i. with ZIKV.

(C) Quantification of $ZIKV^+$ cells in a panel of human GSCs and NPCs.

(D) Kinetics of viral RNA copies p.i. with ZIKV by measuring viral RNA copies by qRT-PCR in NPC C4-7 and GSC3565.

(E) ZIKV infection efficiency of GSCs and NPCs was measured by direct measurement of viral RNA copies.

(F) Representative bright-field images 5 days p.i. with ZIKV for GSCs, NPCs, and primary astrocytes. Scale bars, 50 μm.

(G) Cell viability normalized to day 5 mock, as measured 5 days p.i. with ZIKV for GSCs, NPCs, and primary astrocytes.

(H) GSCs (GSC3565), differentiated GSCs, NPCs (NPC C4-7), and differentiated NPCs were assayed for cell viability 72 h p.i. with ZIKV.

(I) Apoptosis of GSCs (387, 3565) and primary (NPC194, fetal human [fh] NPC) or iPSC-derived NPCs (WT83, C4-7) p.i. with ZIKV was measured by cleaved caspase-3 (CC3) staining.

(J) Representative immunostaining for ZIKV-E (green), CC3 (red), and DAPI (blue) of GSCs and forebrain-specific NPCs 48 h p.i. with ZIKV. Scale bar, 50 μm.

(K) Representative immunostaining for ZIKV-E (green), CC3 (red), and DAPI (blue) of GSCs and forebrain-specific NPCs 72 h p.i. with ZIKV. Scale bars, 50 μm.

(L) Quantification of the percentage of $CC3^+$ cells in $DAPI^+$ cells for GSCs and NPCs 72 h p.i. with ZIKV.

(M) Cell viability of patient-derived cultures from GBM (387 and 3565), pontine glioma (3752 and 007), meningioma (CH-157MN, IOMM-LEE), ependymoma (EP1), and medulloblastoma cell lines (DAOY, D283, HDMB03, D341) 72 h after ZIKV infection.

Experiments were performed in two biological replicates with three technical repeats. Values represent mean ± SEM. NS, no significance. ****$p < 0.0001$ by one-way ANOVA.

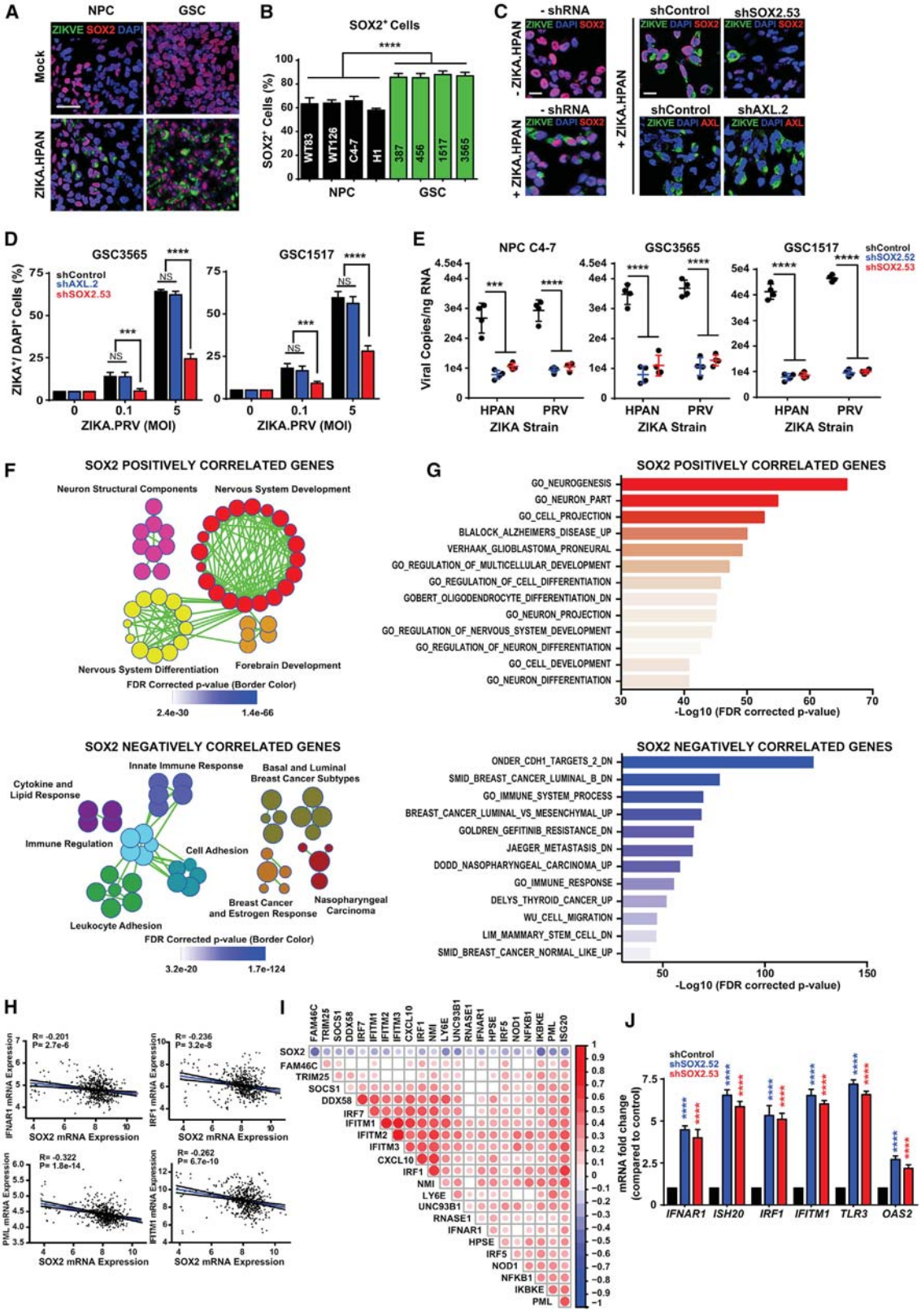


*(legend on next page)*

medulloblastomas, an ependymoma, and 2 meningiomas grown under serum-free conditions to enrich for stem-like populations (Wang et al., 2017a). For all models except meningiomas, ZIKV induced apoptotic cell death (Figures 1M and S2A–S2C). Unlike the other tumor types tested, meningioma is not intrinsic to the brain parenchyma; it is posited to arise from the arachnoid granulations (Buetow et al., 1991). Collectively, these results establish preferential ZIKV killing of stem-like brain tumor cells, supporting its potential utility as a platform for an oncolytic virus.

## SOX2 Modulates Infection of GSCs Associated with Repression of Innate Antiviral Responses

To define the molecular determinants of ZIKV infection of GSCs, we investigated a core regulator of GSCs reported to mark NPCs infected by ZIKV, SOX2 (Souza et al., 2016). SOX2 is an SRY-box transcription factor that is expressed at high levels during neural development and contributes to induced pluripotency (Sarkar and Hochedlinger, 2013). GSCs express high levels of SOX2, and targeting SOX2 expression attenuates GSC maintenance (Gangemi et al., 2009). Nearly all ZIKV-infected NPCs and GSCs were $SOX2^+$, and most $SOX2^+$ cells were infected by ZIKV (Figures 2A and 2B). The fraction of ZIKV-infected cells mirrored the fraction of $SOX2^+$ cells in other brain tumor types (Figures S2D and S2E); meningioma cultures had both the lowest fraction of $SOX2^+$ cells and ZIKV infection. GSCs expressed higher levels of SOX2 than NPCs by immunoblot (Figure S2F).

To address the functional role of SOX2 in ZIKV infection, we targeted SOX2 expression using two non-overlapping short hairpin RNAs (designated shSOX2.52 and shSOX2.53) relative to a control short hairpin RNA (shRNA) sequence designed to avoid targeting any sequence in the mammalian genome (shCONT) (Figure S2G). Consistent with its role in GSC maintenance, targeting SOX2 expression induced expression of the differentiation marker GFAP (Figure S2G). GSCs transduced with shCONT retained their ability to be infected by ZIKV, as measured by both ZIKV-E protein and RNA, whereas GSCs transduced with shSOX2 showed attenuated ZIKV infectivity (Figures 2C–E). Although AXL is a putative ZIKV receptor (Nowakowski et al., 2016), we did not observe differential ZIKV infection following AXL knockdown, suggesting that AXL is dispensable for ZIKV infection of GSCs (Figures 2C, 2D, and S2H). Moreover, in GBM surgical specimens, the majority of $AXL^+$ cells were $GFAP^+$, not $SOX2^+$, suggesting that SOX2 and AXL mark discrete tumor populations (Figures S2I and S2J).

SOX2 exerts many of its effects through transcriptional regulation of gene targets. To focus our efforts on mediators of ZIKV infection, we interrogated The Cancer Genome Atlas (TCGA) GBM database for genes that correlated with *SOX2* mRNA expression. *SOX2* positively correlated with genes involved in nervous system development and neuronal structural components, whereas *SOX2* negatively correlated with genes of the innate immune response and regulation (Figures 2F and 2G). Because suppression of cell-intrinsic innate immune responses can render cells susceptible to viral infection, we interrogated the relationship between SOX2 mRNA expression and mediators of the interferon-stimulated gene (ISG) family. *SOX2* mRNA consistently negatively correlated with ISGs in GBM (Figures 2H, 2I, and S3A). Silencing SOX2 induced ISG expression, supporting SOX2 regulation of antiviral cellular responses (Figures 2J and S3B). To determine whether these changes in ISGs were biologically relevant, we examined ISG levels in GSCs treated with increasing concentrations of type I interferon (Figure S3C). The inverse relationship between SOX2 and ISGs in GSCs contrasts with normal stem cells, where ISGs are highly expressed (Wu et al., 2018), suggesting that SOX2 function differs between normal and neoplastic stem cells.

## SOX2 Regulates Integrin $\alpha_v$ Expression in GSCs

SOX2 suppression of the innate antiviral response provides one mechanism by which its expression correlates with ZIKV infection. We hypothesized that SOX2 also may regulate the expression of molecules involved in the primary infection process, based on the rapid decrease in ZIKV infection after SOX2 targeting, so we interrogated the TCGA GBM database for associations between *SOX2* mRNA, expression of other GSC markers, and possible ZIKV receptors, including the TAM receptors (*TYRO3*, *AXL*, and *MERTK*) and several integrins, which may serve as attachment factors for West Nile virus and other flaviviruses (Chu and Ng, 2004; Meertens et al., 2017; Figure 3A). *AXL*

**Figure 2. SOX2 Mediates Infection of GSCs Associated with Repression of Innate Antiviral Responses**

(A) Representative immunostaining for ZIKV-E (green), SOX2 (red), and DAPI (blue) of GSCs and forebrain-specific hiPSC-derived NPCs 48 h p.i. with ZIKV. Scale bar, 50 μm.

(B) Quantification of the percentage of $SOX2^+$ cells in $DAPI^+$ cells for GSCs and NPCs 48 h p.i. with ZIKV.

(C) Representative immunostaining for ZIKV-E (green), SOX2 or AXL (red), and DAPI (blue) of GSCs (GSC3565) without transduction (shRNA) or transduced with control shRNA (shCONT), AXL shRNA (shAXL.2), or SOX2 shRNA (shSOX2.53) for 72 h and then 48 h with ZIKV infection. Scale bars, 100 μm.

(D) Quantification of the percentage of $ZIKV^+$ cells in $DAPI^+$ cells in GSCs 1517 and 3565 under conditions for (C), with a range of ZIKV infection.

(E) Viral copy number by qRT-PCR of GSCs (GSC3565 or GSC1517) or NPC C4-7 transduced with either shCONT or SOX2 shRNA (shSOX2.52 or shSOX2.53) for 72 h and then either exposed to mock conditions or infected with ZIKV for another 72 h. All comparisons are versus shCONT.

(F) Gene set enrichment (GSE) bubble plots showing pathways positively (top, $r > 0.4$) or negatively (bottom, $r < -0.4$) correlated with *SOX2* expression in the TCGA GBM HG-U133A microarray dataset. Each circle represents an enriched pathway, with the border color indicating the false discovery rate (FDR)-corrected p value.

(G) GSE graph showing the top pathway enrichments positively or negatively correlated with *SOX2* as described in (F).

(H) Correlation of mRNA levels of SOX2 with IFNAR1, IRF1, promyelocytic leukemia (PML), and IFITIM1 from the TCGA GBM HG-U133A microarray dataset.

(I) Correlation between *SOX2* with ISGs from the TCGA GBM HG-U133A microarray dataset. The size and color of the dots indicate the degree of correlation ($p < 0.001$). Blank cells indicate a non-significant correlation.

(J) qPCR of ISGs (*IFNAR-1*, *ISH20*, *IRF1*, *IFITM1*, *TLR3*, and *OAS2*) in GSCs (GSC3565) transduced with either shCONT or SOX2 shRNA (shSOX2.52 or shSOX2.53).

Experiments were performed in two biological replicates with three technical repeats. Values represent mean ± SEM. $^{**}p < 0.001$, $^{****}p < 0.0001$ by one-way ANOVA.

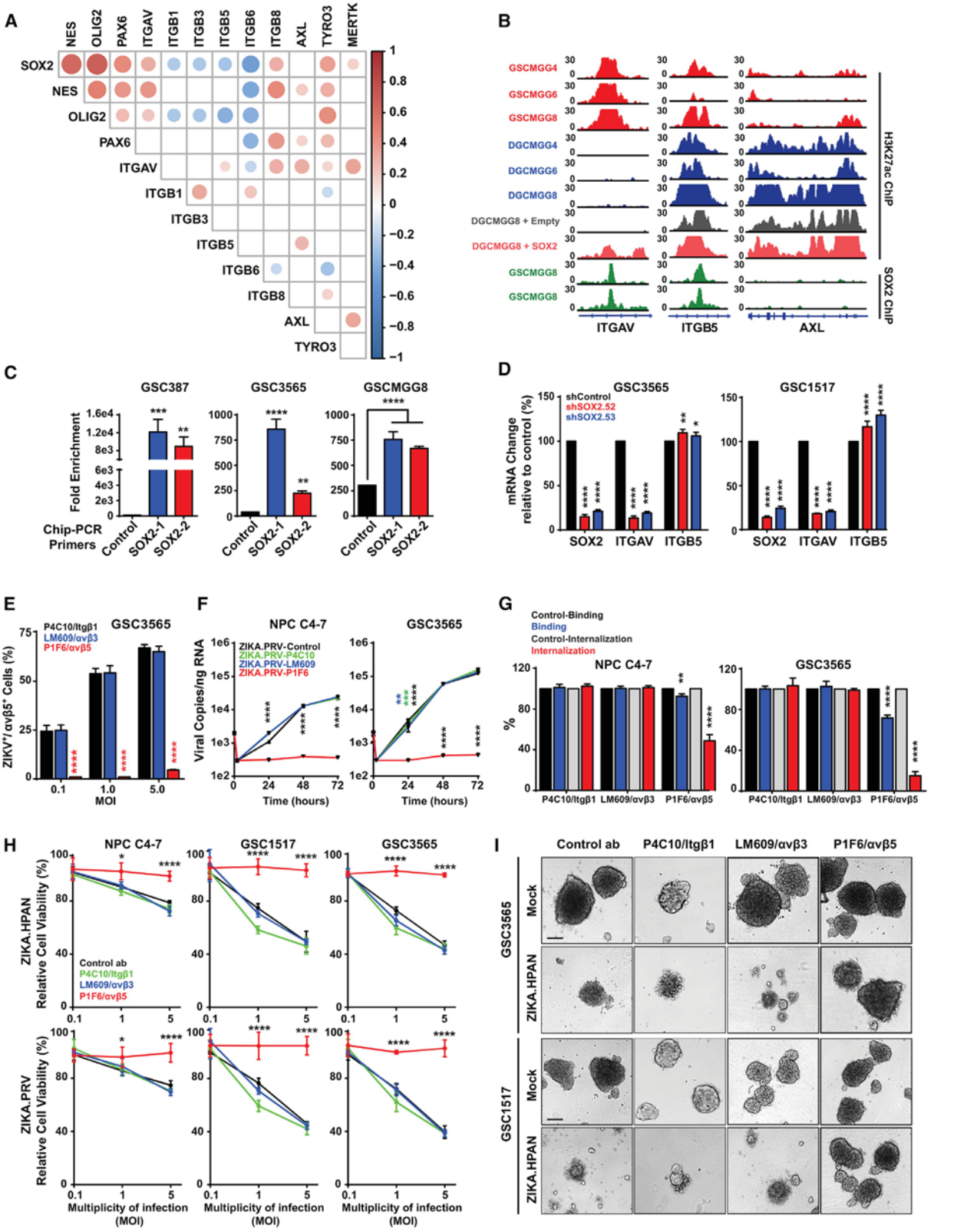


(legend on next page)

and *SOX2* expression were not correlated, whereas the mRNA levels of integrin $\alpha_v$ (*ITGAV*) correlated with *SOX2* and other GSC markers (*NES*, *PAX6*, and *OLIG2*) (Figures 3A and S4A). Because SOX2 is a transcription factor, we investigated SOX2 regulation of ITGAV. Measurement of active chromatin through histone 3 lysine 27 acetyl chromatin immunoprecipitation followed by deep sequencing (H3K27ac ChIP-seq) of GSCs and DGCs revealed activation of the ITGAV locus in GSCs, whereas the AXL locus was more activated in DGCs (Suvà et al., 2014; Figure 3B); these data were consistent with the immunofluorescence staining of GBMs (Figure S2I). SOX2 bound within the *ITGAV* locus by ChIP-seq, and its binding was associated with an increase in the active chromatin mark H3K27ac at this locus (Figure 3B). ChIP-PCR of SOX2 on the *ITGAV* locus in a set of GSCs confirmed SOX2 binding (Figure 3C). Gene silencing of SOX2 using either of two non-overlapping shRNAs showed reduced ITGAV expression but not that of another integrin subunit, *ITGB5*, as measured by mRNA levels, immunohistochemistry, and immunoblotting (Figures 3D, S4B, and S4C). Collectively, these results demonstrate that SOX2 regulates ITGAV expression in GSCs.

## Blockade of $\alpha_v\beta_5$ Integrin Reduces ZIKV Infection in GSCs

The integrin $\alpha_v$ subunit forms heterodimers with one of five different β subunits ($\beta_1$, $\beta_3$, $\beta_5$, $\beta_6$, or $\beta_8$) to mediate its binding to matrix ligands and promote intracellular signaling, adhesion, cell migration, and cell proliferation (Desgrosellier and Cheresh, 2010). To determine whether any of the integrin heterodimers were involved in ZIKV infection, we screened a panel of function-blocking antibodies against different integrins—pan-$\beta_1$ (P4C10), $\alpha_v\beta_3$ (LM609), and $\alpha_v\beta_5$ (P1F6)—for the capacity to prevent viral infection. Although blocking antibodies against $\beta_1$ and $\alpha_v\beta_3$ integrins had limited effect on ZIKV infection of NPCs or GSCs, as measured by ZIKV-E staining (Figures 3E and S4D) or ZIKV RNA levels (Figure 3F), blockade of $\alpha_v\beta_5$ integrin substantially reduced viral infection (Figures 3E, 3F, and S4D–S4G). Although blocking antibodies against $\beta_1$ and $\alpha_v\beta_3$ integrins did not alter surface binding or internalization of ZIKV to GSCs, a blocking antibody against integrin $\alpha_v\beta_5$ reduced ZIKV internalization to a greater extent than cell binding (Figure 3G). We assessed the effects of antibody blocking of integrins on ZIKV killing of NPCs and GSCs. With blocking antibodies against $\beta_1$ or $\alpha_v\beta_3$ integrins, we observed similarly reduced cellular viability with increasing multiplicity of infection (MOI) compared with a control antibody (Figure 3H). In contrast, a blocking antibody against $\alpha_v\beta_5$ integrin attenuated ZIKV-mediated cell death in both NPCs and GSCs (Figures 3H, S4H, and S4I). The $\alpha_v\beta_5$ integrin-blocking antibody also attenuated ZIKV effects on sphere formation under serum-free conditions (Figure 3I).

Brain organoids are complex, three-dimensional structures that self-organize and provide models that share features with normal and neoplastic brain tissues (Drost and Clevers, 2018); they have proven useful for studying viral infections (Zhou et al., 2018), including ZIKV (Garcez et al., 2016; Qian et al., 2016). We recently reported GBM organoids as a system for investigating the basis of GBM heterogeneity (Hubert et al., 2016). GBM organoids grow over time, as measured by organoid diameter (Figures S4K and S4L). Supporting a functional importance for $\alpha_v\beta_5$ integrin in GBM growth, tumor organoids incubated with an integrin $\alpha_v\beta_5$-blocking antibody were static or reduced in size over time. In contrast, tumor organoids infected with ZIKV were obliterated, an effect that was lost upon treatment with the $\alpha_v\beta_5$ integrin-blocking antibody (Figures S4K and S4L).

To determine whether GBMs preferentially express specific integrins, we interrogated the TCGA GBM dataset, which revealed that $\alpha_v$ and $\beta_1$, $\beta_3$, $\beta_5$, and $\beta_8$, but not $\beta_6$ integrin subunits, were overexpressed in GBM relative to normal brain (Figure 4A). The preferential expression of these integrins suggested that they might contribute to the specificity of ZIKV infection, so we silenced expression of the β subunits known to associate with integrin $\alpha_v$ ($\beta_1$, $\beta_3$, $\beta_5$, $\beta_6$, or $\beta_8$) using two non-overlapping shRNAs each (Figure 4B). Only silencing of integrin $\beta_5$ prevented killing of GSCs by ZIKV infection, as measured by cell viability (Figure 4C), sphere formation (Figure 4D), sphere size (Figure 4E), and ZIKV RNA copy number (Figure 4F). In complementary studies, we targeted ITGB3, ITGB5, and ITGAV using CRISPR/Cas9 gene editing (Figure S5A), revealing that ZIKV infection required ITGAV and ITGB5 but not ITGB3 (Figure S5B). We previously demonstrated that integrin $\alpha_6$ (ITGA6) is a functional GSC marker (Lathia et al., 2010). Targeting ITGAV by CRISPR/Cas9 did not change ITGA6

**Figure 3. SOX2 Regulates Integrin $\alpha_v$ in GSCs, and Integrin $\alpha_v\beta_5$ Mediates ZIKV Infection in GSCs**

(A) Correlation between *SOX2* mRNA expression with *ITGAV*, *Nestin* (*NES*), *PAX6*, *OLIG2*, *ITGB1*, *ITGB3*, *ITGB5*, *ITGB6*, *ITGB8*, *AXL*, *TYRO3*, and *MERTK* levels from the TCGA GBM HG-U133A microarray dataset. Size and color indicate the degree of correlation ($p < 0.001$), with blank cells indicating a non-significant correlation.

(B) ChIP-seq for H3K27ac or SOX2 at the *ITGAV*, *ITGB5*, and *AXL* loci in matched GSCs and DGCs and following SOX2 overexpression. Data were derived from GSE54792 and GSE17312.

(C) ChIP-PCR assessing SOX2 occupancy at the ITGAV locus with two distinct sequences (denoted SOX2-1 and SOX2-2) in three GSC lines (387, 3565, and MGG8).

(D) mRNA levels of *SOX2*, *ITGAV*, and *ITGB5* by qPCR for GSCs (GSC3565 or GSC1517) transduced with either shCONT or SOX2 shRNA (shSOX2.52 or shSOX2.53). p values indicate comparisons with shCONT.

(E) GSCs (GSC3565) were cultured with an IgG control antibody (LM142) or one of three neutralizing antibodies against integrins (Itg$\beta_1$, 4C10; $\alpha_v\beta_3$, LM609; $\alpha_v\beta_5$, P1F6; 50 μg/mL) and then exposed to mock conditions or infection with ZIKV. The fraction of GBM integrin $\alpha_v\beta_5^+$ cells was assessed by immunofluorescence 72 h p.i. with ZIKV.

(F) GSCs (GSC3565) or NPCs (C4-7) were cultured as in (E). The number of intracellular ZIKV viral particles was quantified by qRT-PCR.

(G) Quantification of viral RNA by qRT-PCR in (F) was performed to assess surface binding or internalization with normalization to the IgG control.

(H) GSCs (GSC3565) were cultured as in (E). Cell viability was assessed 72 h p.i. with ZIKV.

(I) Representative bright-field images of GSCs (GSC3565 and GSC1517) that were cultured as in (E). Scale bars, 50 μm.

Experiments were performed in two biological replicates with three technical repeats. Values represent mean ± SEM. *$p < 0.05$, **$p < 0.01$, ****$p < 0.0001$ by one-way ANOVA.

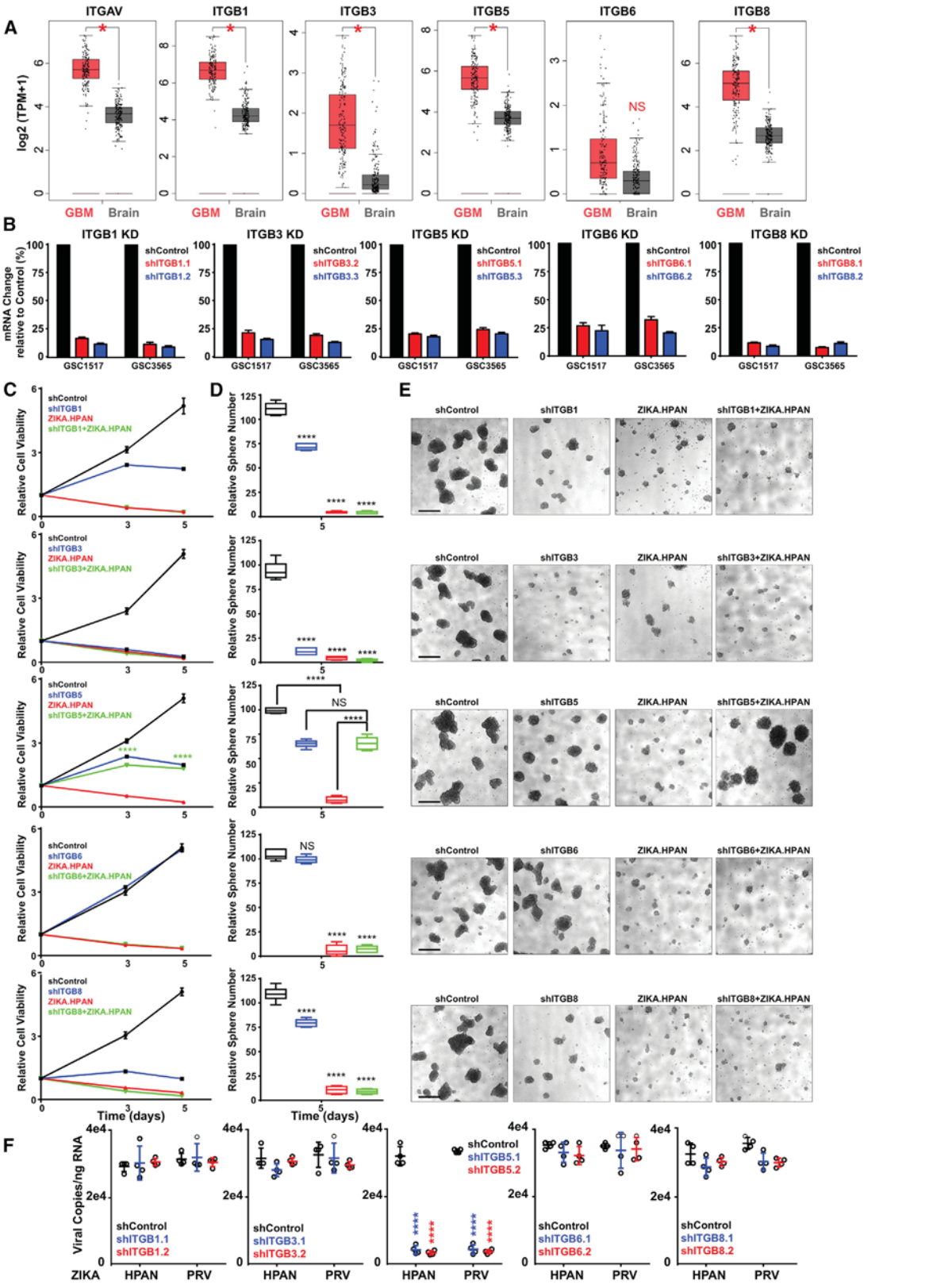


*(legend on next page)*

levels (Figures S5C and S5D). Targeting ITGA6 by CRISPR/Cas9 reduced ITGA6 expression and the number of GSCs, consistent with our previous study (Figures S5E–S5G). Although ITGA6 single-guide RNA (sgRNA) and ZIKV infection both targeted GSCs (Figure S5G), GSCs surviving loss of ITGA6 were not infected by ZIKV at higher rates, and ZIKV infection did not specifically deplete ITGA6$^+$ cells in surviving GSCs (Figures S5H and S5I), suggesting that ITGA6 is not essential for ZIKV infection of GSCs. Collectively, these results support a specific role for $\alpha_v\beta_5$ integrin in ZIKV infection and cellular killing.

### $\alpha_v\beta_5$ Integrin Maintains GSCs

To interrogate the role of integrin $\alpha_v\beta_5$ in GSCs, we leveraged a panel of H3K27ac profiles that we developed from primary GBM resection specimens (Wang et al., 2017b) and compared these with normal brain H3K27ac profiles derived from the Roadmap Epigenomics database (Figure 5A). The loci for *SOX2*, *ITGAV*, and *ITGB5* displayed more active chromatin states in GBM than non-neoplastic brain. AXL, in contrast, showed similar chromatin states between tumor and non-neoplastic tissues (Figure 5A). High *ITGB5* mRNA levels were associated with a poor prognosis in IDH1 wild-type GBM patients, with a particularly poor prognosis for patients with high levels of both *ITGAV* and *ITGB5* (Figure 5B). To further link SOX2 and $\alpha_v\beta_5$ integrin in GBM, we performed immunofluorescence for SOX2, $\alpha_v\beta_5$ integrin, and GFAP (a marker of differentiated cells) on surgical specimens from GBM and control brain tissue derived from epilepsy patients (Figure 5C). GBM tissues had more integrin $\alpha_v\beta_5^+$ cells than non-neoplastic brain, and the majority of SOX2$^+$, but not GFAP$^+$, cells expressed $\alpha_v\beta_5$ integrin (Figure 5D). CRISPR/Cas9 targeting of ITGAV with two distinct sgRNAs (sgITGAV) in GSCs reduced integrin $\alpha_v\beta_5$ protein expression, as measured by immunofluorescence, but not SOX2 expression, supporting that ITGAV is downstream of SOX2 (Figure 5E). As expected, GSCs transduced with sgITGAV had reduced surface expression of $\alpha_v\beta_5$ integrin (Figure 5F). Targeting ITGAV attenuated GSC viability (Figure 5G) and self-renewal, as measured by limiting dilution sphere formation (Figures 5H and 5I). Immunocompromised mice bearing two different GSCs transduced with one of two sgITGAVs survived longer and had reduced tumor growth compared to a control sgRNA (sgCONT) (Figures 5J and 5K). These results demonstrate that the cells targeted by ZIKV and marked by ITGAV expression are critical to tumor growth.

### ZIKV Induces Cellular Changes in Normal Mature Cerebral Organoids but Has Little Effect on Size

To avoid species differences between tumor and normal cells, we determined the relative effects of ZIKV infection on GBM and normal cerebral organoids. Mature brain cortical organoids (BCOs) from human pluripotent stem cells (Thomas et al., 2017; Trujillo et al., 2019) contain mature neurons from different layers (CTIP2, NeuN, SATB2, and MAP2$^+$ cells) and neuronal progenitors (SOX2$^+$) and glia (GFAP$^+$) (Figures 6A and S6A). ZIKV had little effect on the size of BCOs over time (Figures 6B, 6C, and S6B), but there was an increase in apoptotic cells and decrease in SOX2$^+$ cells (Figures 6D and 6E). ZIKV had little to no effect on the proportions of different neuronal and astrocytic cell types in cerebral organoids (Figures 6F–6I).

### Generation of Human GBM-Cerebral Organoid Models

To test the relative efficacy of ZIKV infection against human GBM relative to toxicity to normal human brain, we implanted human GBM tumors grown in mature (6-month-old) human BCOs. After 6 months, most NPCs differentiated into neurons and astrocytes (Thomas et al., 2017; Trujillo et al., 2019). Mimicking tumor growth, the GFP-GSCs invaded the BCOs and expanded over time (Figure 6J). The cerebral organoids alone without GSCs displayed substantially lower expression of $\alpha_v\beta_5$ integrin than the GBM organoids (Figures 6K and 6L). The GFP-GSCs preferentially expressed SOX2 and $\alpha_v\beta_5$ integrin relative to normal BCO cells (Figures 6M and 6N). These results demonstrate that fused GSC-BCOs preserve the differential expression profiles found in human tumors and normal brain and offer a platform to study human GBM.

### ZIKV Infection Preferentially Targets GSCs in GBM-BCOs

ZIKV infection of GBM-BCOs preferentially reduced GFP-GSCs (Figure 6O) and infected $\alpha_v\beta_5$ integrin$^+$ cells in combined GBM-BCOs, reducing the number of GFP-labeled tumor cells (Figures 6P and 6Q). In 2 patient-derived GSCs fused with human BCOs, ZIKV showed a potent anti-tumor effect over time (Figures S7A and S7B). We followed the number of GFP-GSCs by measuring the integrated density of GFP$^+$ cells (Figures S7A and S7B) and immunostaining of GFP$^+$ cells (Figures 6R and S7C); this showed preferential infection of GSCs by ZIKV and reduced cell numbers. Upon ZIKV infection, GFP-GSC-BCOs had an increased number of ZIKV-E$^+$ cells that were mainly seen in GFP$^+$ cells (Figures 6R and S7C). To rule out a contribution of GFP to the increased vulnerability of GFP-labeled GSCs to ZIKV infection, we generated GFP-BCOs by transducing iPSCs with a phosphoglycerate kinase (PGK) promoter-driven GFP lentivirus and then infected them with ZIKV (Figure S7D). ZIKV decreased the fraction of GFP$^+$ cells in GFP-GSC-BCOs, concomitant with GSC apoptosis (Figure S7E), but not the number of GFP$^+$ cells in GFP-BCOs

**Figure 4. ZIKV Infection of GSCs Requires Integrin $\beta_5$**

(A) Matched TCGA GBM and normal brain from the genotype-tissue expression (GTEx) dataset, showing the expression levels of selected integrins; log scale by Log2 (transcripts per million [TPM]+1). *p < 0.0001 (n = 163 samples for GBM, n = 207 samples for normal brain).

(B) mRNA expression of integrins following shRNA-mediated knockdown in two patient-derived GSCs (GSC1517 and GSC3565). Values were normalized to a non-targeting shCONT.

(C) Cell viability in GSC3565 on days 0, 3, and 5 following treatment with integrin-targeting shRNAs, ZIKV, or a combination.

(D) Quantification of the number of spheres formed by GSCs on day 5 following treatment with integrin-targeting shRNAs, ZIKV, or a combination.

(E) Representative images of spheres derived from GSC3565 (C and D). Scale bars, 100 μm.

(F) ZIKV infectivity assessed by qRT-PCR on patient-derived GSCs transduced with either shCONT or one of two non-overlapping shRNAs targeting integrin β subunits that paired with integrin $\alpha_v$.

Two biological replicates with three technical repeats were performed. Data presented as mean ± SEM. ****p < 0.0001 by one-way ANOVA.

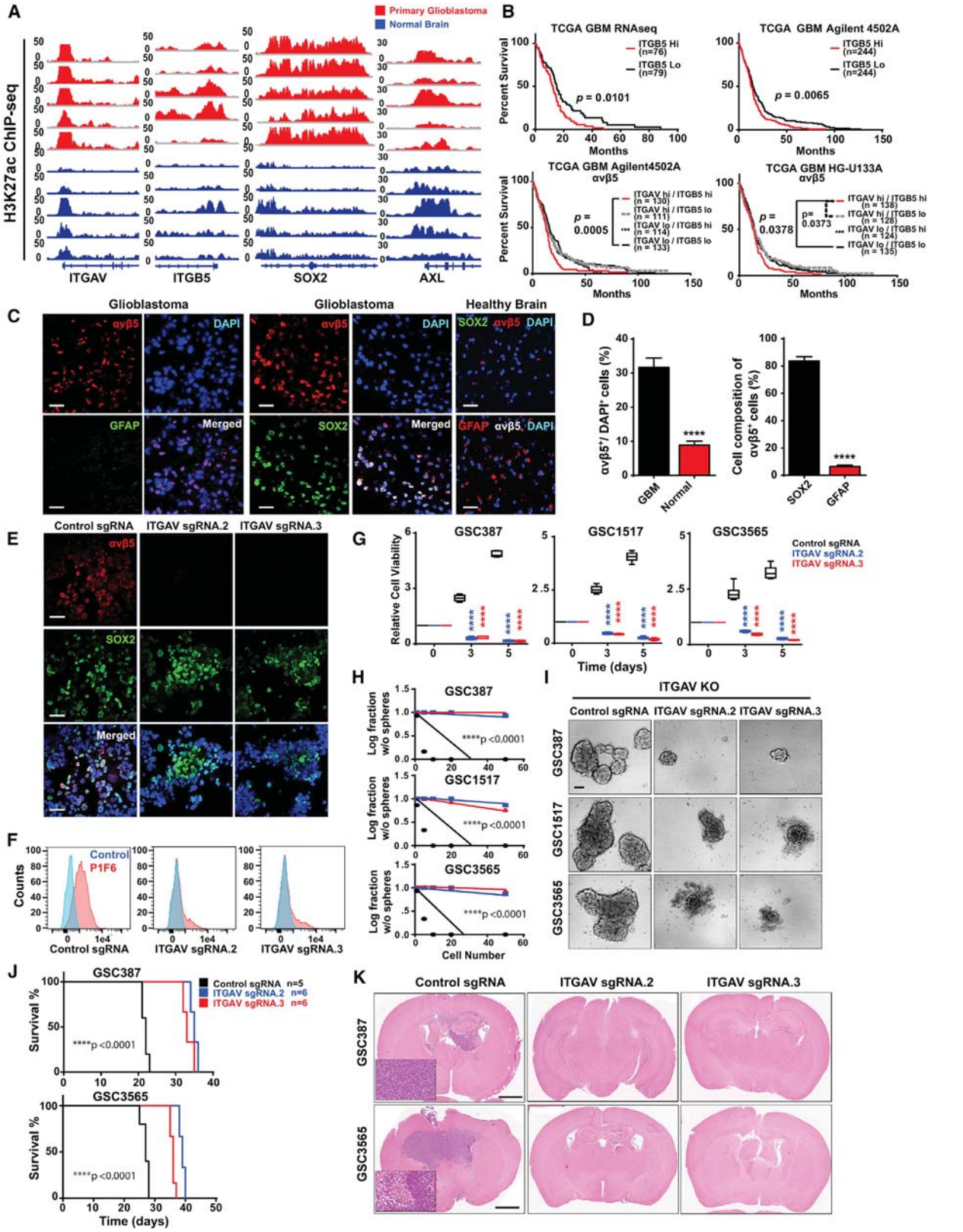


*(legend on next page)*

(Figure S7F), confirming that GSC vulnerability to ZIKV in GSC-BCOs is not due to the presence of GFP. Given the regulation of ISGs by SOX2 in cell culture, we interrogated our GBM-BCOs for immune responses after infection with ZIKV by performing targeted RNA sequencing using a Nanostring panel of 770 immune-related genes (Figure 6S). Upon infection with ZIKV, 113 genes were differentially expressed, including increased expression of several ISGs as well as inflammasome, adaptive immunity, antigen presentation, interferon (IFN) response, and Toll-like receptor (TLR) signaling pathways (Figure 6T and 6U), suggesting that organoids induce an immune response associated with elimination of GSCs by the virus. Collectively, these results confirm that ZIKV has oncolytic activity against GSCs and that this is associated with preferential expression of $\alpha_v\beta_5$ integrin in a fully humanized model system.

### ZIKV Does Not Induce Malignant Transformation in Normal Brain but Targets GSCs *In Vivo*

To address the potential for ZIKV induction of malignancy *in vivo*, we tested its toxicity on NPCs and the potential for oncogenic transformation of normal NPCs using 4- to 6-week-old immunocompromised mice (non-obese diabetic [NOD].Cg-*Prkdc*$^{scid}$ *Il2rg*$^{tm1Wjl}$/SzJl [NSG]). ZIKV ($10^3$ focus-forming units [FFU]/mouse of either the Human Panama [HPAN] or Puerto Rican isolate of ZIKV [PRVABC-59] [PRV] strains) was inoculated directly into the subventricular zone (SVZ). 72 h later, ZIKV infection of murine NPCs in the SVZ was confirmed through co-localization of ZIKV-E with the NPC marker SOX2 and $\alpha_v\beta_5$ integrin staining (Figures 7A and 7B). One month after ZIKV inoculation, the immunocompromised mice reached endpoint criteria (neurological signs), likely because of ZIKV virulence (Figure 7C). Analysis of ZIKV-infected brains revealed no gross morphological changes or evidence of malignancy (Figure 7D). These findings suggest that ZIKV induces neural toxicity *in vivo* in NSG mice but does not cause oncogenic transformation.

Previous reports from our laboratory and others have shown that ZIKV kills GSCs *in vivo* (Zhu et al., 2017; Kaid et al., 2018; Chen et al., 2018b). To assess the role of $\alpha_v\beta_5$ integrin in ZIKV-dependent oncolytic activity against GSCs *in vivo*, we used a tumor transplantation model in NSG mice and two complementary techniques: pharmacological inhibition with an integrin $\alpha_v\beta_5$-blocking antibody and genetic targeting of integrin $\beta_5$ expression using CRISPR/Cas9-based techniques. GSCs treated with an immunoglobulin G (IgG) control antibody had the shortest survival, whereas treatment with ZIKV extended the survival of tumor-bearing hosts (Figures 7E and 7F). Treatment of GSCs with an antibody targeting $\alpha_v\beta_5$ or gene editing of ITGB5 in the tumor attenuated Zika-mediated cytotoxicity and reduced host survival (Figures 7E and 7F). However, treatment with the $\alpha_v\beta_5$ integrin-blocking antibody extended the survival of tumor-bearing hosts in the absence of ZIKV treatment, which is consistent with the independent role of $\alpha_v\beta_5$ integrin in GSC maintenance. Collectively, these results support a role of integrin $\alpha_v\beta_5$ in ZIKV-dependent targeting of GSCs *in vivo*.

### Blocking $\alpha_v\beta_5$ Integrin Inhibits ZIKV Infection in Patient-Derived Tissues

Finally, to rule out possible effects of culture of tumors, we infected fresh intraoperative patient-derived GBM slices with ZIKV. To establish this model, we obtained freshly isolated primary human GBM slices and then incubated them with either an IgG control antibody or blocking integrin antibodies and infected them with ZIKV. Attenuation of ZIKV infection by $\alpha_v\beta_5$ integrin blockade was confirmed by staining for the ZIKV-E protein (Figure 7G) and quantifying the levels of ZIKV RNA (Figure 7H). These data support a dependence of $\alpha_v\beta_5$ integrin on ZIKV infection of GBM.

## DISCUSSION

Identification of molecular mediators of viral infection is important for antiviral and oncolytic virus strategies (Medigeshi et al., 2008; Brinton, 2013). Enrichment strategies for effective oncolytic therapy trials now include testing for expression of key determinants of viral infection in tumor tissues prior to patient enrollment. Here we demonstrate that SOX2 and integrin $\alpha_v\beta_5$ mark GSCs that are preferentially targeted by ZIKV in association with suppression of immune response genes and a molecular

**Figure 5. Integrin $\alpha_v\beta_5$ Maintains GSCs**

(A) H3K27ac ChIP-seq of primary GBM (red, n = 5 samples) and normal human brain (blue, n = 5 specimens) at the *ITGAV*, *ITGB5*, *SOX2*, and *AXL* loci.

(B) Kaplan-Meier survival curve of patients from the TCGA database. Patients were categorized into a "high" or "low" expression group based on the median mRNA expression of ITGB5 and integrin $\alpha_v\beta_5$ in RNA sequencing (RNA-seq), the Agilent 4502 microarray, or the HG-U133A microarray. The p values were calculated by log rank test.

(C) Immunostaining for integrin $\alpha_v\beta_5$ (red), GFAP (green), SOX2 (green), and DAPI (blue) of primary human GBM surgical biopsy specimens (n = 3) or normal human brain (n = 2). Scale bars, 100 μm.

(D) (Left) The fraction of DAPI$^+$ cells from Figure 4C that stained for integrin $\alpha_v\beta_5$. Right: the fraction of SOX2$^+$ and GFAP$^+$ cells in integrin $\alpha_v\beta_5^+$ GSCs. Values represent mean ± SEM. ****p < 0.0001 by two-tailed Student's t test.

(E) Representative immunostaining of GSCs (GSC3565) for integrin $\alpha_v\beta_5$ (red), SOX2 (green), and DAPI (blue) after transduction with either a sgCONT or one of two sgRNAs targeting ITGAV. Scale bars, 100 μm.

(F) Flow cytometry analysis for three patient-derived GSCs (GSC387, GSC1517, and GSC3565) transduced with either sgCONTor one of two sgRNAs targeting ITGAV following incubation with an IgG control antibody (LM142) or an integrin $\alpha_v\beta_5$ antibody (P1F6).

(G) Cell viability of three patient-derived GSCs (GSC387, GSC1517, and GSC3565) transduced with either sgCONT or one of two sgRNAs targeting ITGAVs normalized to day 0. Values represent mean ± SEM. ****p < 0.0001 by one-way ANOVA.

(H) Neurosphere formation of three patient-derived GSCs (GSC387, GSC1517, and GSC3565) transduced with either sgCONT or one of two sgRNAs targeting ITGAV. Values represent mean ± SEM. ****p < 0.0001 by extreme limiting dilution analysis (ELDA).

(I) Representative bright-field images of (H) at 5 days. Scale bar, 50 μm.

(J) Kaplan-Meier survival curves for mice bearing GSCs (GSC387 and GSC3565) transduced with either sgCONT or one of two sgRNAs targeting ITGAV (sgCONT, n = 5; ITGAV sgRNA, n = 6). ****p < 0.0001 by log rank analysis.

(K) Representative H&E images from (J). Boxes show magnified sections. Scale bars, 50 μm.

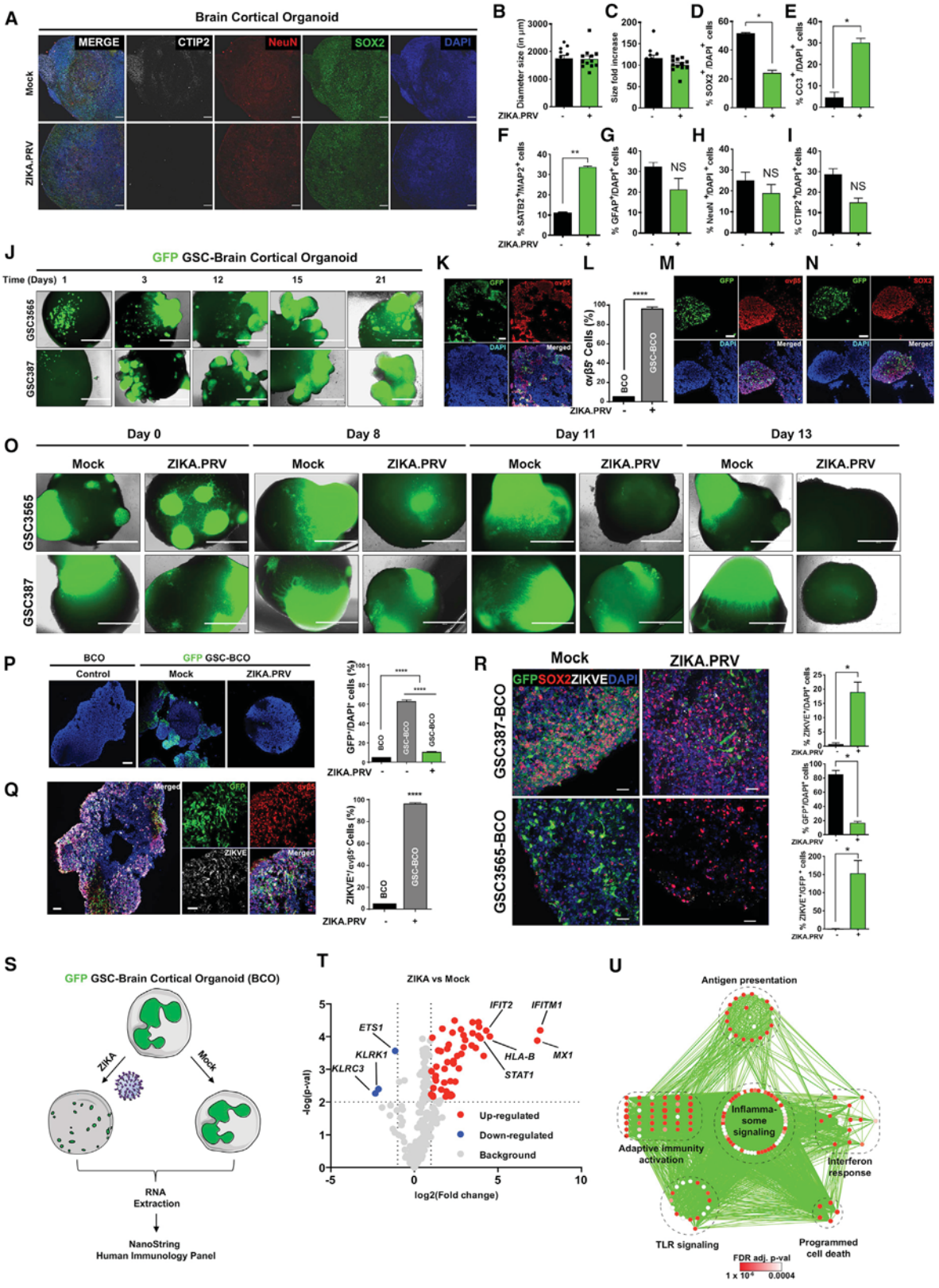


(legend on next page)

complex involved in viral internalization. $\alpha_v$ integrins are a particularly attractive set of targets for several reasons. These integrins are often expressed at low levels in normal tissues, with induction upon stress environments found in tumors (Desgrosellier and Cheresh, 2010). Further, integrins can be modulated with acceptable toxicity through neutralizing antibodies or small molecules. More than two decades ago, these integrins were linked to adenovirus infection (Wickham et al., 1993). More recently, selected integrins have been associated with viral infection of other viruses in the flavivirus family, albeit with differential results based on assay (Schmidt et al., 2013; Fan et al., 2017). $\alpha_v$ integrins have been linked to cancer stem cells; integrin $\alpha_v\beta_3$ is expressed in epithelial cancer stem cells, where it serves as a driver of tumor initiation and drug resistance (Seguin et al., 2014, 2017). In GBM, $\alpha_v\beta_3$ expression inhibits senescence (Poirot et al., 2015) and facilitates glucose uptake by promoting upregulation of the high-affinity glucose transporter Glut3 (Cosset et al., 2017). ZIKV infection was not inhibited by shRNAs or sgRNAs against ITGB3 or LM609, a highly selective antibody antagonist of $\alpha_v\beta_3$. Instead, our results suggest that a specific integrin heterodimer, $\alpha_v\beta_5$, closely related to $\alpha_v\beta_3$, is required for optimal ZIKV infection in GSCs. Although $\alpha_v$ integrin also is expressed by NPCs, expression of the $\beta_5$ integrin subunit is more selective to GBM, both stem-like and differentiated tumor cells. Therefore, GSCs display preferential sensitivity to ZIKV based on one integrin that is linked to a stem-like state and its partner, which is linked to a neoplastic state.

Our studies suggest an additional molecular mechanism mediating the effects of ZIKV against GSCs: downregulation of the antiviral immune response by SOX2, a core regulator of GSCs. These results stand in contrast to high expression levels of several ISGs in embryonic stem cells and more restricted ISG expression in neural stem cells, which have high levels of SOX2 expression (Wu et al., 2018). The divergent results between GSCs and normal stem cells suggest that SOX2 transcriptional control of ISGs is likely defined by other levels of control, including co-binding of other transcription factors and differential chromatin states. Comparison of the chromatin landscapes of GSCs and NPCs revealed that GSCs have greater activation of chromatin across the genome, which can alter transcriptional regulation (Mack et al., 2019). To further consider the role of immune responses in GSCs upon ZIKV infection, we interrogated transcriptional regulation of immunological modulators of GSCs grown in organoids with normal brains, which demonstrated upregulation of genes in the inflammasome, adaptive immune responses, TLR signaling, and IFN responses. Although SOX2 does not solely determine GSC response to ZIKV, GSCs appear to be less immunogenic than DGCs, offering a potential advantage in sustained tumor growth in the inflammatory environment found in GBMs. This immune phenotype may offer a potential selection factor.

Here we extend the recent description of GBM-BCO systems by another group (Ogawa et al., 2018). We leveraged the system to model the growth patterns of patient-derived models and test the efficacy of antitumor therapies. This system is particularly valuable for measuring the direct therapeutic index of therapies, such as oncolytic viruses, that must provide substantial anti-tumor activity while minimizing toxicity against normal tissues, like

**Figure 6. ZIKV Infection Preferentially Targets GBM in GBM-Brain Cortical Organoid (GSC-BCO) Models and Activates Viral Process and Type I IFN Signaling Pathways**

(A) Representative images of mock- or ZIKV-infected BCOs stained with neuronal markers (CTIP2 and NeuN), a neural progenitor cell marker (SOX2), and DAPI. Scale bars, 100 μm.

(B) Quantification of BCO size p.i. with ZIKV. Significance was assessed by two-tailed Student's t test, and experiments were performed in two batches with 12 organoids per group per batch.

(C) BCO size fold change of ZIKV- and mock-treated groups over a period of 1 month.

(D) Quantification of $SOX2^+$ cells in ZIKV- versus mock-infected groups. *$p < 0.05$ by two-tailed Student's t test.

(E) Quantification of $CC3^+$ cells in ZIKV- versus mock-infected groups. *$p < 0.05$ by two-tailed Student's t test.

(F) Quantification of $SATB2^+$ cells within $MAP2^+$ cells in ZIKV- versus mock-infected groups. **$p < 0.01$ by two-tailed Student's t test.

(G) Quantification of $GFAP^+$ cells in ZIKV- versus mock-infected groups. N.S., not significant by two-tailed Student's t test.

(H) Quantification of $NeuN^+$ cells in ZIKV- versus mock-infected groups. N.S., not significant by two-tailed Student's t test.

(I) Quantification of $CTIP2^+$ cells in ZIKV- versus mock-infected groups. N.S., not significant by two-tailed Student's t test.

(J) Bright-field images of engraftment of two patient-derived GSCs (387 and 3565) transduced with GFP into human BCOs over a time course. Scale bars, 1 mm.

(K) Engrafted GSCs ($GFP^+$) with normal BCO immunostained for integrin $\alpha_v\beta_5$ (red), GFP (green), and DAPI (blue). Scale bars, 200 μm.

(L) Quantification of integrin $\alpha_v\beta_5^+$ cells in normal BCOs or GSC-BCOs. Values represent mean ± SEM. n = 6. ****$p < 0.0001$ by two-tailed Student's t test.

(M) Representative images of GFP-labeled GSC-BCOs immunostained for integrin $\alpha_v\beta_5$ (red), GFP (green), and DAPI (blue). Scale bars, 100 μm.

(N) Representative images of GFP-labeled GSC-BCOs immunostained for SOX2 (red), GFP (green), and DAPI (blue). Scale bars, 100 μm.

(O) Images of GFP-labeled GSC-GFP BCOs 13 days p.i. with ZIKV. Scale bars, 1 mm.

(P) Representative images of residual GSCs (green) and DAPI staining (blue) of GFP-labeled GSC-GFP BCOs cultured under mock conditions or with ZIKV for 2–4 weeks. Scale bars, 200 μm. The percentage of $GFP^+$ cells among $DAPI^+$ cells was quantified. Values represent mean ± SEM. n = 6. ****$p < 0.0001$ by two-way ANOVA.

(Q) Representative immunostaining for integrin $\alpha_v\beta_5$ (red), GFP (green), ZIKV-E (white), and DAPI (blue) of GFP-labeled GSC-GFP BCOs mock- or ZIKV-infected for 2–4 weeks. Scale bars, 200 μm (left) and 100 μm (center). The percentage of $ZIKV\text{-}E^+$ cells among integrin $\alpha_v\beta_5$ cells was quantified. Values represent mean ± SEM. n = 6. ****$p < 0.0001$ by two-tailed Student's t test.

(R) Representative images of 387 and 3565 GSC-BCOs with or without ZIKV, respectively, stained with SOX2, ZIKV-E, and DAPI. GFP shows the presence of GSCs (scale bars, 50 μm). $ZIKV\text{-}E^+$, $GFP^+$, and $ZIKV\text{-}E^+$ cells among $GFP^+$ cells were quantified by counting (two GSCs cell lines, two repeats, n = 12 organoids/group); *$p < 0.05$ by two-tailed Student's t test.

(S) Schematic of the experiment design.

(T) Volcano plot showing differences between GSC-BCO ZIKV versus GSC-BCO mock. 113 genes were differentially expressed (greater than 1.5-fold) between these two groups (*$p < 0.05$).

(U) Network analysis of genes differentially expressed upon ZIKV infection, represented as a bubble plot.

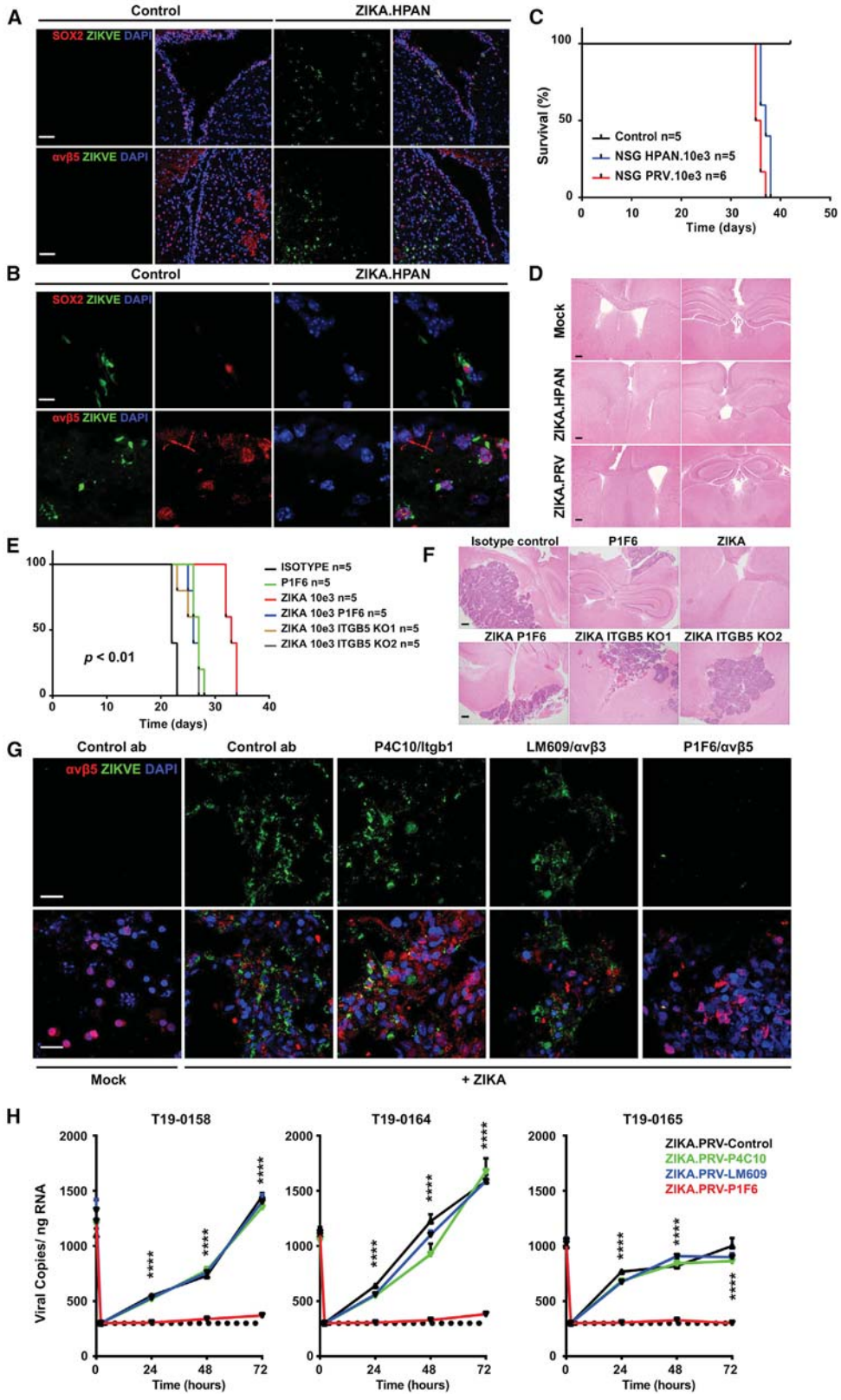


*(legend on next page)*

the brain. Because some viral infections display strong species specificity, the use of human GBMs in organoids of normal human brain may empower greater relevance of selective tumor targeting in preclinical studies. Further, we employed genetic and pharmacologic targeting strategies that can be leveraged to dissect the determinants of tumor response to oncolytic viral therapies.

Although direct application of wild-type ZIKV as an oncolytic virus in GBM would likely be challenging, we and others have already reported that genetically attenuating modifications to ZIKV strains may offer reduced toxicity against normal tissues (Zhu et al., 2017; Chen et al., 2018b). Identification of SOX2-associated downregulation of the innate antiviral immune response that distinguishes normal and neoplastic stem cells and of integrin $\alpha_v\beta_5$ as an important molecular feature mediating infection may prioritize selection of genetically modified ZIKV for use in patients to augment efficacy against the most resistant and aggressive GBMs cells while minimizing virus-induced disease.

## STAR★METHODS

Detailed methods are provided in the online version of this paper and include the following:

- KEY RESOURCES TABLE
- LEAD CONTACT AND MATERIALS AVAILABILITY
- EXPERIMENTAL MODEL AND SUBJECT DETAILS
  - Ethical Compliance Statement
  - Culture of GSCs, DGCs, and nonmalignant brain cultures
  - Proliferation and neurosphere formation assay
  - Brightfield images
  - Immunohistochemistry, immunofluorescence, and microscopy
  - EdU labeling and imaging
  - ZIKV preparation
  - ZIKV titration
  - *In vitro* viral infection
  - Zika viral RNA quantification
  - Binding and internalization assay
  - Lentiviral shRNA transfection
  - Quantitative PCR
  - NanoString nCounter Gene Expression
  - Rosalind NanoString analysis methods
  - Western blotting
  - *In silico* analysis
  - ChIP-Seq and ChIP-PCR
  - Flow cytometry
  - Apoptosis assays
  - CRISPR-Cas9 gRNA and cloning
  - ZIKV *in vivo* inoculation experiments
  - Histology
  - TUNEL staining
  - Human induced pluripotent stem cells (iPSCs), NPCs and BCO generation
  - Generation of GFP-BCOs
  - GSC-brain cortical organoid formation
  - GSC organoid formation
  - GBM organoid and BCOs *in vitro* ZIKV infection
  - Anti-integrin $\alpha_v\beta_5$ antibody treatment of GBM organoids
  - Image analysis
  - Statistical analysis
- DATA AND CODE AVAILABILITY

## SUPPLEMENTAL INFORMATION

Supplemental Information can be found online at https://doi.org/10.1016/j.stem.2019.11.016.

## ACKNOWLEDGMENTS

We thank Drs. Peter Yingxiao Wang and Hsin-Hung Lin (UC, San Diego) for the PGK-EGFP lentiviral vector and Dr. Elsa Molina (UC, San Diego Stem Cell Genomics Core) for technical assistance with experiments using the NanoString nCounter Sprint. We also acknowledge access and use of the UCSD Screening Core to perform part of the experiments presented in this manuscript. This work was made possible in part by CIRM Major Facilities grant FA1-00607 (to the Sanford Consortium for Regenerative Medicine). P.M. has an International Rett Syndrome Foundation (IRSF) mentored training fellowship. A.R.M. is supported by the California Institute for Regenerative Medicine (DISC2-09649). These studies were supported by the NIH through CA217065 (to R.C.G.); CA217066 (to B.C.P.); CA203101 (to L.J.Y.K.); CA159859 and CA199376 (to S.S.); NS097649-01 and CA240953-01 (to C.C.C.); NS096368 (to R.J.W.-R.); R01DK103901 and R01AA027065 (to H.H.); MH107367 and N5105969 (to A.R.M.); CA045726 and CA050286 (to D.A.C.); and CA197718, CA154130, CA169117, CA171652, NS087913, and NS089272 (to J.N.R.).

## AUTHOR CONTRIBUTIONS

Z.Z., P.M., J.L.S.-N., D.A.C., A.R.M., and J.N.R. designed the experiments, analyzed the data, and wrote the manuscript with contributions from all authors. Z.Z., P.M., J.A.B., S.T.S., R.C.G., X.W., H.I.W., S.B., A.E.C., Q.W.,

**Figure 7. Integrin $\alpha_v\beta_5$ Mediates *In Vivo* ZIKV Targeting of GSCs in Mouse Models and in Human GBM**

(A) Immunostaining of the subventricular zone (SVZ) of mice 72 h following ZIKV infection ZIKV-E (green), SOX2 (red, top panels), and integrin $\alpha_v\beta_5$ (red, bottom panels). Scale bars, 50 μm.

(B) Higher magnification of images from (A), demonstrating ZIKV infection of SOX2$^+$ (top panels) and integrin $\alpha_v\beta_5{}^+$ cells. Scale bars, 10 μm.

(C) Survival of ZIKV-infected NSG mice from (A) was plotted by the Kaplan-Meier method.

(D) ZIKV-infected brains from the mice in (A) were collected upon death, and histology was assessed by H&E staining. Scale bars, 20 μm.

(E) Survival of NSG mice following implantation of GSCs treated with isotype control, P1F6 antibody, ZIKV, combined P1F6 and ZIKV, combined CRISPR knockout (KO) of integrin $\beta_5$ (sgRNA1 sgRNA2) with ZIKV inoculation, analyzed by log rank test; $p < 0.01$.

(F) H&E staining of tumor-bearing brains from (E). Scale bars, 50 μm.

(G) Intraoperative brain slices from GBM patients were pre-incubated with an IgG control antibody or an integrin-blocking antibody under mock conditions or upon ZIKV infection (10e3 FFU). Slices then underwent immunofluorescence staining for ZIKV-E (green), integrin $\alpha_v\beta_5$ (red), and DAPI (blue). Scale bars, 10 μm.

(H) Intraoperative brain slices from GBM patients were pre-incubated with an IgG control antibody or an integrin-blocking antibody under mock conditions or upon ZIKV infection. Slices then underwent a viral RNA copy assay by qRT-PCR. Experiments were performed in two biological replicates with three technical repeats. Values represent mean ± SEM. ****$p < 0.0001$ by one-way ANOVA.

B.C.P., L.J.Y.K., Z.L., J.F., R.Z., A.W.W., and R.D. performed the experiments. S.T.S., R.C.G., B.C.P., and L.J.Y.K. performed database analyses. S.S., S.D., C.C.C., R.J.W.-R., F.H.G., J.D.S.-N., M.S.D., and H.H. provided scientific input and helped edit the manuscript. A.G., S.M.W., S.C.M., P.D.N., C.A.T., L.O.P., R.J.W.-R., and J.L.S.-N. provided key reagents.

## DECLARATION OF INTERESTS

A.R.M. is a co-founder and has equity interest in TISMOO, a company dedicated to genetic analysis focusing on therapeutic applications customized for autism spectrum disorder and other neurological disorder origin genetics. The terms of this arrangement have been reviewed and approved by the University of California, San Diego in accordance with its conflict of interest policies. D.A.C. is the co-founder of TargeGen. D.A.C. is a founder of a new company, AlphaBeta Therapeutics, that is developing an antibody to integrin alphaVbeta3, involved in cancer treatment; however, this company is not yet funded. M.S.D. is a consultant for Inbios and Atreca and on the Scientific Advisory Board of Moderna.

Received: July 27, 2018
Revised: July 10, 2019
Accepted: November 22, 2019
Published: January 16, 2020

## REFERENCES

Allen, C., Opyrchal, M., Aderca, I., Schroeder, M.A., Sarkaria, J.N., Domingo, E., Federspiel, M.J., and Galanis, E. (2013). Oncolytic measles virus strains have significant antitumor activity against glioma stem cells. Gene Ther. *20*, 444–449.

Bach, P., Abel, T., Hoffmann, C., Gal, Z., Braun, G., Voelker, I., Ball, C.R., Johnston, I.C., Lauer, U.M., Herold-Mende, C., et al. (2013). Specific elimination of CD133+ tumor cells with targeted oncolytic measles virus. Cancer Res. *73*, 865–874.

Bao, S., Wu, Q., McLendon, R.E., Hao, Y., Shi, Q., Hjelmeland, A.B., Dewhirst, M.W., Bigner, D.D., and Rich, J.N. (2006a). Glioma stem cells promote radioresistance by preferential activation of the DNA damage response. Nature *444*, 756–760.

Bao, S., Wu, Q., Sathornsumetee, S., Hao, Y., Li, Z., Hjelmeland, A.B., Shi, Q., McLendon, R.E., Bigner, D.D., and Rich, J.N. (2006b). Stem cell-like glioma cells promote tumor angiogenesis through vascular endothelial growth factor. Cancer Res. *66*, 7843–7848.

Boonnak, K., Slike, B.M., Burgess, T.H., Mason, R.M., Wu, S.J., Sun, P., Porter, K., Rudiman, I.F., Yuwono, D., Puthavathana, P., and Marovich, M.A. (2008). Role of dendritic cells in antibody-dependent enhancement of dengue virus infection. J. Virol. *82*, 3939–3951.

Bowman, R.L., Wang, Q., Carro, A., Verhaak, R.G., and Squatrito, M. (2017). GlioVis data portal for visualization and analysis of brain tumor expression datasets. Neuro Oncol. *19*, 139–141.

Brinton, M.A. (2013). Replication cycle and molecular biology of the West Nile virus. Viruses *6*, 13–53.

Buetow, M.P., Buetow, P.C., and Smirniotopoulos, J.G. (1991). Typical, atypical, and misleading features in meningioma. Radiographics *11*, 1087–1106.

Chailangkarn, T., Trujillo, C.A., Freitas, B.C., Hrvoj-Mihic, B., Herai, R.H., Yu, D.X., Brown, T.T., Marchetto, M.C., Bardy, C., McHenry, L., et al. (2016). A human neurodevelopmental model for Williams syndrome. Nature *536*, 338–343.

Chen, J., Yang, Y.F., Yang, Y., Zou, P., Chen, J., He, Y., Shui, S.L., Cui, Y.R., Bai, R., Liang, Y.J., et al. (2018a). AXL promotes Zika virus infection in astrocytes by antagonizing type I interferon signalling. Nat. Microbiol. *3*, 302–309.

Chen, Q., Wu, J., Ye, Q., Ma, F., Zhu, Q., Wu, Y., Shan, C., Xie, X., Li, D., Zhan, X., et al. (2018b). Treatment of Human Glioblastoma with a Live Attenuated Zika Virus Vaccine Candidate. MBio *9*, e01683–e18.

Chu, J.J.H., and Ng, M.L. (2004). Interaction of West Nile virus with alpha v beta 3 integrin mediates virus entry into cells. J. Biol. Chem. *279*, 54533–54541.

Cosset, É., Ilmjärv, S., Dutoit, V., Elliott, K., von Schalscha, T., Camargo, M.F., Reiss, A., Moroishi, T., Seguin, L., Gomez, G., et al. (2017). Glut3 Addiction Is a Druggable Vulnerability for a Molecularly Defined Subpopulation of Glioblastoma. Cancer Cell *32*, 856–868.e5.

Darmanis, S., Sloan, S.A., Croote, D., Mignardi, M., Chernikova, S., Samghababi, P., Zhang, Y., Neff, N., Kowarsky, M., Caneda, C., et al. (2017). Single-Cell RNA-Seq Analysis of Infiltrating Neoplastic Cells at the Migrating Front of Human Glioblastoma. Cell Reports *21*, 1399–1410.

Desgrosellier, J.S., and Cheresh, D.A. (2010). Integrins in cancer: biological implications and therapeutic opportunities. Nat. Rev. Cancer *10*, 9–22.

Donato, M., Xu, Z., Tomoiaga, A., Granneman, J.G., Mackenzie, R.G., Bao, R., Than, N.G., Westfall, P.H., Romero, R., and Draghici, S. (2013). Analysis and correction of crosstalk effects in pathway analysis. Genome Res. *23*, 1885–1893.

Draghici, S., Khatri, P., Tarca, A.L., Amin, K., Done, A., Voichita, C., Georgescu, C., and Romero, R. (2007). A systems biology approach for pathway level analysis. Genome Res. *17*, 1537–1745.

Drost, J., and Clevers, H. (2018). Organoids in cancer research. Nat. Rev. Cancer *18*, 407–418.

Fabregat, A., Jupe, S., Matthews, L., Sidiropoulos, K., Gillespie, M., Garapati, P., Haw, R., Jassal, B., Korninger, F., May, B., et al. (2018). The Reactome Pathway Knowledgebase. Nucleic Acids Res. *46*, D649–D655.

Fan, W., Qian, P., Wang, D., Zhi, X., Wei, Y., Chen, H., and Li, X. (2017). Integrin αvβ3 promotes infection by Japanese encephalitis virus. Res. Vet. Sci. *111*, 67–74.

Foo, S.S., Chen, W., Chan, Y., Bowman, J.W., Chang, L.C., Choi, Y., Yoo, J.S., Ge, J., Cheng, G., Bonnin, A., et al. (2017). Asian Zika virus strains target $CD14^{+}$ blood monocytes and induce M2-skewed immunosuppression during pregnancy. Nat. Microbiol. *2*, 1558–1570.

Foreman, P.M., Friedman, G.K., Cassady, K.A., and Markert, J.M. (2017). Oncolytic Virotherapy for the Treatment of Malignant Glioma. Neurotherapeutics *14*, 333–344.

Gangemi, R.M.R., Griffero, F., Marubbi, D., Perera, M., Capra, M.C., Malatesta, P., Ravetti, G.L., Zona, G.L., Daga, A., and Corte, G. (2009). SOX2 Silencing in Glioblastoma Tumor-Initiating Cells Causes Stop of Proliferation and Loss of Tumorigenicity. Stem Cells *27*, 40–48.

Garcez, P.P., Loiola, E.C., Madeiro da Costa, R., Higa, L.M., Trindade, P., Delvecchio, R., Nascimento, J.M., Brindeiro, R., Tanuri, A., and Rehen, S.K. (2016). Zika virus impairs growth in human neurospheres and brain organoids. Science *352*, 816–818.

Geer, L.Y., Marchler-Bauer, A., Geer, R.C., Han, L., He, J., He, S., Liu, C., Shi, W., and Bryant, S.H. (2010). The NCBI BioSystems database. Nucleic Acids Res. *38*, D492–D496.

Heinz, S., Benner, C., Spann, N., Bertolino, E., Lin, Y.C., Laslo, P., Cheng, J.X., Murre, C., Singh, H., and Glass, C.K. (2010). Simple combinations of lineage-determining transcription factors prime cis-regulatory elements required for macrophage and B cell identities. Mol. Cell *38*, 576–589.

Heymann, D.L., Hodgson, A., Sall, A.A., Freedman, D.O., Staples, J.E., Althabe, F., Baruah, K., Mahmud, G., Kandun, N., Vasconcelos, P.F., et al. (2016). Zika virus and microcephaly: why is this situation a PHEIC? Lancet *387*, 719–721.

Hu, Y., and Smyth, G.K. (2009). ELDA: Extreme limiting dilution analysis for comparing depleted and enriched populations in stem cell and other assays. J. Immunol. Methods. *347*, 70–78.

Hubert, C.G., Rivera, M., Spangler, L.C., Wu, Q., Mack, S.C., Prager, B.C., Couce, M., McLendon, R.E., Sloan, A.E., and Rich, J.N. (2016). A three-dimensional organoid culture system derived from human glioblastomas recapitulates the hypoxic gradients and cancer stem cell heterogeneity of tumors found in vivo. Cancer Res. *76*, 2465–2477.

Ianevski, A., He, l., Aittokallio, T., and Tang, J. (2017). SynergyFinder: a web application for analyzing drug combination dose–response matrix data. Bioinformatics *33*, 2413–2415.

Josupeit, R., Bender, S., Kern, S., Leuchs, B., Hielscher, T., Herold-Mende, C., Schlehofer, J.R., Dinsart, C., Witt, O., Rommelaere, J., and Lacroix, J. (2016).

Pediatric and Adult High-Grade Glioma Stem Cell Culture Models Are Permissive to Lytic Infection with Parvovirus H-1. Viruses *8*, E138.

Kaid, C., Goulart, E., Caires-Júnior, L.C., Araujo, B.H.S., Soares-Schanoski, A., Bueno, H.M.S., Telles-Silva, K.A., Astray, R.M., Assoni, A.F., Júnior, A.F.R., et al. (2018). Zika virus selectively kills aggressive human embryonal CNS tumor cells in vitro and in vivo. Cancer Res. *78*, 3363–3374.

Kanehisa, M., Furumichi, M., Tanabe, M., Sato, Y., and Morishima, K. (2017). KEGG: new perspectives on genomes, pathways, diseases and drugs. Nucleic Acids Res. *45*, D353–D361.

Kanehisa, M., Sato, Y., Furumichi, M., Morishima, K., and Tanabe, M. (2019). New approach for understanding genome variations in KEGG. Nucleic Acids Res. *47*, D590–D595.

Lathia, J.D., Gallagher, J., Heddleston, J.M., Wang, J., Eyler, C.E., Macswords, J., Wu, Q., Vasanji, A., McLendon, R.E., Hjelmeland, A.B., and Rich, J.N. (2010). Integrin alpha 6 regulates glioblastoma stem cells. Cell Stem Cell *6*, 421–432.

Lazear, H.M., Govero, J., Smith, A.M., Platt, D.J., Fernandez, E., Miner, J.J., and Diamond, M.S. (2016). A Mouse Model of Zika Virus Pathogenesis. Cell Host Microbe *19*, 720–730.

Li, C., Xu, D., Ye, Q., Hong, S., Jiang, Y., Liu, X., Zhang, N., Shi, L., Qin, C.F., and Xu, Z. (2016). Zika Virus Disrupts Neural Progenitor Development and Leads to Microcephaly in Mice. Cell Stem Cell *19*, 120–126.

Liberzon, A., Subramanian, A., Pinchback, R., Thorvaldsdóttir, H., Tamayo, P., and Mesirov, J.P. (2011). Molecular signatures database (MSigDB) 3.0. Bioinformatics *27*, 1739–1740.

Liu, F., Hon, G.C., Villa, G.R., Turner, K.M., Ikegami, S., Yang, H., Ye, Z., Li, B., Kuan, S., Lee, A.Y., et al. (2015). EGFR Mutation Promotes Glioblastoma through Epigenome and Transcription Factor Network Remodeling. Mol. Cell. *60*, 307–318.

Love, M.I., Huber, W., and Anders, S. (2014). Moderated estimation of fold change and dispersion for RNA-seq data with DESeq2. Genome Biology *15*, 550.

Mack, S.C., Pajtler, K.W., Chavez, L., Okonechnikov, K., Bertrand, K.C., Wang, X., Erkek, S., Federation, A., Song, A., Lee, C., et al. (2018). Therapeutic targeting of ependymoma as informed by oncogenic enhancer profiling. Nature *553*, 101–105.

Mack, S.C., Singh, I., Wang, X., Hirsch, R., Wu, Q., Villagomez, R., Bernatchez, J.A., Zhu, Z., Gimple, R.C., Kim, L.J.Y., et al. (2019). Chromatin landscapes reveal developmentally encoded transcriptional states that define human glioblastoma. J. Exp. Med. *216*, 1071–1090.

Marchetto, M.C.N., Carromeu, C., Acab, A., Yu, D., Yeo, G.W., Mu, Y., Chen, G., Gage, F.H., and Muotri, A.R. (2010). A model for neural development and treatment of Rett syndrome using human induced pluripotent stem cells. Cell *143*, 527–539.

Medigeshi, G.R., Hirsch, A.J., Streblow, D.N., Nikolich-Zugich, J., and Nelson, J.A. (2008). West Nile Virus Entry Requires Cholesterol-Rich Membrane Microdomains and Is Independent of alphavbeta3 Integrin. J. Virol. *82*, 5212–5219.

Meertens, L., Labeau, A., Dejarnac, O., Cipriani, S., Sinigaglia, L., Bonnet-Madin, L., Le Charpentier, T., Hafirassou, M.L., Zamborlini, A., Cao-Lormeau, V.M., et al. (2017). Axl Mediates ZIKA Virus Entry in Human Glial Cells and Modulates Innate Immune Responses. Cell Rep. *18*, 324–333.

Merico, D., Isserlin, R., Stueker, O., Emili, A., and Bader, G.D. (2010). Enrichment Map: A Network-Based Method for Gene-Set Enrichment Visualization and Interpretation. PLoS ONE *5*, e13984.

Mesci, P., Macia, A., LaRock, C.N., Tejwani, L., Fernandes, I.R., Suarez, N.A., de A Zanotto, P.M., Beltrão-Braga, P.C.B., Nizet, V., and Muotri, A.R. (2018). Modeling neuro-immune interactions during Zika virus infection. Hum. Mol. Genet. *27*, 41–52.

Michlmayr, D., Andrade, P., Gonzalez, K., Balmaseda, A., and Harris, E. (2017). $CD14^{+}CD16^{+}$ monocytes are the main target of Zika virus infection in peripheral blood mononuclear cells in a paediatric study in Nicaragua. Nat. Microbiol. *2*, 1462–1470.

Miner, J.J., Cao, B., Govero, J., Smith, A.M., Fernandez, E., Cabrera, O.H., Garber, C., Noll, M., Klein, R.S., Noguchi, K.K., et al. (2016). Zika Virus Infection during Pregnancy in Mice Causes Placental Damage and Fetal Demise. Cell *165*, 1081–1091.

Mitchell, A.L., Attwood, T.K., Babbitt, P.C., Blum, M., Bork, P., Bridge, A., Brown, S.D., Chang, H.Y., El-Gebali, S., Fraser, M.I., et al. (2019). InterPro in 2019: improving coverage, classification and access to protein sequence annotations. Nucleic Acids Res. *47*, D351–D360.

Milde, T., Kleber, S., Korshunov, A., Witt, H., Hielscher, T., Koch, P., Kopp, H.G., Jugold, M., Deubzer, H.E., Oehme, I., et al. (2011). A novel human high-risk ependymoma stem cell model reveals the differentiation-inducing potential of the histone deacetylase inhibitor Vorinostat. Acta Neuropathol. *122*, 637–650.

Mootha, V.K., Lindgren, C.M., Eriksson, K.F., Subramanian, A., Sihag, S., Lehar, J., Puigserver, P., Carlsson, E., Ridderstråle, M., Laurila, E., et al. (2003). PGC-1$\alpha$-responsive genes involved in oxidative phosphorylation are coordinately downregulated in human diabetes. Nat. Genet. *34*, 267–273.

Nowakowski, T.J., Pollen, A.A., Di Lullo, E., Sandoval-Espinosa, C., Bershteyn, M., and Kriegstein, A.R. (2016). Expression Analysis Highlights AXL as a Candidate Zika Virus Entry Receptor in Neural Stem Cells. Cell Stem Cell *18*, 591–596.

Ogawa, J., Pao, G.M., Shokhirev, M.N., and Verma, I.M. (2018). Glioblastoma Model Using Human Cerebral Organoids. Cell Rep. *23*, 1220–1229.

Oh, Y., Zhang, F., Wang, Y., Lee, E.M., Choi, I.Y., Lim, H., Mirakhori, F., Li, R., Huang, L., Xu, T., et al. (2017). Zika virus directly infects peripheral neurons and induces cell death. Nat. Neurosci. *20*, 1209–1212.

Oliveira Melo, A.S., Malinger, G., Ximenes, R., Szejnfeld, P.O., Alves Sampaio, S., and Bispo de Filippis, A.M. (2016). Zika virus intrauterine infection causes fetal brain abnormality and microcephaly: tip of the iceberg? Ultrasound Obstet. Gynecol. *47*, 6–7.

Paşca, A.M., Sloan, S.A., Clarke, L.E., Tian, Y., Makinson, C.D., Huber, N., Kim, C.H., Park, J.Y., O'Rourke, N.A., Nguyen, K.D., et al. (2015). Functional cortical neurons and astrocytes from human pluripotent stem cells in 3D culture. Nat. Methods *12*, 671–678.

Petersen, E., Wilson, M.E., Touch, S., McCloskey, B., Mwaba, P., Bates, M., Dar, O., Mattes, F., Kidd, M., Ippolito, G., et al. (2016). Rapid Spread of Zika Virus in The Americas–Implications for Public Health Preparedness for Mass Gatherings at the 2016 Brazil Olympic Games. Int. J. Infect. Dis. *44*, 11–15.

Poirot, L., Philip, B., Schiffer-Mannioui, C., Le Clerre, D., Chion-Sotinel, I., Derniame, S., Potrel, P., Bas, C., Lemaire, L., Galetto, R., et al. (2015). Multiplex Genome-Edited T-cell Manufacturing Platform for "Off-the-Shelf" Adoptive T-cell Immunotherapies. Cancer Res. *75*, 3853–3864.

Pollen, A.A., Nowakowski, T.J., Chen, J., Retallack, H., Sandoval-Espinosa, C., Nicholas, C.R., Shuga, J., Liu, S.J., Oldham, M.C., Diaz, A., et al. (2015). Molecular Identity of Human Outer Radial Glia during Cortical Development. Cell *163*, 55–67.

Qian, X., Nguyen, H.N., Song, M.M., Hadiono, C., Ogden, S.C., Hammack, C., Yao, B., Hamersky, G.R., Jacob, F., Zhong, C., et al. (2016). Brain-Region-Specific Organoids Using Mini-bioreactors for Modeling ZIKV Exposure. Cell *165*, 1238–1254.

Quinlan, A.R., and Hall, I.M. (2010). BEDTools: a flexible suite of utilities for comparing genomic features. Bioinformatics *26*, 841–842.

Ramírez, F., Ryan, D.P., Grüning, B.A., Bhardwaj, V., Kilpert, F., Richter, A.S., Heyne, S., Dundar, F., and Manke, T. (2016). deepTools2: a next generation web server for deep-sequencing data analysis. Nucleic Acids Res. *44*, W160–W165.

Reich, M., Liefeld, T., Gould, J., Lerner, J., Tamayo, P., and Mesirov, J.P. (2006). GenePattern 2.0. Nat. Genet. *38*, 500–501.

Retallack, H., Di Lullo, E., Arias, C., Knopp, K.A., Laurie, M.T., Sandoval-Espinosa, C., Mancia Leon, W.R., Krencik, R., Ullian, E.M., Spatazza, J., et al. (2016). Zika virus cell tropism in the developing human brain and inhibition by azithromycin. Proc. Natl. Acad. Sci. USA. *113*, 14408–14413.

Ritchie, M.E., Phipson, B., Wu, D., Hu, Y., Law, C.W., Shi, W., and Smyth, G.K. (2015). limma powers differential expression analyses for RNA-sequencing and microarray studies. Nucleic Acids Res. *43*, e47.

Robinson, J.T., Thorvaldsdóttir, H., Winckler, W., Guttman, M., Lander, E.S., Getz, G., and Mesirov, J.P. (2011). Integrative genomics viewer. Nat. Biotechnol. *29*, 24–26.

Russell, S.J., Peng, K.W., and Bell, J.C. (2012). Oncolytic virotherapy. Nat. Biotechnol. *30*, 658–670.

Sarkar, A., and Hochedlinger, K. (2013). The sox family of transcription factors: versatile regulators of stem and progenitor cell fate. Cell Stem Cell *12*, 15–30.

Schafer, S.T., Paquola, A.C.M., Stern, S., Gosselin, D., Ku, M., Pena, M., Kuret, T.J.M., Liyanage, M., Mansour, A.A., Jaeger, B.N., Marchetto, M.C., Glass, C.K., Mertens, J., and Gage, F.H. (2019). Pathological priming causes developmental gene network heterochronicity in autistic subject-derived neurons. Nat. Neurosci. *22*, 243–255.

Schindelin, J., Arganda-Carreras, I., Frise, E., Kaynig, V., Longair, M., Pietzsch, T., Preibisch, S., Rueden, C., Saalfeld, S., Schmid, B., et al. (2012). Fiji: an open-source platform for biological-image analysis. Nat. Methods *9*, 676–682.

Schmidt, K., Keller, M., Bader, B.L., Korytář, T., Finke, S., Ziegler, U., and Groschup, M.H. (2013). Integrins modulate the infection efficiency of West Nile virus into cells. J. Gen. Virol. *94*, 1723–1733.

Schuler-Faccini, L., Ribeiro, E.M., Feitosa, I.M., Horovitz, D.D., Cavalcanti, D.P., Pessoa, A., Doriqui, M.J., Neri, J.I., Neto, J.M., Wanderley, H.Y., et al.; Brazilian Medical Genetics Society–Zika Embryopathy Task Force (2016). Possible Association Between Zika Virus Infection and Microcephaly - Brazil, 2015. MMWR Morb. Mortal. Wkly. Rep. *65*, 59–62.

Seguin, L., Kato, S., Franovic, A., Camargo, M.F., Lesperance, J., Elliott, K.C., Yebra, M., Mielgo, A., Lowy, A.M., Husain, H., et al. (2014). An integrin $\beta_3$-KRAS-RalB complex drives tumour stemness and resistance to EGFR inhibition. Nat. Cell Biol. *16*, 457–468.

Seguin, L., Camargo, M.F., Wettersten, H.I., Kato, S., Desgrosellier, J.S., von Schalscha, T., Elliott, K.C., Cosset, E., Lesperance, J., Weis, S.M., and Cheresh, D.A. (2017). Galectin-3, a Druggable Vulnerability for KRAS-Addicted Cancers. Cancer Discov. *7*, 1464–1479.

Shannon, P., Markiel, A., Ozier, O., Baliga, N.S., Wang, J.T., Ramage, D., Amin, N., Schwikowski, B., and Ideker, T. (2003). Cytoscape: a software environment for integrated models of biomolecular interaction networks. Genome Res. *13*, 2498–2504.

Singh, S.K., Clarke, I.D., Terasaki, M., Bonn, V.E., Hawkins, C., Squire, J., and Dirks, P.B. (2003). Identification of a cancer stem cell in human brain tumors. Cancer Res. *63*, 5821–5828.

Slenter, D.N., Kutmon, M., Hanspers, K., Riutta, A., Windsor, J., Nunes, N., Mélius, J., Cirillo, E., Coort, S.L., Digles, D., et al. (2018). WikiPathways: a multifaceted pathway database bridging metabolomics to other omics research. Nucleic Acids Res. *46*, D661–D667.

Soneson, C., Love, M.I., and Robinson, M.D. (2016). Differential analyses for RNA-seq: transcript-level estimates improve gene-level inferences. F1000Res *4*, 1521.

Souza, B.S.F., Sampaio, G.L., Pereira, C.S., Campos, G.S., Sardi, S.I., Freitas, L.A., Figueira, C.P., Paredes, B.D., Nonaka, C.K., Azevedo, C.M., et al. (2016). Zika virus infection induces mitosis abnormalities and apoptotic cell death of human neural progenitor cells. Sci. Rep. *6*, 39775.

Stupp, R., Mason, W.P., van den Bent, M.J., Weller, M., Fisher, B., Taphoorn, M.J., Belanger, K., Brandes, A.A., Marosi, C., Bogdahn, U., et al. (2005). Radiotherapy plus Concomitant and Adjuvant Temozolomide for Glioblastoma. N. Engl. J. Med. *352*, 987–996.

Subramanian, A., Tamayo, P., Mootha, V.K., Mukherjee, S., Ebert, B.L., Gillette, M.A., Paulovich, A., Pomeroy, S.L., Golub, T.R., Lander, E.S., and Mesirov, J.P. (2005). Gene set enrichment analysis: A knowledge-based approach for interpreting genome-wide expression profiles. Proc. Natl. Acad. Sci. USA. *102*, 15545–15550.

Suvà, M.L., Rheinbay, E., Gillespie, S.M., Patel, A.P., Wakimoto, H., Rabkin, S.D., Riggi, N., Chi, A.S., Cahill, D.P., Nahed, B.V., et al. (2014). Reconstructing and reprogramming the tumor-propagating potential of glioblastoma stem-like cells. Cell *157*, 580–594.

Tang, H., Hammack, C., Ogden, S.C., Wen, Z., Qian, X., Li, Y., Yao, B., Shin, J., Zhang, F., Lee, E.M., et al. (2016). Zika Virus Infects Human Cortical Neural Progenitors and Attenuates Their Growth. Cell Stem Cell *18*, 587–590.

Tang, Z., Li, C., Kang, B., Gao, G., Li, C., and Zhang, Z. (2017). GEPIA: a web server for cancer and normal gene expression profiling and interactive analyses. Nucleic Acids Res. *45*, W98–W102.

Thomas, C.A., Tejwani, L., Trujillo, C.A., Negraes, P.D., Herai, R.H., Mesci, P., Macia, A., Crow, Y.J., and Muotri, A.R. (2017). ). Modeling of TREX1-Dependent Autoimmune Disease using Human Stem Cells Highlights L1 Accumulation as a Source of Neuroinflammation. Cell Stem Cell *21*, 319–331.e8.

Thorvaldsdottir, H., Robinson, J.T., and Mesirov, J.P. (2013). Integrative Genomics Viewer (IGV): high-performance genomic data visualization and exploration. Brief. Bioinform. *14*, 178–192.

Trujillo, C.A., Gao, R., Negraes, P.D., Gu, J., Buchanan, J., Preissl, S., Wang, A., Wu, W., Haddad, G.G., Chaim, I.A., et al. (2019). Complex Oscillatory Waves Emerging from Cortical Organoids Model Early Human Brain Network Development. Cell Stem Cell *25*, 558–569.e7.

Wakimoto, H., Kesari, S., Farrell, C.J., Curry, W.T., Jr., Zaupa, C., Aghi, M., Kuroda, T., Stemmer-Rachamimov, A., Shah, K., Liu, T.C., et al. (2009). Human glioblastoma-derived cancer stem cells: establishment of invasive glioma models and treatment with oncolytic herpes simplex virus vectors. Cancer Res. *69*, 3472–3481.

Wang, X., Huang, Z., Wu, Q., Prager, B.C., Mack, S.C., Yang, K., Kim, L.J.Y., Gimple, R.C., Shi, Y., Lai, S., et al. (2017a). MYC-regulated mevalonate metabolism maintains brain tumor–initiating cells. Cancer Res. *77*, 4947–4960.

Wang, X., Yang, K., Xie, Q., Wu, Q., Mack, S.C., Shi, Y., Kim, L.J.Y., Prager, B.C., Flavahan, W.A., Liu, X., et al. (2017b). Purine synthesis promotes maintenance of brain tumor initiating cells in glioma. Nat. Neurosci. *20*, 661–673.

Wang, X., Prager, B.C., Wu, Q., Kim, L.J.Y., Gimple, R.C., Shi, Y., Yang, K., Morton, A.R., Zhou, W., Zhu, Z., et al. (2018). Reciprocal Signaling between Glioblastoma Stem Cells and Differentiated Tumor Cells Promotes Malignant Progression. Cell Stem Cell *22*, 514–528.e5.

Wells, M.F., Salick, M.R., Wiskow, O., Ho, D.J., Worringer, K.A., Ihry, R.J., Kommineni, S., Bilican, B., Klim, J.R., Hill, E.J., et al. (2016). Genetic Ablation of AXL Does Not Protect Human Neural Progenitor Cells and Cerebral Organoids from Zika Virus Infection. Cell Stem Cell *19*, 703–708.

Wickham, T.J., Mathias, P., Cheresh, D.A., and Nemerow, G.R. (1993). Integrins $\alpha$ v $\beta$ 3 and $\alpha$ v $\beta$ 5 promote adenovirus internalization but not virus attachment. Cell *73*, 309–319.

Wu, A., Wei, J., Kong, L.Y., Wang, Y., Priebe, W., Qiao, W., Sawaya, R., and Heimberger, A.B. (2010). Glioma cancer stem cells induce immunosuppressive macrophages/microglia. Neuro-oncol. *12*, 1113–1125.

Wu, X., Dao Thi, V.L., Huang, Y., Billerbeck, E., Saha, D., Hoffmann, H.H., Wang, Y., Silva, L.A.V., Sarbanes, S., Sun, T., et al. (2018). Intrinsic Immunity Shapes Viral Resistance of Stem Cells. Cell *172*, 423–438.e25.

Zemp, F.J., Lun, X., McKenzie, B.A., Zhou, H., Maxwell, L., Sun, B., Kelly, J.J., Stechishin, O., Luchman, A., Weiss, S., et al. (2013). Treating brain tumor-initiating cells using a combination of myxoma virus and rapamycin. Neuro. Oncol. *15*, 904–920.

Zhou, J., Li, C., Sachs, N., Chiu, M.C., Wong, B.H., Chu, H., Poon, V.K., Wang, D., Zhao, X., Wen, L., et al. (2018). Differentiated human airway organoids to assess infectivity of emerging influenza virus. Proc. Natl. Acad. Sci. USA. *115*, 6822–6827.

Zhu, Z., Gorman, M.J., McKenzie, L.D., Chai, J.N., Hubert, C.G., Prager, B.C., Fernandez, E., Richner, J.M., Zhang, R., Shan, C., et al. (2017). Zika virus has oncolytic activity against glioblastoma stem cells. J. Exp. Med. *214*, 2843–2857.

## STAR★METHODS

### KEY RESOURCES TABLE

| REAGENT or RESOURCE | SOURCE | IDENTIFIER |
|---|---|---|
| Antibodies | | |
| Rabbit polyclonal antibody to SOX2 | Abcam | Cat# ab97959; RRID:AB_2341193 |
| Mouse monoclonal antibody to ZIKVE | EMD Millipore | Cat# MAB10216; RRID:AB_827205 |
| Rabbit Cleaved Caspase3 antibody | Cell signaling | Cat# 9664; RRID:AB_2070042 |
| Rabbit polyclonal antibody to AXL | Abcam | Cat# ab32828; RRID:AB_725598 |
| Rabbit polyclonal antibody to GFAP (Poly284000) | Biolegend | Cat# 840001; RRID:AB_2565444 |
| Mouse monoclonal antibody to beta-actin | Sigma-Aldrich | Cat# A5316; RRID:AB_476743 |
| Rabbit monoclonal antibody to $\alpha_v\beta_5$ | Absolute Antibody | Cat# Ab00888 |
| Mouse monoclonal antibody to TUBB3 | Thermofisher | Cat# MA1-118; RRID:AB_2536829 |
| PE Mouse IgG1, κ Isotype Ctrl (FC) Control Antibody [Clone: MOPC-21] | Biolegend | Cat# 400113; RRID:AB_326435 |
| Alexa Fluor 488 conjugated anti-mouse | Thermofisher | Cat# A-11001; RRID:AB_2534069 |
| Alexa Fluor 594 conjugated anti–rabbit | Thermofisher | Cat# A-11012; RRID:AB_2534079 |
| Alexa Fluor 594 conjugated anti–rat | Thermofisher | Cat# A-11007; RRID:AB_10561522 |
| Alexa Fluor 647 conjugated anti–goat | Thermofisher | Cat# A-21447; RRID:AB_2535864 |
| Anti-rabbit IgG, HRP-linked Secondary Antibody | Cell Signaling | Cat# 7074; RRID:AB_2099233 |
| Anti-mouse IgG, HRP-linked Secondary Antibody | Cell Signaling | Cat# 7076; RRID:AB_330924 |
| donkey anti-goat IgG-HRP-lined Secondary Antibody | Santa Cruz Biotechnology | Cat# sc-2020; RRID:AB_631728 |
| Donkey anti-Rabbit IgG (H+L) Highly Cross-Adsorbed Secondary Antibody, Alexa Fluor 488 | Life Technologies | Cat# A-21206; RRID:AB_2535792 |
| Normal Goat IgG antibody (negative control for ChIP-PCR) | R & D Systems | Cat# AB-108-C; RRID:AB_354267 |
| Rabbit monoclonal (14C10) antibody to GAPDH | Cell Signaling | Cat# 2118; RRID:AB_561053 |
| Rabbit polyclonal antibody to CTIP2 | US Biological | Cat# B0807-13E2; RRID:AB_2064140 |
| Mouse monoclonal antibody to NeuN | PhosphoSolutions | Cat# 538-FOX3; RRID:AB_2560943 |
| Rat monoclonal antibody to ITGA6 | Thermofisher | Cat# 17-0495-82; RRID:AB_2016694 |
| Chicken polyclonal antibody to MAP2 | Abcam | Cat# ab5392; RRID:AB_2138153 |
| Rabbit monoclonal antibody to SATB2 | RevMAb Biosciences | Cat# 31-1251-00; RRID:AB_2783604 |
| LM609 antibody | EMD Millipore | Cat# MAB1976; RRID:AB_2296419 |
| P1F6 antibody | EMD Millipore | Cat# MAB1961Z; RRID:AB_94466 |
| Bacterial and Virus Strains | | |
| One Shot™ Stbl3™ Chemically Competent E. coli | Thermofisher | Cat# C737303 |
| ZIKA.HPAN | BEI Resources | NR-50210 |
| ZIKA.PRV | BEI Resources | NR-50240 |
| Chemicals, Peptides, and Recombinant Proteins | | |
| Neurobasal-A Medium | Life Technologies | Cat# A2477501 |
| GlutaMAX Supplement | Life Technologies | Cat# 35050061 |
| MEM nonessential amino acids | Thermofisher | Cat# 11140-050 |
| Sodium Pyruvate | Life Technologies | Cat# 11360070 |
| N2 NeuroPlex | Gemini Bio-Products | Cat# 400163 |
| Gem21 NeuroPlex | Gemini Bio-Products | Cat# 400160 |
| B27-supplement w/o Vitamin A | Life Technologies | Cat# 12587010 |
| Recombinant Human EGF Protein | R&D Systems | Cat# 236-EG-01M |
| Recombinant Human FGF basic, 145 aa (TC Grade) Protein | R&D Systems | Cat# 4114-TC-01M |
| Recombinant Human BDNF | Peprotech | Cat# 450-02 |

(*Continued on next page*)

*Continued*

| REAGENT or RESOURCE | SOURCE | IDENTIFIER |
|---|---|---|
| Recombinant Human GDNF | Peprotech | Cat# 450-10 |
| Recombinant Human NT-3 | Peprotech | Cat# 450-03 |
| L-Ascorbic acid | Sigma-Aldrich | Cat# A4403 |
| N6,20-O-Dibutyryladenosine 30,50-cyclic monophosphate sodium salt | Sigma-Aldrich | Cat# D0627 |
| Stemolecule SB431542 | StemGent | Cat# 04-0010-10 |
| Dorsomorphin | R&D Systems | Cat# 3093 |
| ROCK inhibitor (Ri) Y-27632 dihydrochloride | Tocris | Cat# 125410 |
| StemPro Accutase Cell Dissociation Reagent | Thermofisher | Cat# A1110501 |
| Penicillin-Streptomycin (10,000 U/mL) | Thermofisher | Cat# 15140122 |
| TrypLE™ Express Enzyme (1X), no phenol red | Thermofisher | Cat# 12604021 |
| Fetal Bovine Serum, qualified, US origin | Thermofisher | Cat# 26140079 |
| NuPage 4%–12% Bis-Tris gels | Invitrogen | NP0321BOX |
| PVDF membranes | EMD Millipore | Cat# ISEQ00010 |
| Matrigel hESC-Qualified Matrix | Corning | Cat# 354277 |
| LipoD293™ In Vitro DNA Transfection Reagent | SignaGen Laboratories | Cat# SL100668 |
| JetPrime transfection reagent | Polyplus | Cat# 89129-926 |
| qScript cDNA synthesis kit | Quanta | Cat# 101414-106 |
| EndoFree Plasmid mini kit | Omega | Cat# D6948 |
| Click-iT EdU imaging Kit with Alexa 594 | Molecular probes | Cat# C10086 |
| TUNEL Assay Kit - HRP-DAB | Abcam | Cat# ab206386 |
| PowerUp™ SYBR™ Green Master Mix | Thermofisher | Cat# A25742 |
| Radiant™ Green Hi-ROX qPCR Kit, 5000 x 20μl Reactions,50 x 1mL | Alkali scientific inc | Cat# QS2050 |
| Qiagen RNeasy Mini Plus kit | Qiagen | Cat# 74134 |
| QIAamp Viral RNA Mini Kit | Qiagen | Cat# 52904 |
| Cell Titer-Glo™ Cell Viability Reagent | Promega | Cat# G7570 |
| Dead Cell Apoptosis Kit with Annexin V Alexa Fluor™ 488 | Thermofisher | Cat# V13241 |
| High Capacity cDNA Reverse Transcription Kit | Life Technologies | Cat# 4368814 |
| Lenti-X Concentrator | Clontech (Takara Bio USA) | Cat# 631232 |
| Pronase | Roche Applied Science | Cat# 10165921001 |
| Bradford assay | Bio-Rad Laboratories | Cat# 5000006 |
| Mission Lentiviral Packaging Mix | Sigma-Aldrich | Cat# SHP001 |
| Quick-RNA MiniPrep Plus kit | Zymo Research | Cat# R1055 |
| TRIzol reagent | Sigma-Aldrich | Cat# T9424 |
| TaqMan® Universal Master Mix II, no UNG | Thermofisher | Cat# 4440043 |
| Critical Commercial Assays | | |
| VECTASHIELD with DAPI | Vector Laboratories | Cat# H-1200; RRID:AB_2336790 |
| Experimental Models: Cell Lines | | |
| 293FT Cell Line | Thermofisher | Cat# R70007 |
| ENSA (ENS-tem-A) | EMD Millipore | Cat# SCC003, RRID:CVCL_GS51 |
| NSC11 | Alstem | Mack et al., 2019 |
| NM53 | Cleveland Clinic | N/A |
| NM55 | Cleveland Clinic | N/A |
| NM177 | Cleveland Clinic | N/A |
| NPC C4-7 | Gage lab, Salk | Schafer et al., 2019 |
| hNP1 (STEMEZ hNP1) | Neuromics | Cat# HN60001 |
| H1 ESC | RCB | Cat# RCB1778, RRID:CVCL_N541 |

(*Continued on next page*)

*Continued*

| REAGENT or RESOURCE | SOURCE | IDENTIFIER |
|---|---|---|
| NPC194 | Cleveland clinic | Mack et al., 2019 |
| EP1 | DKFZ | Milde et al., 2011 |
| fh NPC | Clontech Stem Cell Line Kits | Y40050 |
| WT83 iPS and NPC | Muotri Lab, UCSD | N/A |
| WT126 iPS and NPC | Muotri Lab, UCSD | RRID:CVCL_HA44 |
| DAOY | ATCC | Cat# HTB-186, RRID:CVCL_1167 |
| D283 | ATCC | Cat# HTB-185, RRID:CVCL_1155 |
| HDMB03 | DSMZ | Cat# ACC-740, RRID:CVCL_S506 |
| D341 | ATCC | Cat# HTB-187, RRID:CVCL_0018 |
| HNA/Human Astrocyte kit | Thermofisher | Cat# N7805200 |
| Experimental Models: Organisms/Strains | | |
| NSG (NOD.Cg-*Prkdc*$^{scid}$*Il2rg*$^{tm1Wjl}$/SzJl) | The Jackson Laboratory | JAX: 005557 |
| Recombinant DNA | | |
| pCMV-dR8.2 dvpr | Addgene | Plasmid# 8455, RRID:Addgene_8455 |
| pCI-VSVG | Addgene | Plasmid# 1733, RRID:Addgene_1733 |
| LentiCRISPR v2 | Addgene | Plasmid# 52961, RRID:Addgene_52961 |
| SOX2 shRNA: shSOX52 | Sigma-Aldrich | TRCN0000355694 |
| SOX2 shRNA: shSOX53 | Sigma-Aldrich | TRCN0000355638 |
| Non-targeting Control shRNA: shCONT | Sigma-Aldrich | pLKO.1 Non-targeting Vector (SHC002) |
| psPAX2 | Addgene | Plasmid# 12260, RRID:Addgene_12260 |
| pMD2.G | Addgene | Plasmid# 12259, RRID:Addgene_12259 |
| pSIN-hPGK-EGFP-WPRE | Peter Wang's lab, UCSD | N/A |
| Software and Algorithms | | |
| GlioVis | Bowman et al., 2017 | http://gliovis.bioinfo.cnio.es |
| DeepTools (v2.4.1) | Ramírez et al., 2016 | http://deeptools.readthedocs.io/en/latest/index.html |
| Extreme limiting-dilution analysis | Hu and Smyth, 2009 | http://bioinf.wehi.edu.au/software/elda/ |
| Trim Galore v0.4.3 | | https://www.bioinformatics.babraham.ac.uk/projects/trim_galore |
| FASTQC | | https://www.bioinformatics.babraham.ac.uk/projects/fastqc/ |
| Gene Set Enrichment Analyses | Mootha et al., 2003; Subramanian et al., 2005 | http://software.broadinstitute.org/gsea/index.jsp |
| Synthego ICE Analysis | | https://ice.synthego.com/#/ |
| Gene Expression Profiling Interactive Analyses (GEPIA) | Tang et al., 2017 | http://gepia.cancer-pku.cn/about.html |
| Synergy Finder | Ianevski et al., 2017 | N/A |
| HOMER | Heinz et al., 2010 | http://homer.ucsd.edu/homer/ |
| DESeq2 | Love et al., 2014 | https://bioconductor.org/packages/release/bioc/html/DESeq2.html |
| BedTools | Quinlan and Hall, 2010 | http://bedtools.readthedocs.io/en/latest/ |
| Cytoscape | Shannon et al., 2003 | http://www.cytoscape.org/ |
| TXImport | Soneson et al., 2016 | https://bioconductor.org/packages/release/bioc/html/tximport.html |
| GraphPad Prism | Commercially available | https://www.graphpad.com/scientific-software/prism/ |
| Adobe Illustrator | Commercially available | https://www.adobe.com/ |
| R Programming Language | | https://www.r-project.org/ |
| R Studio | Commercially available | https://www.rstudio.com/ |
| Microsoft Office | Commercially available | https://www.office.com/ |

(*Continued on next page*)

*Continued*

| REAGENT or RESOURCE | SOURCE | IDENTIFIER |
|---|---|---|
| IGV (Integrative Genomics Viewer) | Robinson et al., 2011; Thorvaldsdottir et al., 2013 | https://software.broadinstitute.org/software/igv/ |
| Image Lab | Commercially available | http://www.bio-rad.com/en-us/product/image-lab-software?ID=KRE6P5E8Z |
| Gene Pattern | Reich et al., 2006 | https://software.broadinstitute.org/cancer/software/genepattern/ |
| ImageJ / FIJI | Schindelin et al., 2012 | https://fiji.sc/ |
| Other | | |
| BD LSR Fortessa Flow Cytometer | Beckman | N/A |
| ZEISS 580 Confocal Microscope | ZEISS | N/A |
| Zeiss Apotome microscope | ZEISS | N/A |
| NanoString nCounter system | NanoString | N/A |
| Applied Biosystems 7500HT cycler | Applied Biosystems | N/A |
| nSolver software | NanoString | N/A |
| CFX96 Touch Detection System | Bio-Rad | N/A |
| Glioblastoma Stem Cell and Differentiated Glioblastoma Cell H3K27ac ChIP-seq and RNA-seq data | Suvà et al., 2014 | GEO: GSE54792 |
| Glioblastoma Tissue H3K27ac ChIP-seq data | Liu et al., 2015 | GEO: GSE72468 |
| Glioblastoma Tissue H3K27ac ChIP-seq data | Wang et al., 2017b | GEO: GSE101148 |
| Glioblastoma single-cell RNA-seq data | Darmanis et al., 2017 | GEO: GSE84465 |
| Normal Brain single-cell RNA-seq data | Pollen et al., 2015 | Supplemental Data |
| Normal Brain Tissue H3K27ac ChIP-seq Data | Encode Project | https://www.encodeproject.org/files/ENCFF398LQI/@@download/ENCFF398LQI.bam |
| Normal Brain Tissue H3K27ac ChIP-seq Data | Encode Project | https://www.encodeproject.org/files/ENCFF317ZJQ/@@download/ENCFF317ZJQ.bam |
| Normal Brain Tissue H3K27ac ChIP-seq Data | Encode Project | https://www.encodeproject.org/files/ENCFF883QEJ/@@download/ENCFF883QEJ.bam |
| Normal Brain Tissue H3K27ac ChIP-seq Data | Encode Project | https://www.encodeproject.org/files/ENCFF858WMB/@@download/ENCFF858WMB.bam |
| Normal Brain Tissue H3K27ac ChIP-seq Data | Encode Project | https://www.encodeproject.org/files/ENCFF465XYF/@@download/ENCFF465XYF.bam |
| Normal Brain Tissue H3K27ac ChIP-seq Data | Encode Project | https://www.encodeproject.org/files/ENCFF042WIR/@@download/ENCFF042WIR.bam |
| Normal Brain Tissue H3K27ac ChIP-seq Data | Encode Project | https://www.encodeproject.org/files/ENCFF854IBQ/@@download/ENCFF854IBQ.bam |
| Normal Brain Tissue H3K27ac ChIP-seq Data | Encode Project | https://www.encodeproject.org/files/ENCFF258IAC/@@download/ENCFF258IAC.bam |
| Normal Brain Tissue H3K27ac ChIP-seq Data | Encode Project | https://www.encodeproject.org/files/ENCFF021NCO/@@download/ENCFF021NCO.bam |
| Normal Brain Tissue H3K27ac ChIP-seq Data | Encode Project | https://www.encodeproject.org/files/ENCFF866QWG/@@download/ENCFF866QWG.bam |
| Normal Brain Tissue H3K27ac ChIP-seq Data | Encode Project | https://www.encodeproject.org/files/ENCFF284YVJ/@@download/ENCFF284YVJ.bam |
| Normal Brain Tissue H3K27ac ChIP-seq Data | Encode Project | https://www.encodeproject.org/files/ENCFF300PEE/@@download/ENCFF300PEE.bam |
| Normal Brain Tissue H3K27ac ChIP-seq Data | Encode Project | https://www.encodeproject.org/files/ENCFF240QQV/@@download/ENCFF240QQV.bam |
| Normal Brain Tissue H3K27ac ChIP-seq Data | Encode Project | https://www.encodeproject.org/files/ENCFF592XMP/@@download/ENCFF592XMP.bam |
| Normal Brain Tissue H3K27ac ChIP-seq Data | Encode Project | https://www.encodeproject.org/files/ENCFF519BFV/@@download/ENCFF519BFV.bam |
| GlioVis | Bowman et al., 2017 | http://gliovis.bioinfo.cnio.es |

## LEAD CONTACT AND MATERIALS AVAILABILITY

All data will be provided to reviewers and/or editors upon request. There are no restrictions on data availability. Further information and requests should be addressed to and will be fulfilled by the Lead Contact, Jeremy Rich (drjeremyrich@gmail.com).

## EXPERIMENTAL MODEL AND SUBJECT DETAILS

### Ethical Compliance Statement

For intracranial tumor models, NSG (NOD.Cg-*Prkdc*$^{scid}$*Il2rg*$^{tm1Wjl}$/SzJl, #005557, Jackson Laboratory, Bar Harbor, ME) mice were used under the University of California, San Diego Institutional Animal Care and Use Committee (IACUC) approved protocol. All experiments conformed to the ethical and humane standards for animal treatment as defined by our protocol. Animals were monitored daily and were humanely sacrificed upon the appearance of any neurological signs.

### Culture of GSCs, DGCs, and nonmalignant brain cultures

Glioblastoma tissues were obtained from excess surgical materials from patients at the Cleveland Clinic after neuropathology review with appropriate consent, in accordance with an IRB-approved protocol. To prevent culture-induced drift, patient-derived xenografts were generated and maintained as a recurrent source of tumor cells for study (Wang et al., 2017a). To prevent culture-induced drift in GBM models, patient-derived subcutaneous xenografts were generated in NOD.Cg-*Prkdc*$^{scid}$*Il2rg*$^{tm1Wjl}$/SzJl mice (#005557, Jackson Laboratory) and maintained as a recurrent source of tumor cells for study. Upon xenograft removal, a papain dissociation system (Worthington Biochemical) was used to dissociate tumors according to the manufacturer's instructions. Cells were then cultured in Neurobasal complete media (Neurobasal medium; Life Technologies) supplemented with 1 × B27 without vitamin A (Thermofisher), 2 mM l-glutamine (Thermofisher), 1 mM sodium pyruvate (Thermofisher), 20 ng/ml basic fibroblast growth factor (bFGF), and 20 ng/ml epidermal growth factor (EGF; R&D Systems). The GSCs phenotype was validated by OLIG2 and SOX2 expression, functional assays of self-renewal (serial neurosphere passage), and tumor propagation using *in vivo* limiting dilution. All cells were incubated at 37°C in humidified incubators supplemented with 5% $CO_2$ and tested to ensure that they were negative for mycoplasma. See also Table S1 for GSCs lines.

### Proliferation and neurosphere formation assay

Cell viability was measured using CellTiter-Glo (Promega) according to the manufacturer's instructions. All data were normalized to day 0, prior to infection with ZIKV, and expressed as a relative cell number. Neurosphere formation was measured as previously described (Wang et al., 2017b, 2018). Briefly, decreasing numbers of cells per well (50, 20, 10, 5, and 1) were plated into 96-well plates. Seven days after plating, the presence and number of neurospheres in each well were recorded. Extreme limiting dilution (ELDA) analysis was performed using software available at http://bioinf.wehi.edu.au/software/elda (Wang et al., 2017a, 2018).

### Brightfield images

GFP-GSC, GSCs and BCOs images were acquired on an EVOS cell imaging microscope (Thermofisher). Images were acquired using an ImageXpress Micro automated microscope (Molecular Devices) and exported using MetaXpress 5.3 (Molecular Devices).

### Immunohistochemistry, immunofluorescence, and microscopy

Ten μm-thick cryosections were air-dried and fixed in 3.7% paraformaldehyde (PFA) for 15 minutes before being washed twice with PBS. Tissues were permeabilized by incubating the slides with 1% Triton X-100 in PBS for 15 minutes at room temperature. After blocking for 1 hour at room temperature in a blocking buffer containing 0.25% Triton X-100, 2.5% BSA in 1 × PBS, slides were incubated overnight in a humidified chamber at 4°C with primary antibodies for ZIKV (Millipore; AB10216; working dilution 1:1,000), SOX2 (Millipore; AB5603; stock: 1 mg/ml; working dilution 1:400), GFAP (Invitrogen, PA5-18598; working dilution 1:1,000), AXL (Abcam; AB32828; stock: 1 mg/ ml; working dilution 1:200), TUBB3 (Thermofisher; MA1-118; working dilution 1:500) and MAP2 (Abcam; ab5392, working dilution 1:2000). After 1xPBS washes, slides were incubated with Alexa Fluor 488–, 594–, or 647–conjugated anti–mouse, anti–rat, anti-goat, or anti–rabbit secondary antibodies (Thermofisher, working dilution 1:1000). Slides were subsequently washed and mounted using VECTASHIELD with DAPI (Vector Laboratories). For immunocytochemistry stainings, $10^5$ cells were seeded into a 12-well chamber slide (Thermofisher) and cultured overnight. Slides were then processed as described previously for tissue staining. 10 ×, 20 ×, and 40 × images were collected at room temperature on Zeiss Apotome microscope. The cells were identified based on DAPI. Image analysis was performed by thresholding for positive staining and normalizing to total tissue area using ImageJ and Zen (Zeiss) software. Quantification was performed in a blinded manner to eliminate bias.

### EdU labeling and imaging

The EdU labeling was performed according to the manufacturer's instructions (Thermofisher). Briefly, cells were plated on coverslips and allowed to recover overnight. A final concentration of 10 μM EdU was added (Click-iT EdU imaging Kit, molecular probes). The cells were then incubated for 1 hour at 37°C. After incubation, the media was removed and 0.5 mL of 3.7% paraformaldehyde was

added in PBS to each well containing the coverslips. The cells were then incubated for 15 minutes at room temperature. The paraformaldehyde was removed, and the cells were washed twice with 1 mL of 3% BSA in PBS. The wash solution was then removed and 1 mL of 0.5% Triton® X-100 in PBS (permeabilization buffer) was added to each well, then incubated at room temperature for 20 minutes. The permeabilization buffer was then removed, the cells were washed twice with 1 mL of 3% BSA in PBS. Finally, 0.5 mL of Click-iT® reaction cocktail was added to each well containing a coverslip. The plate was briefly rocked to ensure that the reaction cocktail was distributed evenly over the coverslip for 30 minutes at room temperature, protected from light. After 30 minutes, the reaction cocktail was removed, cells were washed once with 1 mL of 3% BSA in PBS before proceeding to DNA staining (DAPI, Vector Laboratories H-1200) and imaging (Zeiss Apotome).

### ZIKV preparation

ZIKV human isolates H/PAN/2016/BEI-259634 and PRVABC59 (BEI Resources, NR-50210 and NR-50240) from Panama and Puerto Rico, respectively, were acquired from the ATCC and distributed by BEI. Viruses were amplified in Vero cells, totaling 2-3 serial passages of the original viral stock. Infected cell supernatants were concentrated through a 30% sucrose cushion, and re-suspended in neural maintenance medium base (50% DMEM/F12 Glutamax, 50% Neurobasal medium, 1x N2 Supplement, 1x B27 Supplement all from Life Technologies) supplemented with 1% DMSO and 5% FBS and stored at −80°C. Viral stock titers were determined by plaque assay on Vero cells and were greater or equal to $2 \times 10^8$ plaque forming units/ml. Mock media was prepared by concentrating uninfected Vero cell supernatant as above.

### ZIKV titration

Viral titers (plaque forming units (FFU)/mL) were calculated by plaque-forming assays on Vero cells. Vero cells were seeded at a density of $7.5 \times 10^4$ cells per well in standard 24-well plates and incubated at 5% $CO_2$, 37°C for 48 hours before infection. Serial dilutions of supernatants were collected from ZIKV-infected NPCs and GSCs after infection with ZIKV at MOI of 0.1 FFU/cell, and then added to Vero cells for 1 hour. Cells were covered with an agarose overlay and further incubated for 72 hours. 3.7% paraformaldehyde was added on top of overlays for 24 hours to fix monolayers, overlays were removed, and cell monolayers were stained with crystal violet to visualize plaques.

### *In vitro* viral infection

GSCs were plated at 5,000 cells/well in 96-well tissue culture plates and allowed to attach overnight. For viral infection and growth inhibition assays, ZIKA.HPAN and ZIKA.PRV at a range of MOI 0.1, 1, and 5 FFU/cell.

### Zika viral RNA quantification

Quantitative real-time PCR (qRT-PCR) was performed using primers, probes, RNA standards, and conditions described previously (Boonnak et al., 2008). Briefly, Viral RNA was extracted from cell culture using the QIAamp Viral RNA Mini Kit (QIAGEN, Valencia, CA). ZIKV RNAs were detected using TaqMan® Universal Master Mix II, no UNG (Thermofisher). The samples were carried out in 20 μL reactions and the run method was as follows: 10 minutes at 95°C, 42 cycles of 15 s at 95°C followed by 1 minute at 58°C. The sensitivity of the ZIKV real-time assays was evaluated by titration of serial dilution of virus with a previously known titer. GraphPad Prism was used as fitting software. See also Table S2 for the ZIKV primers.

### Binding and internalization assay

To measure ZIKV cell surface binding/adsorption, the GSCs and hNPCs incubated with indicated integrin receptor neutralizing antibodies at 50 μg/ml for 1 hour at 4°C, were exposed to ZIKV at a MOI of 5 FFU/cell, along with serum-only and media-only controls for 1 hour at 4°C. Cells were washed three times at 4°C with 10 mL PBS containing 10% BSA. The number of viruses that bound to the cells was determined by qRT-PCR. To measure ZIKV immune complex internalization, cells were exposed to ZIKV at MOI of 5 FFU/cell. The cells were washed three times with 10 mL PBS and resuspended with PBS containing 10% BSA. The cells were treated with 5 mg/ml of Pronase (Roche Applied Science, Indianapolis, IN) to remove excess virus on the cell surface. The number of internalized viruses was determined by qRT-PCR (Boonnak et al., 2008).

### Lentiviral shRNA transfection

shRNA sequences were selected from the Mission 2.0 library (Sigma-Aldrich). Plasmids were transformed and amplified in Dh5α competent *E. coli* and purified using EndoFree Plasmid mini kit (Omega, #D6948). For lentivirus preparation, 293T cells were seeded in 6-well plates and transfected with shRNA against SOX2, AXL vectors and Mission Lentiviral Packaging Mix (Sigma-Aldrich, #SHP001) using JetPrime transfection reagent (Polyplus, #89129-926). After 24 hours, growth media was changed to Neurobasal media and after 48 hours, supernatants were collected and GSCs were infected. After 48 hours of infection, GSCs were trypsinized and reseeded on a 96-well plate for subsequent ZIKV infection. In parallel, total RNA was extracted using Quick-RNA MiniPrep Plus kit (Zymo Research, #R1055). 500 ng of RNA was used to synthesize complementary DNA using qScript cDNA synthesis kit (Quanta, #101414-106). Samples were diluted tenfold and gene expression was analyzed by a CFX96 Touch Detection System (Bio-Rad) using FastStart SYBR Green Master Mix (Roche). See also Table S2 for shRNA sequences and primer pairs.

### Quantitative PCR

Total cellular RNA was isolated using TRIzol reagent (Sigma-Aldrich), followed by RT into cDNA using the qScript cDNA Synthesis kit (Quanta BioSciences). Real-time PCR was performed using an Applied Biosystems 7500HT cycler using Taq-Man Universal PCR Master Mix (Thermofisher Scientific). See also Table S2 for primer pairs sequences.

### NanoString nCounter Gene Expression

Total RNA was extracted from mock or ZIKV-infected GSC-brain cortical organoids using QIAGEN RNeasy Mini Plus kit according to manufacturer's instructions. 50ng of total RNA was then processed with the NanoString nCounter system (NanoString, Seattle, Washington, USA) per vendor instructions with Human Immunology Panel. Data export and normalization were performed using nSolver software (NanoString). Data was further analyzed using Rosalind On Ramp software.

### Rosalind NanoString analysis methods

Data was analyzed by Rosalind (https://rosalind.onramp.bio/), with a HyperScale architecture developed by OnRamp BioInformatics, Inc. (San Diego, CA). Read Distribution percentages, violin plots, identity heatmaps, and sample MDS plots were generated as part of the QC step. The limma R library (Ritchie et al., 2015) was used to calculate fold changes and p values. Clustering of genes for the final heatmap of differentially expressed genes was done using the PAM (Partitioning Around Medoids) method using the fpc R library that takes into consideration of the direction and type of all signals on a pathway, the position, role and type of every gene, etc. Functional enrichment analysis of pathways, gene ontology, domain structure and other ontologies was performed using HOMER (Heinz et al., 2010). Several database sources were referenced for enrichment analysis, including Interpro (Mitchell et al., 2019), NCBI (Geer et al., 2010), KEGG6 (Kanehisa et al., 2017, 2019), MSigDB (Subramanian et al., 2005; Liberzon et al., 2011), REACTOME (Fabregat et al., 2018), WikiPathways (Slenter et al., 2018). Enrichment was calculated relative to a set of background genes relevant for the experiment. Additional gene enrichment is available from the following partner institutions: Advaita (http://advaitabio.com/ipathwayguide/; Draghici et al., 2007; Donato et al., 2013).

### Western blotting

Cells were collected and lysed in RIPA buffer (50 mmol/L Tris-HCl, pH 7.5; 150 mmol/L NaCl; 0.5% NP-40; 50 mmol/L NaF with protease inhibitors) and incubated on ice for 30 minutes. Lysates were centrifuged at 14,000 rpm at 4°C for 10 minutes, and supernatant was collected. Protein concentration was determined using the Bradford assay (Bio-Rad Laboratories). Equal amounts of protein samples were mixed with SDS Laemmli loading buffer, boiled and electrophoresed using NuPAGE Bis-Tris Gels (Life Technologies), and then transferred onto PVDF membranes (Millipore). Blocking was performed for 45 minutes using TBS-T supplemented with 5% nonfat dry milk and blotting performed with primary antibodies at 4°C for 16 hours. Primary antibodies used were SOX2 antibody (R&D, #AF2018), OLIG2 antibody (Millipore, #MABN50), GFAP antibody (BD, #BDB610565), β-Actin antibody (Cell signaling, #4970), Integrin alpha V antibody (Abcam, ab124968), Integrin β5 antibody (R&D, AF3824), Integrin β3 antibody (Sigma-Aldrich, SAB4501586), Integrin alpha 6 antibody (Abcam, ab181551), Cleaved Caspase-3 antibody (Cell signaling, #9664) and GAPDH antibody (Abcam, ab9484).

### *In silico* analysis

mRNA data were obtained from The Cancer Genome Atlas (TCGA) GBM HG-U133A microarray dataset using the GlioVis web portal (Bowman et al., 2017). Expression of each gene was correlated with expression of SOX2. A ''SOX2 positively correlated'' gene set was defined by selecting genes with an $r > 0.4$ and the ''SOX2 negatively correlated'' gene set was defined by selecting genes with an $r < -0.4$. Gene sets were inputted into the Broad Institute online Gene Set Enrichment Analysis (GSEA) Tool (Mootha et al., 2003; Subramanian et al., 2005) (http://software.broadinstitute.org/gsea/index.jsp). The top enrichment pathways were visualized using a bar graph showing the $-\text{Log}_{10}$ of FDR corrected p value for the pathway enrichment. Gene set enrichment bubble plots were generated using the Bader Lab Enrichment Map (Merico et al., 2010) in cytoscape. Bubbles represent single gene sets that are enriched with lines demonstrating overlapping genes between enriched pathways. The borders of the circles represent the FDR corrected p value for each pathway.

### ChIP-Seq and ChIP-PCR

Cells ($5 \times 10^6$) per condition were collected, and 5 mg SOX2 antibody (R&D Systems, #AF2018-SP) or goat-IgG (R&D Systems, #AB-108-C) was used for the immunoprecipitation of the DNA protein immunocomplexes. ChIP was performed using the Millipore Magna ChIP (MAGNA0017) according to the manufacturer's protocol. See also Table S3 for the purified DNA qPCR primer sets.

Three technical replicates were performed with SOX2 ChIP-PCR data presented as fold change relative to the non-specific antibody (goat-IgG). Stem and differentiated glioma cell ChIP-seq data were downloaded from GEO using accession number GSE54047. GBM primary tissue ChIP-seq data was accessed from GSE101148. Normal Brain primary tissue ChIP-seq data was accessed through the publicly available Roadmap Epigenomics (http://www.roadmapepigenomics.org/) and Encode Project web portals (https://www.encodeproject.org/). Data were viewed using IGV (http://software.broadinstitute.org/software/igv/).

### Flow cytometry

Cell pellets were washed with PBS and blocked with 1% BSA in PBS for 30 minutes at room temperature and stained with anti-$\alpha_v\beta_5$ antibody (Millipore, #MAB1961, 5 μg/mL in 1% BSA in PBS) and a fluorescently labeled secondary antibody (Thermofisher, #A21235, 1:1000). After the staining, the cells were incubated with PI (Sigma-Aldrich, #P4864, 1:1000), and flow cytometry was performed on BD LSRFortessa™. The levels of $\alpha_v\beta_5$ integrin were analyzed using the flow cytometry analysis program FlowJo (FlowJo, LLC).

### Apoptosis assays

Apoptosis was assessed using the Dead Cell Apoptosis Kit with Annexin V Alexa Fluor 488 from Thermofisher (#V13241) according to the manufacturer's instructions. Samples were analyzed using flow cytometry on a BD LSR Fortessa Flow Cytometer.

### CRISPR-Cas9 gRNA and cloning

The CRISPR design tool from the Broad Institute (https://portals.broadinstitute.org/gpp/public/analysis-tools/sgrna-design) was used to design the guide RNA (gRNA). Oligonucleotides were purchased from Thermofisher and were annealed and cloned into LentiCRISPR v2 plasmid, which was a gift from F. Zhang (Addgene plasmid 52961). 293FT cells were used to generate lentiviral particles through co-transfection of the packaging vectors pCMV-dR8.2 dvpr and pCI-VSVG using a standard calcium phosphate transfection method in Neurobasal complete media.

For knockout studies, GSC3565 cells were transduced with a CRISPR-Cas9 construct targeting integrins or a non-targeting control and selected for integration of the lentiviral construct by puromycin. Single cells were expanded *in vitro* to obtain clonal populations and knockout was confirmed by immunostaining and western blotting. Two clonal populations per sgRNA were subjected to parallel *in vitro* proliferation assays and *in vivo* survival assays. For *in vitro* studies, cells were plated in 96-well plates on Matrigel as above and maintained in standard serum-free media. For *in vivo* studies, cells were intracranially implanted into age-matched female NSG mice. Between five and six mice where used for each sgRNA construct. All mice were monitored daily until development of neurological signs, at which time they were euthanized, as described previously (Wang et al., 2018). See also Table S4 for the gRNA oligonucleotide sequences.

### ZIKV *in vivo* inoculation experiments

The 4-6 weeks old female NSG mice (NOD.Cg-*Prkdc*$^{scid}$*Il2rg*$^{tm1Wjl}$/SzJl, #005557) were purchased from Jackson Laboratory. All animal experiments were approved by the Animal Experiment Committee of Laboratory Animal Center (Washington University, IACUC-20170066). For the ZIKV transformed NPCs *in vivo* study, NSG mice were inoculated intracranially with $10^3$ FFU of ZIKA.HPAN or PRV at subventricular zone (SVZ). PBS injection was used as a control. For the tumor implantation survival study, groups of NSG mice were inoculated intracranially with $10^4$ GSC3565. For P1F6 treatment, GSC3565 were incubated with $\alpha_v\beta_5$ antibody at 50 μg/ml for an hour in cold PBS. For ZIKV inoculation, $10^3$ FFU of ZIKA.HPAN or PRV was mixed with GSCs before implantation *in vivo*. PBS injection was used as a control.

### Histology

10 μm-thick sections of paraffin-embedded tissues were analyzed for hematoxylin and eosin (H&E; Thermofisher), Picro-Sirius Red (Sigma-Aldrich), and Masson's Trichrome (Diagnostic Biosystems) according to the manufacturer's instructions. 4 ×, 10 ×, and 20 × images were captured by AT2 Aperio Scan Scope. Image analysis was performed by thresholding for positive staining and normalizing to total tissue area using ImageJ (NIH) and MetaMorph v7.7.0.0 (Molecular Devices) software.

### TUNEL staining

Tissue sections were deparaffinized and permeabilized with proteinase K (25 μg/ml in 100 mM Tris·HCl). An *in situ* apoptotic cell death detection kit (TUNEL Assay Kit - HRP-DAB, Abcam) based on the TUNEL assay was used as per the manufacturer's instructions to detect apoptotic cells. The percentage of apoptotic nuclei per section was calculated by counting the total number of TUNEL-staining nuclei divided by the total number of hematoxylin-positive nuclei in 8–10 randomly selected fields at × 20 magnification.

### Human induced pluripotent stem cells (iPSCs), NPCs and BCO generation

Human iPSCs cell lines obtained from healthy patients were generated as previously described (Marchetto et al., 2010; Chailangkarn et al., 2016), by reprogramming fibroblasts from healthy donors. The iPSC colonies were plated on Matrigel-coated (BD Biosciences) plates and maintained in mTESR media (Stem Cell Technologies). hiPSC-derived NPCs were obtained and maintained as previously described (Marchetto et al., 2010; Chailangkarn et al., 2016). The iPSCs lines maintained in mTESR media were switched to N2 media, DMEM/F12 media supplemented with 1x N2 NeuroPlex Serum-Free Supplement (Gemini) supplemented with the dual SMAD inhibitors 1 μM of dorsomorphin (Tocris) and 10 μM of SB431542 (Stemgent) daily, for 48 hours. After two days, colonies were scraped off and cultured under agitation (95 rpm) as embryoid bodies (EB) for seven days using N2 media with dorsomorphin and SB431542. Media was changed every other day. EBs were then plated on Matrigel-coated dishes and maintained in DMEM/F12 supplemented with 0.5x of N2 supplement, 0.5x Gem21 NeuroPlex Serum-Free Supplement (Gemini), 20 ng/ml basic fibroblast growth factor (bFGF, Life Technologies) and 1% penicillin/streptomycin (P/S). After seven days in culture, rosettes arising from

the plated EBs were manually picked, gently dissociated with StemPro Accutase (Life Technologies) and plated onto poly-L-ornithine/Laminin-coated (Life Technologies) plates. NPCs were maintained in DMEM/F12 with 0.5x N2, 0.5x Gem21, 20 ng/ml bFGF and 1% P/S. The media was changed every other day. NPCs were split as soon as confluent using StemPro Accutase for 5 mininutes at 37°C, centrifuged and replated with NGF with a 1:3 ratio in poly-L-ornithine/Laminin-coated plates.

Human iPSC-derived cortical organoids were obtained as previously described by Paşca et al. (2015) with modifications (Thomas et al., 2017; Trujillo et al., 2019). Briefly, iPSC colonies were gently dissociated using Accutase in PBS (1:1) (Life Technologies). Cells were then transferred to 6-well plates and kept under suspension. For neural induction, media containing DMEM/F12, 15 mM HEPES, 1x Glutamax, 1x N2 NeuroPlex (Gemini), 1x MEM-NEAA, 1 μM dorsomorphin (R&D Systems), 10 μM SB431542 (Stemgent) and 100 U/ml penicillin-streptomycin was used for six days. NPCs proliferation was obtained in the presence of Neurobasal media supplemented with 2x Gem21 NeuroPlex, 1x NEAA, 1x Glutamax, 20 ng/ml bFGF (Life Technologies) for seven days followed by seven additional days with the same media supplemented with 20 ng/ml EGF (PeproTech). Finally, for neuronal maturation, Neurobasal media supplemented 2x Gem21 NeuroPlex, 1x NEAA, 1x Glutamax, 10ng/mL of BDNF, 10ng/mL of GDNF, 10ng/mL of NT-3 (all from PeproTech), 200 μM L-ascorbic acid and 1mM dibutyryl-cAMP (Sigma-Aldrich) was used for seven days. The cells were kept in the same media thereafter in the absence of growth factors for neuronal maturation.

All the cell lines tested negative for mycoplasma contamination. All experiments were approved and performed in accordance with the Institutional Review Boards (IRB) and Embryonic Stem Cell Research Oversight (ESCRO) guidelines and regulations.

### Generation of GFP-BCOs

The PGK-EGFP lentiviral vector construct was provided by Dr. Peter Yingxiao Wang's laboratory in UC San Diego. For virus production, HEK293T cells were transfected with Lipofectamine 2000, the virus was harvested and concentrated using PEG-it solution according to manufacturer's instructions (System Biosciences). A healthy control iPS line was then infected with the PGK-EGFP lentivirus and the $EGFP^+$ cells were sorted by FACS (Aria, BD Biosciences) and replated on Matrigel plates. The brain cortical organoids were then generated from the sorted iPS cells.

### GSC-brain cortical organoid formation

$10^2$ to $10^5$ 3565, 387 or 1517 GFP-labeled GSCs were added per BCOs and allowed to proliferate. GFP-labeled GSCs were present inside brain cortical organoids as early as 24 hours post-addition. The experiments were conducted 2-3 weeks after adding GSCs onto the BCOs. Neurobasal media supplemented with 1X GEM21 (Gemini), 1% NEAA (Life Technologies), 1% Glutamax (Life Technologies) and 1% penicillin/streptomycin (Life Technologies) was used throughout the experiment.

### GSC organoid formation

Between $1 \times 10^5$ or $2 \times 10^5$ of 3565, 387 or 1517 GSCs were put per well in a 24-well plate under constant agitation at 95 rpm at 37°C in Neurobasal media supplemented with 1X GEM21 (Gemini), 1% NEAA (Life Technologies), 1% Glutamax (Life Technologies) and 1% penicillin/streptomycin (Life Technologies). The organoids started forming as early as 2 days after being put in suspension but were allowed to grow for 2-4 weeks before performing subsequent experiments.

### GBM organoid and BCOs *in vitro* ZIKV infection

GSC-BCOs and GSC organoids were infected with H/PAN/2016/BEI-259634, Panama 2016 and PRVABC59, Puerto Rico 2015 ZIKV strains for 2 hours at 37°C at MOI of 5 FFU/cell and then the media containing the virus were removed and fresh media were added, Neurobasal media supplemented with 1X GEM21 (Gemini), 1% NEAA (Life Technologies), 1% Glutamax (Life Technologies) and 1% penicillin/streptomycin (Life Technologies).

### Anti-integrin $\alpha_v\beta_5$ antibody treatment of GBM organoids

2- to 4-weeks-old GSC organoids were incubated with 50 μg/ml of the integrin $\alpha_v\beta_5$ antibody for 2-4 hours, then infected with PRVABC59 ZIKV strain for 2 hours at 37°C at an MOI of 5 FFU/cell. The media was then removed and fresh media containing 50 μg/ml of integrin $\alpha_v\beta_5$ antibody was added. The integrin $\alpha_v\beta_5$ antibody was added twice a week and GSC organoids were monitored for a month.

### Image analysis

To calculate the integrated density of GFP in GSC-brain cortical organoids, ImageJ software was used. Briefly, the channels were split and the integrated density of the GFP channel was measured by the software.

### Statistical analysis

All statistical analysis was performed using Prism 7.0 software (GraphPad). The number of animals and replicate experiments is specified in each figure legend. Sample size is similar to those reported in previous publications (Wang et al., 2017a). All grouped data were presented as mean ± SEM as indicated in the figure legends. Student's t test, one-way ANOVA with Tukey multiple comparison correction, and two-way ANOVA with the Bonferroni multiple comparison test were used to assess the significance of differences between groups. These tests were performed when the sample size was large enough to assume that the means were normally distributed or that the distribution of residuals was normal. For groups being statistically compared, variances in data were similar.

For animal survival analysis, Kaplan-Meier curves were generated and the Log-rank test was performed to assess statistical significance between groups.

## DATA AND CODE AVAILABILITY

Correlation between gene expression and patient survival was performed through analysis of The Cancer Genome Atlas (TCGA) and brain tumor datasets downloaded from the TCGA data portal (http://gliovis.bioinfo.cnio.es/) or NCBI GEO database. Raw data from enhancer profiling of primary glioma tissues were deposited at GSE101148. ChIP-seq data from Suvà et al. (2014) were accessed from the NCBI GEO database at GSE54792 and GSE17312.

**Cell Stem Cell, Volume *26***

## Supplemental Information

# Zika Virus Targets Glioblastoma Stem Cells through a SOX2-Integrin $\alpha_v\beta_5$ Axis

**Zhe Zhu, Pinar Mesci, Jean A. Bernatchez, Ryan C. Gimple, Xiuxing Wang, Simon T. Schafer, Hiromi I. Wettersten, Sungjun Beck, Alex E. Clark, Qiulian Wu, Briana C. Prager, Leo J.Y. Kim, Rekha Dhanwani, Sonia Sharma, Alexandra Garancher, Sara M. Weis, Stephen C. Mack, Priscilla D. Negraes, Cleber A. Trujillo, Luiz O. Penalva, Jing Feng, Zhou Lan, Rong Zhang, Alex W. Wessel, Sanjay Dhawan, Michael S. Diamond, Clark C. Chen, Robert J. Wechsler-Reya, Fred H. Gage, Hongzhen Hu, Jair L. Siqueira-Neto, Alysson R. Muotri, David A. Cheresh, and Jeremy N. Rich**

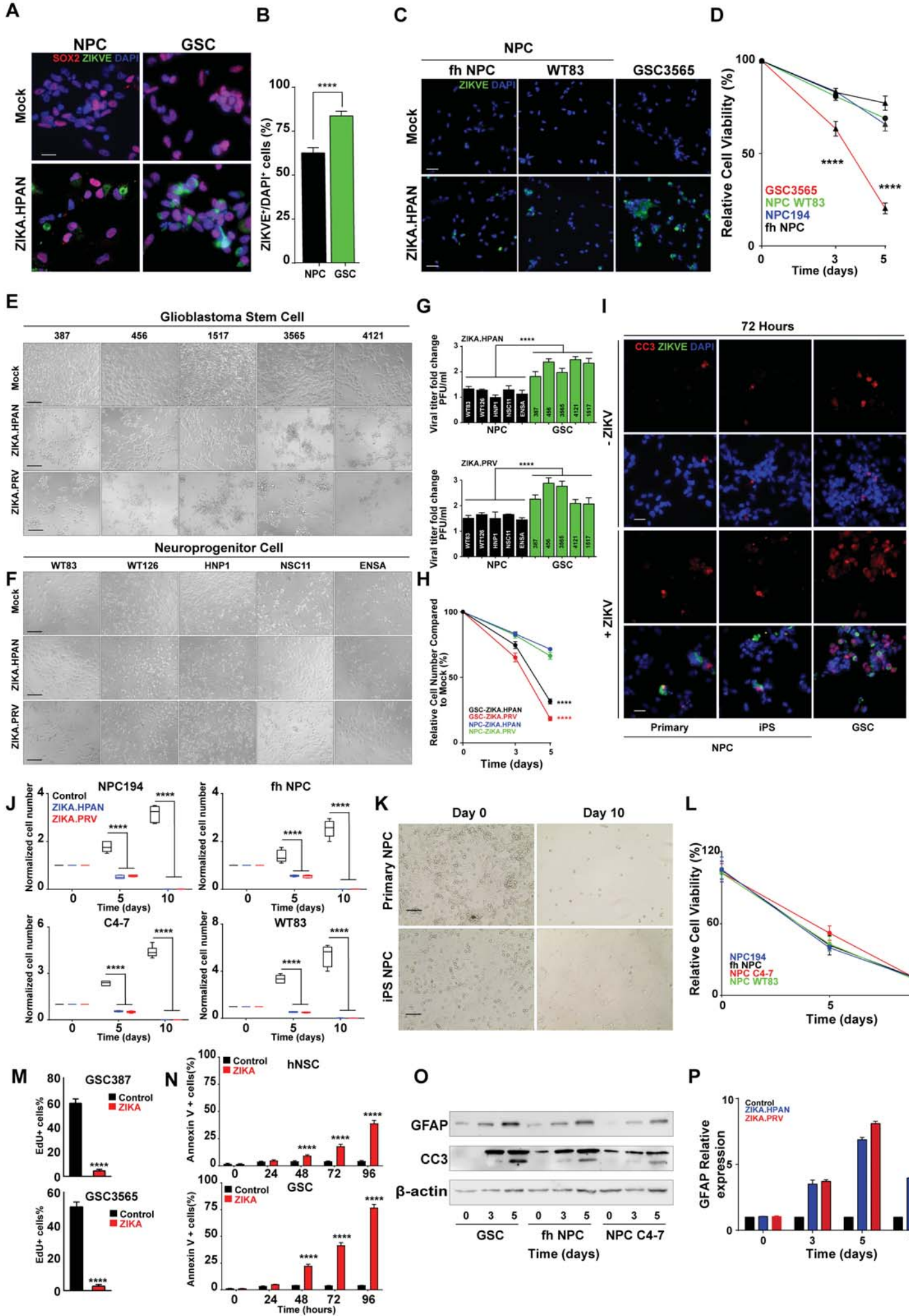
A
NPC
GSC
SOX2 ZIKVE DAPI
Mock
ZIKA.HPAN
B
ZIKVE+/DAPI+ cells (%)
100
75
50
25
0
****
NPC
GSC
C
NPC
fh NPC
WT83
GSC3565
ZIKVE DAPI
Mock
ZIKA.HPAN
D
Relative Cell Viability (%)
100
50
0
****
****
GSC3565
NPC WT83
NPC194
fh NPC
0
3
5
Time (days)
E
Glioblastoma Stem Cell
387
456
1517
3565
4121
Mock
ZIKA.HPAN
ZIKA.PRV
Neuroprogenitor Cell
WT83
WT126
HNP1
NSC11
ENSA
F
Mock
ZIKA.HPAN
ZIKA.PRV
G
ZIKA.HPAN
****
Viral titer fold change PFU/ml
WT83
WT126
HNP1
NSC11
ENSA
387
456
3565
4121
1517
NPC
GSC
ZIKA.PRV
****
H
Relative Cell Number Compared to Mock (%)
100
50
0
****
****
GSC-ZIKA.HPAN
GSC-ZIKA.PRV
NPC-ZIKA.HPAN
NPC-ZIKA.PRV
0
3
5
Time (days)
I
72 Hours
CC3 ZIKVE DAPI
- ZIKV
+ ZIKV
Primary
iPS
GSC
NPC
J
NPC194
Control
ZIKA.HPAN
ZIKA.PRV
Normalized cell number
****
Time (days)
fh NPC
C4-7
WT83
K
Day 0
Day 10
Primary NPC
iPS NPC
L
Relative Cell Viability (%)
120
60
0
NPC194
fh NPC
NPC C4-7
NPC WT83
0
5
10
Time (days)
M
GSC387
Control
ZIKA
EdU+ cells%
****
GSC3565
N
hNSC
Control
ZIKA
Annexin V + cells(%)
****
0
24
48
72
96
GSC
Time (hours)
O
GFAP
CC3
β-actin
0
3
5
GSC
fh NPC
NPC C4-7
Time (days)
P
Control
ZIKA.HPAN
ZIKA.PRV
GFAP Relative expression
10
5
0
0
3
5
7
Time (days)

**SUPPLEMENTAL FIGURES & LEGENDS**

**Supplemental Figure 1. refers to Figure 1. Comparative infection efficiency of ZIKV on GBM stem cells (GSCs) and neural precursor cells (NPCs).**

**A.** Primary NPCs and patient-derived GSCs underwent analysis for expression of the SOX2 neural progenitor marker (red) and the ZIKV envelope protein (ZIKV-E, green) under mock conditions or after ZIKV infection. Cell nuclei were imaged with DAPI. Scale bars, 20 μm.

**B.** The results of experiments in (A) were quantified. ****, $p < 0.0001$ two tailed Student's t-test.

**C.** 48 hours post ZIKV infection, patient-derived GSCs (GSC3565) and NPCs (primary and iPSC-derived) underwent immunostaining for ZIKV (green) with counterstaining by DAPI. GSCs displayed a greater fraction of $ZIKV^+$ cells than NPCs, with similar infection efficiency of primary and iPSC-derived NPCs. Scale bars, 40 μm.

**D.** The effects of ZIKV infection on cell viability was measured in GSCs and NPCs using the Cell Titer-Glo assay, revealing a greater loss of cell viability upon ZIKV infection in GSCs than either primary or iPSC-derived NPCs.

**E.** Representative brightfield images of GSCs (387, 456, 1517, 3565, and 4121) observed 5 days after infection with ZIKA.HPAN (MOI: 5 FFU/cell). Scale bars, 100 μm.

**F.** Representative brightfield images of NPCs (WT83, WT126, HNP1, NSC11, ENSA) observed 5 days after infection with ZIKA.HPAN (MOI: 5 FFU/cell). Scale bars, 100 μm.

**G.** Plaque assays were used to determine viral titers of NPCs and GSCs four days post infection with either ZIKA.HPAN (top) or ZIKA.PRV (bottom) at MOI of 0.1 FFU/cell. Values represent mean ± SEM and were normalized to day 0 levels as fold change. ****, $p < 0.0001$ by one-way ANOVA.

**H.** GSCs (GSC3565) and NPCs (NPC C4-7) were treated with mock conditions or infected with ZIKA.PRV or ZIKA.HPAN (MOI: 5 FFU/cell) with viability assayed over 5 days by CellTiter-Glo. Values represent mean ± SEM. ****, $p < 0.0001$ by one-way ANOVA.

**I.** Cell death of GSCs and NPCs upon ZIKV infection was measured by Cleaved Caspase-3 (CC3) staining, showing more apoptotic cells in GSCs than NPCs. Primary and iPSC-derived NPCs had similar rates of cell death upon ZIKV infection. Scale bars, 40 μm.

**J.** The effects of ZIKV on primary and iPSC-derived NPCs was measured over a time course. None of the NPCs displayed augmentation of proliferation, which would be expected with oncogenic transformation. ****, $p < 0.0001$ by one-way ANOVA.

**K.** Visualization of ZIKV infection on primary and iPSC-derived NPCs was assessed over a time course using brightfield images. No morphologic changes consistent with oncogenic transformation were detected over a time course. Scale bars, 40 μm.

**L.** Results in (K) were quantified.

**M.** GSC387 and GSC3565 were treated with Zika virus at MOI of 5 FFU/cell, 72 hours after infection, EdU labeling assay was used to label proliferating cells. Mock treated GSCs were used as control. **** $p < 0.0001$ by two tailed Student's t-test.

**N.** hNSCs and GSCs were infected with Zika at MOI of 5 FFU/cell, Annexin V labeling were used over a time course from 0 hour to 96 hours and quantified. Uninfected (control) and ZIKV-infected (Zika) cells were compared at each timepoint. Values represent mean ± SEM. ****, $p < 0.0001$ by one-way ANOVA.

**O.** Effects of ZIKV on cellular differentiation and apoptosis were measured by immunoblotting for GFAP and Cleaved Caspase-3 (CC3), respectively, in GSCs, primary NPCs and iPSC-derived NPCs over a time course.

**P.** The effects of ZIKV infection on cellular differentiation was measured by qPCR of GFAP over one week time course.

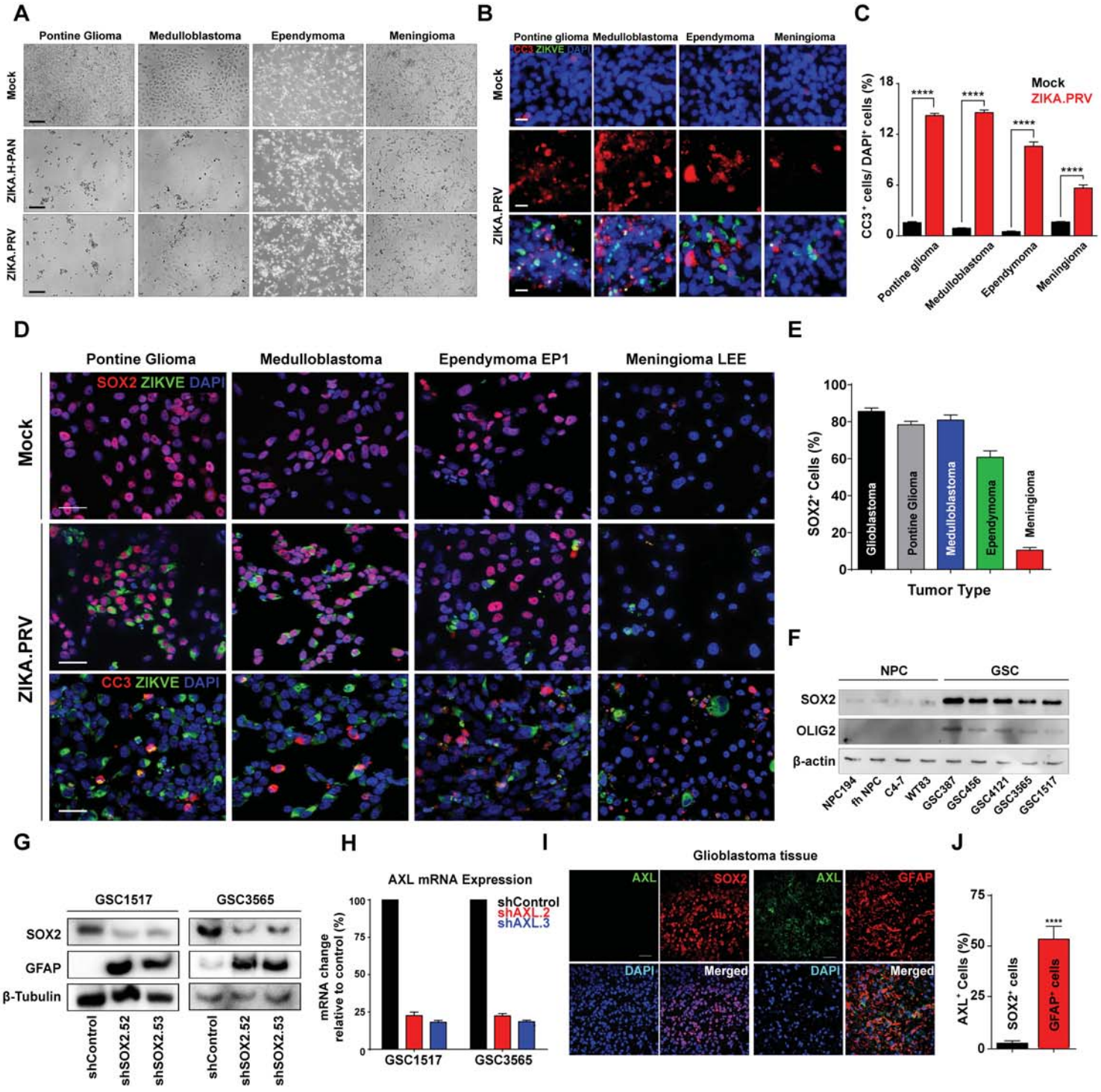
A
Pontine Glioma
Medulloblastoma
Ependymoma
Meningioma
Mock
ZIKA.H-PAN
ZIKA.PRV
B
Pontine glioma
Medulloblastoma
Ependymoma
Meningioma
CC3 ZIKVE DAPI
Mock
ZIKA.PRV
C
CC3+ cells/ DAPI+ cells (%)
Mock
ZIKA.PRV
****
Pontine glioma
Medulloblastoma
Ependymoma
Meningioma
D
Pontine Glioma
Medulloblastoma
Ependymoma EP1
Meningioma LEE
Mock
ZIKA.PRV
SOX2 ZIKVE DAPI
CC3 ZIKVE DAPI
E
SOX2+ Cells (%)
Glioblastoma
Pontine Glioma
Medulloblastoma
Ependymoma
Meningioma
Tumor Type
F
NPC
GSC
SOX2
OLIG2
β-actin
NPC194
fh NPC
C4-7
WT83
GSC387
GSC456
GSC4121
GSC3565
GSC1517
G
GSC1517
GSC3565
SOX2
GFAP
β-Tubulin
shControl
shSOX2.52
shSOX2.53
H
AXL mRNA Expression
shControl
shAXL.2
shAXL.3
mRNA change relative to control (%)
GSC1517
GSC3565
I
Glioblastoma tissue
AXL
SOX2
GFAP
DAPI
Merged
J
AXL+ Cells (%)
SOX2+ cells
GFAP+ cells

**Supplemental Figure S2, refers to Figure 2. SOX2 expression in NPCs, GSCs and different brain tumors, which mediates infection of GSCs through integrin $\alpha_v\beta_5$.**

**A.** Representative brightfield images of patient-derived cultures from pontine glioma, medulloblastoma, ependymoma and meningioma 5 days after mock infection or infection with one of two strains of Zika virus. MOI: 5 FFU/cell. Scale bars, 100 μm.

**B**. The baseline apoptotic index of cells derived from several brain tumor types was measured under mock conditions for apoptotic index (Cleaved Caspase-3, CC3, red). Total cell numbers were quantified through stained with DAPI. Scale bars, 20 μm.

**C.** Quantification of apoptotic cells upon ZIKV infection compared to mock in a spectrum of cells derived from different brain tumors. GBM and NPCs data were previously included. ****, $p < 0.0001$ by two tailed Student's t-test.

**D**. Representative confocal images of brain tumor cultures from (A) were immunostained 48 hours post ZIKA.PRV infection (MOI: 5 FFU/cell) for ZIKV envelope protein (ZIKVE, green), SOX2 or Cleaved Caspase-3 (red), and DAPI (blue). Scale bars, 100 μm.

**E**. Quantification of $SOX2^+$ cells in different brain tumor models used in (A) with two independent repeats.

**F.** Basal levels of precursor markers, SOX2 and OLIG2, were measured in primary NPCs, iPSC-derived NPCs, and patient-derived GSCs by immunoblotting. β-actin served as a loading control. GSCs expressed higher levels of SOX2 and OLIG2, whereas primary and iPSC-derived NPCs expressed similar levels.

**G.** Two patient-derived GSCs (GSC3565 and GSC1517) were transduced with either a control shRNA (shCONT) or one of two shRNAs targeting SOX2 (shSOX2.52 or shSOX2.53). 72 hours later, whole cell lysates were generated and resolved by SDS-PAGE with SOX2 and GFAP protein levels measured by immunoblotting. Tubulin was used as a loading control.

**H.** Two patient-derived GSCs (GSC3565 and GSC1517) were transduced with either a control shRNA (shCONT) or one of two shRNAs targeting AXL (shAXL.2, or shAXL.3). *AXL* levels were measured by qPCR and normalized to the values from shCONT.

**I.** Representative images of primary human GBM surgical biopsy specimens stained for AXL (green), SOX2 or GFAP (red) and DAPI (blue). Scale bars, 100 μm. (Right)

79 **J.** Quantification of $AXL^+$ cells in $SOX2^+$ or $GFAP^+$ cells in primary human GBM surgical biopsy
80 specimens. Values represent mean ± SEM. ****, $p < 0.0001$ by two tailed Student's t-test.

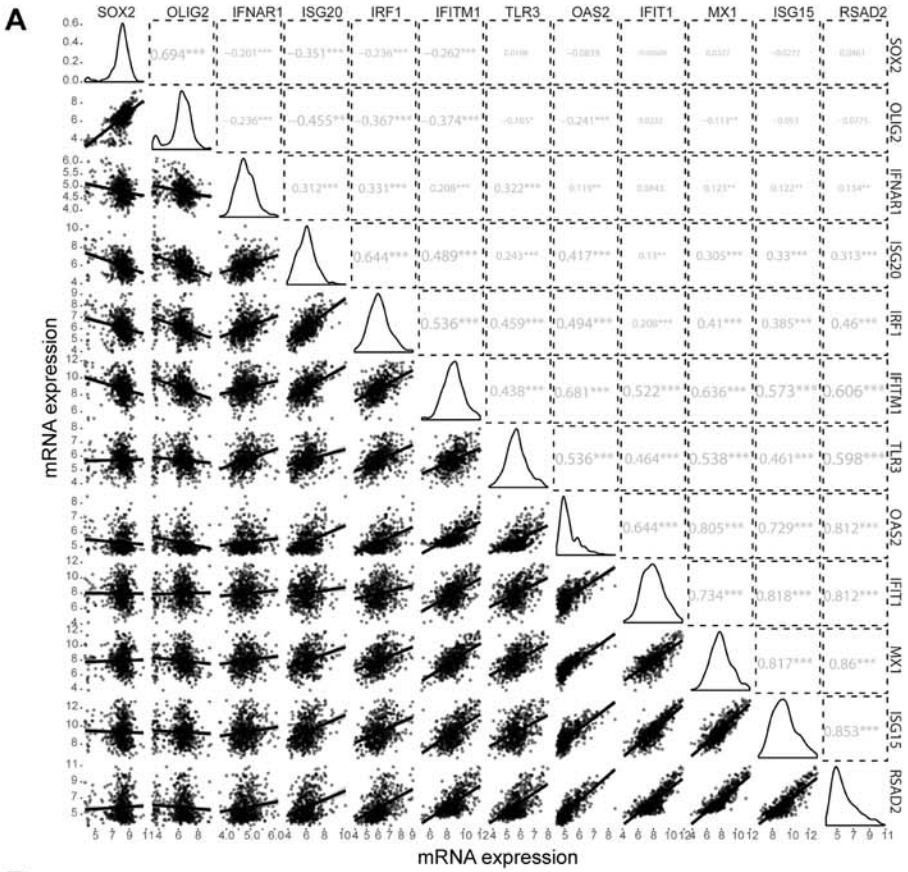
A
SOX2
OLIG2
IFNAR1
ISG20
IRF1
IFITM1
TLR3
OAS2
IFIT1
MX1
ISG15
RSAD2
mRNA expression
mRNA expression

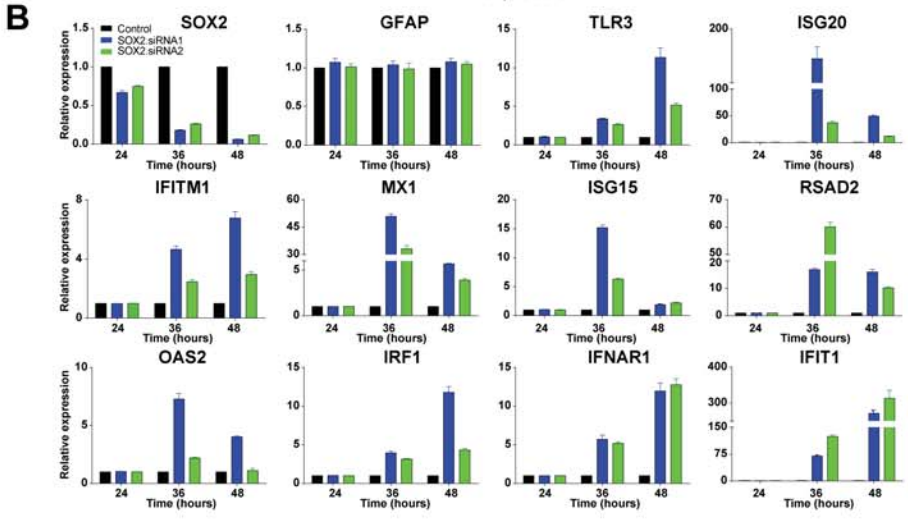
B
Control
SOX2.siRNA1
SOX2.siRNA2
SOX2
GFAP
TLR3
ISG20
IFITM1
MX1
ISG15
RSAD2
OAS2
IRF1
IFNAR1
IFIT1
Relative expression
Time (hours)

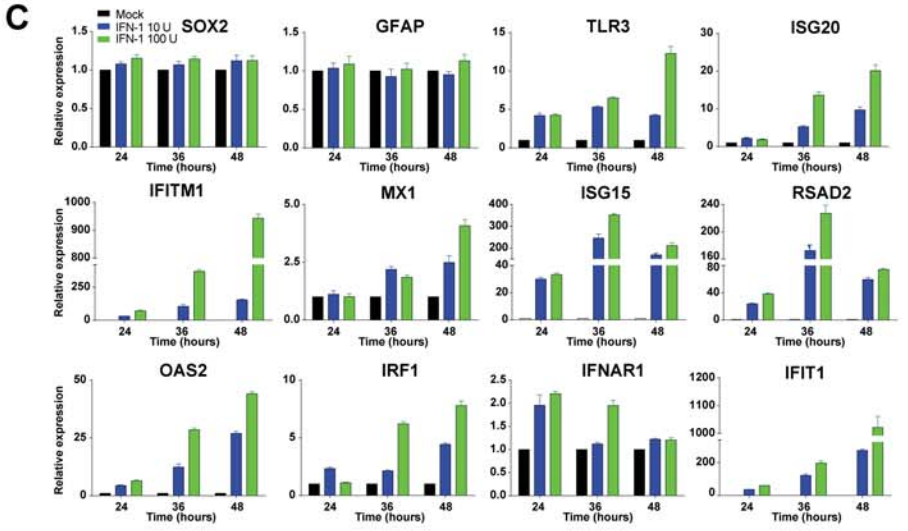
C
Mock
IFN-1 10 U
IFN-1 100 U
SOX2
GFAP
TLR3
ISG20
IFITM1
MX1
ISG15
RSAD2
OAS2
IRF1
IFNAR1
IFIT1
Relative expression
Time (hours)

**Supplemental Figure 3, refers to Figure 3. Targeting SOX2 induces ISG expression in GSCs.**

**A.** SOX2 expression inversely correlates with ISG expression in GBM. The GBM TCGA database was interrogated for correlation between mRNA expression levels of SOX2 and OLIG2 with ISGs. R-values are presented for each gene-gene correlation.

**B.** Gene expression time course in GSCs upon SOX2 targeting. GSCs without ZIKV infection were transduced with a non-targeting control siRNA or one of two, non-overlapping siRNAs. mRNA expression of SOX2, GFAP and several ISGs following knockdown of SOX2 were monitored over 24-48 hours. All experiments were performed in the absence of ZIKV infection.

**C.** mRNA expression level of SOX2, GFAP, and several ISGs in GSC3565 following treatment with interferon at two concentrations over a time course. Each experiment was performed in 3 technical replicates and two biological repeats.

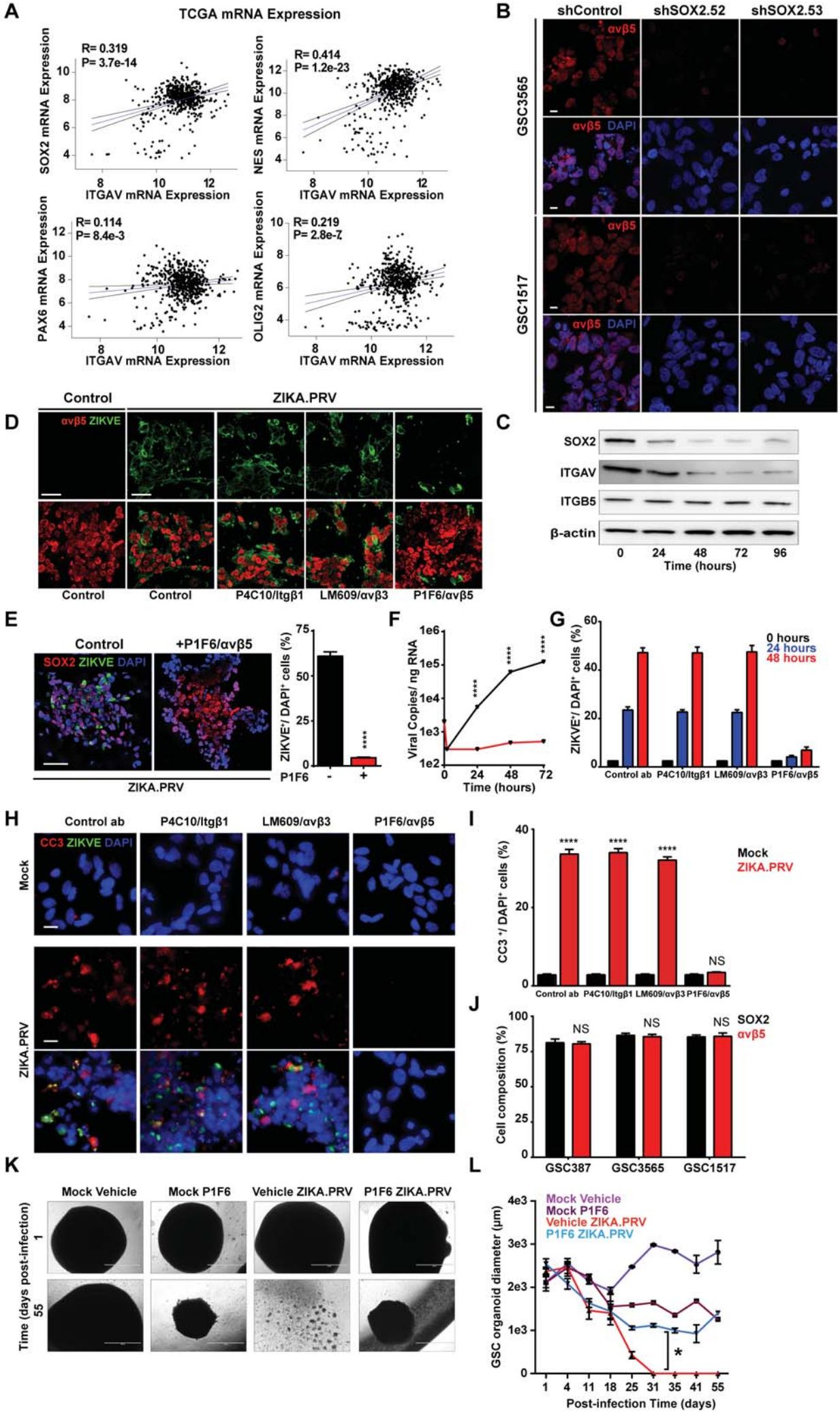
A
TCGA mRNA Expression
R= 0.319
P= 3.7e-14
SOX2 mRNA Expression
ITGAV mRNA Expression
R= 0.414
P= 1.2e-23
NES mRNA Expression
ITGAV mRNA Expression
R= 0.114
P= 8.4e-3
PAX6 mRNA Expression
ITGAV mRNA Expression
R= 0.219
P= 2.8e-7
OLIG2 mRNA Expression
ITGAV mRNA Expression
B
shControl
shSOX2.52
shSOX2.53
GSC3565
GSC1517
αvβ5
αvβ5 DAPI
C
SOX2
ITGAV
ITGB5
β-actin
0 24 48 72 96
Time (hours)
D
Control
ZIKA.PRV
αvβ5 ZIKVE
Control
Control
P4C10/Itgβ1
LM609/αvβ3
P1F6/αvβ5
E
Control
+P1F6/αvβ5
SOX2 ZIKVE DAPI
ZIKA.PRV
ZIKVE+/ DAPI+ cells (%)
P1F6 - +
F
Viral Copies/ ng RNA
Time (hours)
G
ZIKVE+/ DAPI+ cells (%)
0 hours
24 hours
48 hours
Control ab
P4C10/Itgβ1
LM609/αvβ3
P1F6/αvβ5
H
Control ab
P4C10/Itgβ1
LM609/αvβ3
P1F6/αvβ5
CC3 ZIKVE DAPI
Mock
ZIKA.PRV
I
CC3 +/ DAPI+ cells (%)
Mock
ZIKA.PRV
NS
Control ab
P4C10/Itgβ1
LM609/αvβ3
P1F6/αvβ5
J
Cell composition (%)
NS
SOX2
αvβ5
GSC387
GSC3565
GSC1517
K
Mock Vehicle
Mock P1F6
Vehicle ZIKA.PRV
P1F6 ZIKA.PRV
Time (days post-infection)
1
55
L
Mock Vehicle
Mock P1F6
Vehicle ZIKA.PRV
P1F6 ZIKA.PRV
GSC organoid diameter (μm)
Post-infection Time (days)

**Supplemental Figure 4, refers to Figure 4. Pharmacological Blocking of integrin $\alpha_v\beta_5$ attenuates ZIKV infection.**

**A.** Plots showing correlation of mRNA levels between *ITGAV* with *SOX2*, *NES*, *PAX6* and *OLIG2* in GBMs derived from the HG-U133A microarray dataset in The Cancer Genome Atlas (TCGA) GBM dataset.

**B.** Patient-derived GSCs were transduced with a non-targeting control shRNA (shControl) or one of two non-overlapping shRNAs targeting SOX2 (labeled shSOX2.52 and shSOX2.53). Transduced GSCs underwent immunofluorescent staining 72 hours for the integrin $\alpha_v\beta_5$ heterodimer (red) and DAPI (blue). Scale bars, 10 $\mu$m.

**C.** Immunoblots were performed for SOX2, integrin $\alpha_v$, and integrin $\beta_5$ over a 96 hours time course. $\beta$-actin was used as a loading control.

**D.** GSC3565 were cultured either under mock condition alone or with one of three blocking antibodies against integrins (Itg$\beta_1$, P4C10; $\alpha_v\beta_3$, LM609; $\alpha_v\beta_5$, P1F6 at 50 $\mu$g/ml for 2 hours at 4$^o$C) then infected with ZIKA.PRV (MOI: 5 FFU/cell). Representative confocal immunofluorescent images for integrin $\alpha_v\beta_5$ (red) or ZIKV envelope protein (ZIKVE, green) were shown. Scale bars, 100 $\mu$m.

**E.** GSC3565 were cultured either under mock condition or with a neutralizing antibody against $\alpha_v\beta_5$ (P1F6 at 50 $\mu$g/ml for 2 hours at 4$^o$C) then infected with ZIKA.PRV (MOI: 5 FFU/cell). (Left) Representative confocal immunofluorescent images after 48 hours infection for ZIKV envelope protein (ZIKVE, green), SOX2 (red) and DAPI (blue) were shown. (Right) ZIKV$^+$ cells in GSCs subjected to mock conditions or with neutralizing antibodies against integrin $\alpha_v\beta_5$ were shown. Values represent mean ± SEM. ****, $p < 0.0001$ by two tailed Student's t-test. Scale bars, 100 $\mu$m.

**F.** GSC3565 were cultured either under mock condition or with a neutralizing antibody against integrin $\alpha_v\beta_5$ (P1F6 at 50 $\mu$g/ml for 2 hours at 4$^o$C) then infected with ZIKA.PRV (MOI: 0.1 FFU/cell). Kinetics of viral RNA copy number was measured by qRT-PCR over a 72 hours time course. Values represent mean ± SEM. ****, $p < 0.0001$ by one-way ANOVA.

**G.** Quantification of ZIKV$^+$ cells in GSC3565 using different integrin antibody treatments according to different time points.

**H.** Patient-derived GSCs were cultured under mock (upper panel) or ZIKV (lower panel) conditions with IgG control or blocking antibodies against several integrins (pan-$\beta_1$, $\alpha_v\beta_3$, or $\alpha_v\beta_5$). GSCs were immunostained for ZIKVE (green), CC3 (red) and DAPI (blue). Scale bars, 20 μm.

**I.** Quantification of $CC3^+$ cells upon ZIKV infection compared to mock control, after incubation with antibodies targeting several integrins. ****, $p < 0.0001$, by two tailed Student's t-test.

**J.** Quantification of $\alpha_V\beta_5$ and SOX2 cells in total DAPI cells by GSC387, GSC3565 and GSC1517 models. The percentages were similar between $\alpha_V\beta_5^+$ and $SOX2^+$ cells (NS, no significance).

**K.** Organoids were derived from GSC3565 and subjected to treatment with mock condition, a blocking antibody against integrin $\alpha_v\beta_5$ (P1F6 at 50 μg/ml twice a week), ZIKA.PRV infection (MOI: 5 FFU/cell), or the combined antibody and ZIKV treatment. Brightfield images were taken over a time course until day 55. N = 5. Scale bars, 1 mm.

**L.** GSC-derived organoids from (H) were assayed for their diameter over a time course. Values represent mean ± SEM. *, $p < 0.05$ by two-way ANOVA.

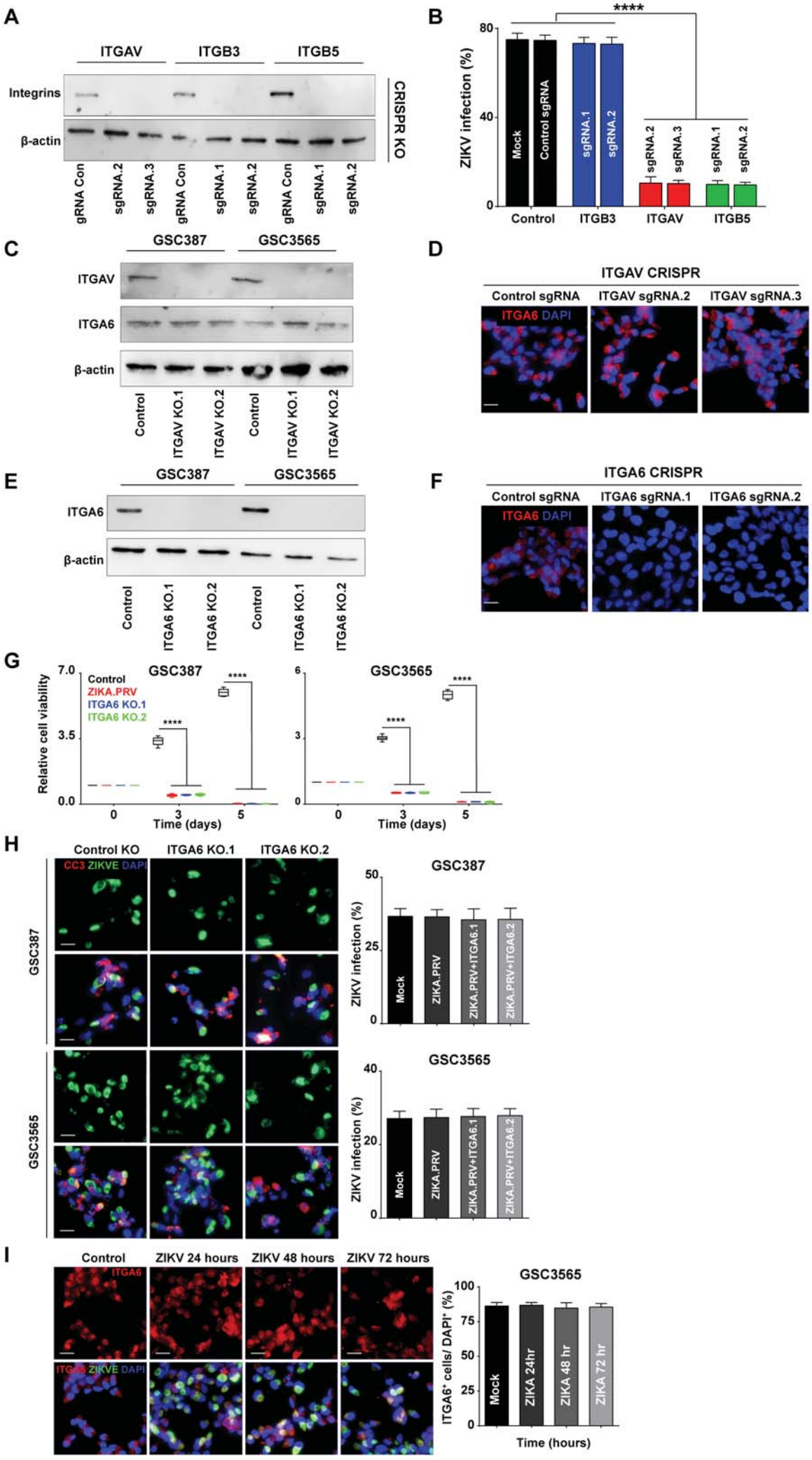
A
ITGAV
ITGB3
ITGB5
Integrins
β-actin
CRISPR KO
gRNA Con
sgRNA.2
sgRNA.3
gRNA Con
sgRNA.1
sgRNA.2
gRNA Con
sgRNA.1
sgRNA.2
B
****
ZIKV infection (%)
80
40
0
Mock
Control sgRNA
sgRNA.1
sgRNA.2
sgRNA.2
sgRNA.3
sgRNA.1
sgRNA.2
Control
ITGB3
ITGAV
ITGB5
C
GSC387
GSC3565
ITGAV
ITGA6
β-actin
Control
ITGAV KO.1
ITGAV KO.2
Control
ITGAV KO.1
ITGAV KO.2
D
ITGAV CRISPR
Control sgRNA
ITGAV sgRNA.2
ITGAV sgRNA.3
ITGA6 DAPI
E
GSC387
GSC3565
ITGA6
β-actin
Control
ITGA6 KO.1
ITGA6 KO.2
Control
ITGA6 KO.1
ITGA6 KO.2
F
ITGA6 CRISPR
Control sgRNA
ITGA6 sgRNA.1
ITGA6 sgRNA.2
ITGA6 DAPI
G
GSC387
GSC3565
Control
ZIKA.PRV
ITGA6 KO.1
ITGA6 KO.2
Relative cell viability
7.0
3.5
0.0
6
3
0
****
****
****
****
0
3
5
0
3
5
Time (days)
Time (days)
H
Control KO
ITGA6 KO.1
ITGA6 KO.2
GSC387
GSC3565
CC3 ZIKVE DAPI
GSC387
ZIKV infection (%)
50
25
0
Mock
ZIKA.PRV
ZIKA.PRV+ITGA6.1
ZIKA.PRV+ITGA6.2
GSC3565
ZIKV infection (%)
40
20
0
Mock
ZIKA.PRV
ZIKA.PRV+ITGA6.1
ZIKA.PRV+ITGA6.2
I
Control
ZIKV 24 hours
ZIKV 48 hours
ZIKV 72 hours
ITGA6
ITGA6 ZIKVE DAPI
GSC3565
ITGA6+ cells/ DAPI+ (%)
100
75
50
25
0
Mock
ZIKA 24hr
ZIKA 48 hr
ZIKA 72 hr
Time (hours)

**Supplemental Figure 5, refers to Figure 5. CRISPR-mediated targeting of ITGAV and ITGB5 integrins, but not ITGB3 attenuates ZIKV infection of GSCs**

**A.** Patient-derived GSCs were transduced with sgRNAs for a non-targeting control sequence (Control sgRNA) or one of two sgRNAs targeting selected integrins. Whole cell lysates from transduced GSCs were collected and resolved by SDS-PAGE. Immunoblotting confirmed successful knockout of integrins at the protein level.

**B.** GSC3565 under mock conditions or transduced with indicated sgRNAs were examined for ZIKV infection efficiency.

**C-F**. Patient-derived GSCs (GSC387 and GSC3565) were transduced with a non-targeting control sgRNA or one of two sgRNAs targeting either (E,F) ITGA6 or (C, D) ITGAV. A and B. ITGA6 and/or ITGAV expression was assessed by immunoblotting. β-actin was used as a loading control. D and F. ITGA6 expression was analyzed by immunofluorescence after targeting (F) ITGA6 or (D) ITGAV. DAPI (blue) was used as counterstain. Scale bars, 20 μm.

**G.** Patient-derived GSCs were either infected with ZIKV or transduced with sgRNAs targeting ITGA6. The CellTiter-Glo assay was performed over a time course.

**H.** Patient-derived GSCs were transduced with either a non-targeting control sgRNA or one of two, non-overlapping sgRNAs targeting ITGA6. Left, immunostaining for ZIKVE (green), CC3 (red) with DAPI (blue). Right, quantification of $ZIKVE^+$ cells in $DAPI^+$ cells.

**I.** Left, immunostaining for ZIKV (green), ITGA6 (red) and DAPI (blue). Right, quantification of $ITGA6^+$ cells in $DAPI^+$ cells. Scale bars, 20 μm. Values represent mean ± SEM. ****, $p < 0.0001$ by one-way ANOVA.

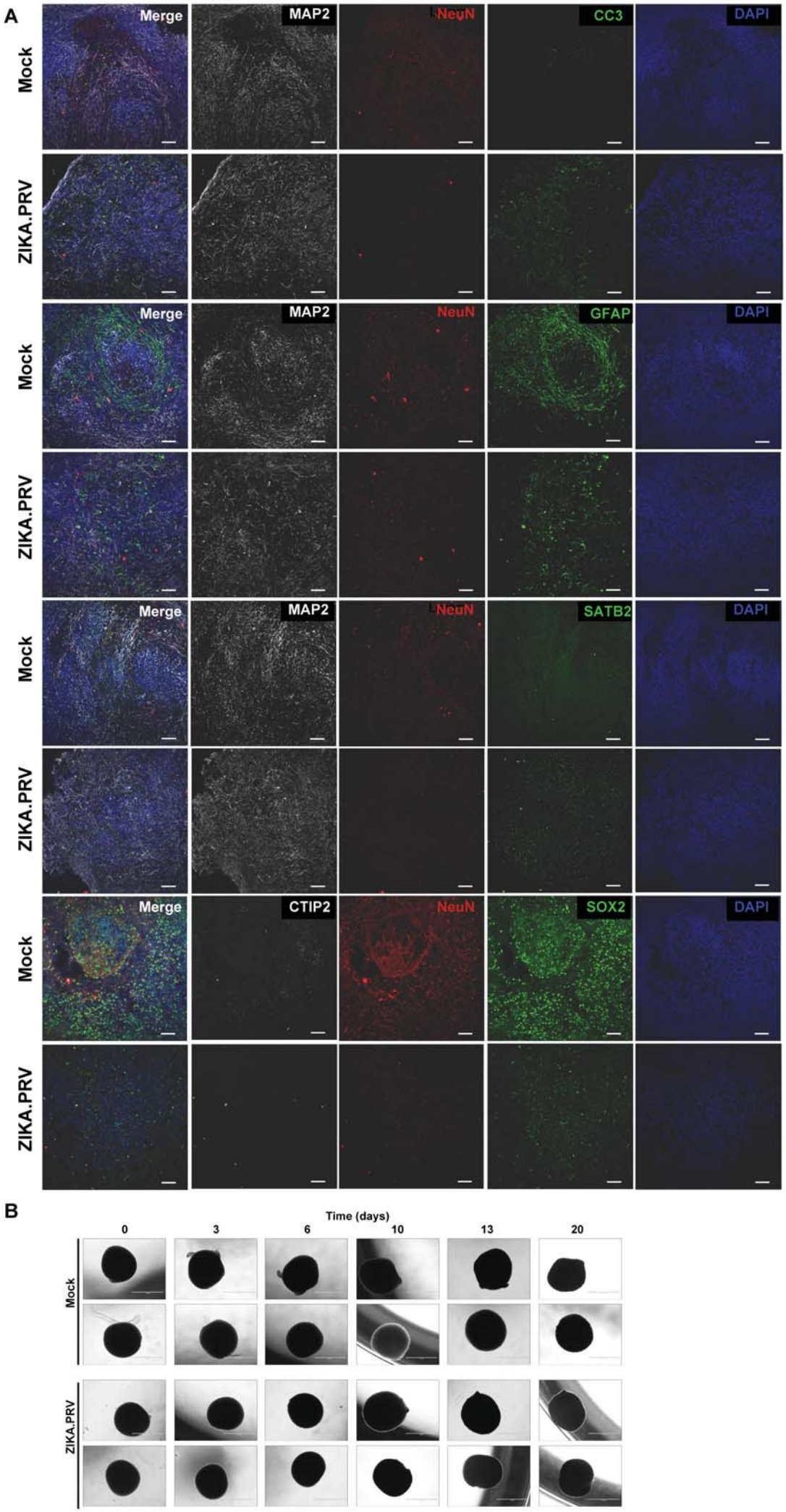
A
Merge
MAP2
NeuN
CC3
DAPI
Mock
ZIKA.PRV
Merge
MAP2
NeuN
GFAP
DAPI
Mock
ZIKA.PRV
Merge
MAP2
NeuN
SATB2
DAPI
Mock
ZIKA.PRV
Merge
CTIP2
NeuN
SOX2
DAPI
Mock
ZIKA.PRV
B
Time (days)
0
3
6
10
13
20
Mock
ZIKA.PRV

**Supplemental Figure 6, refers to Figure 6. Effects of ZIKV on normal brain cortical organoid cellular types and size.**

**A.** Representative images of mock or ZIKV-infected brain cortical organoids immunostained with MAP2, NeuN, CC3, GFAP, CTIP2, SATB2, SOX2 and DAPI. Scale bar = 100μm.

**B.** Representative brightfield images of brain cortical organoids derived from induced pluripotent stem cells that were subjected to mock conditions or infected with ZIKA.PRV (MOI: 5 FFU/cell) over a time course until 20 days post infection. Scale bar, 1 mm.

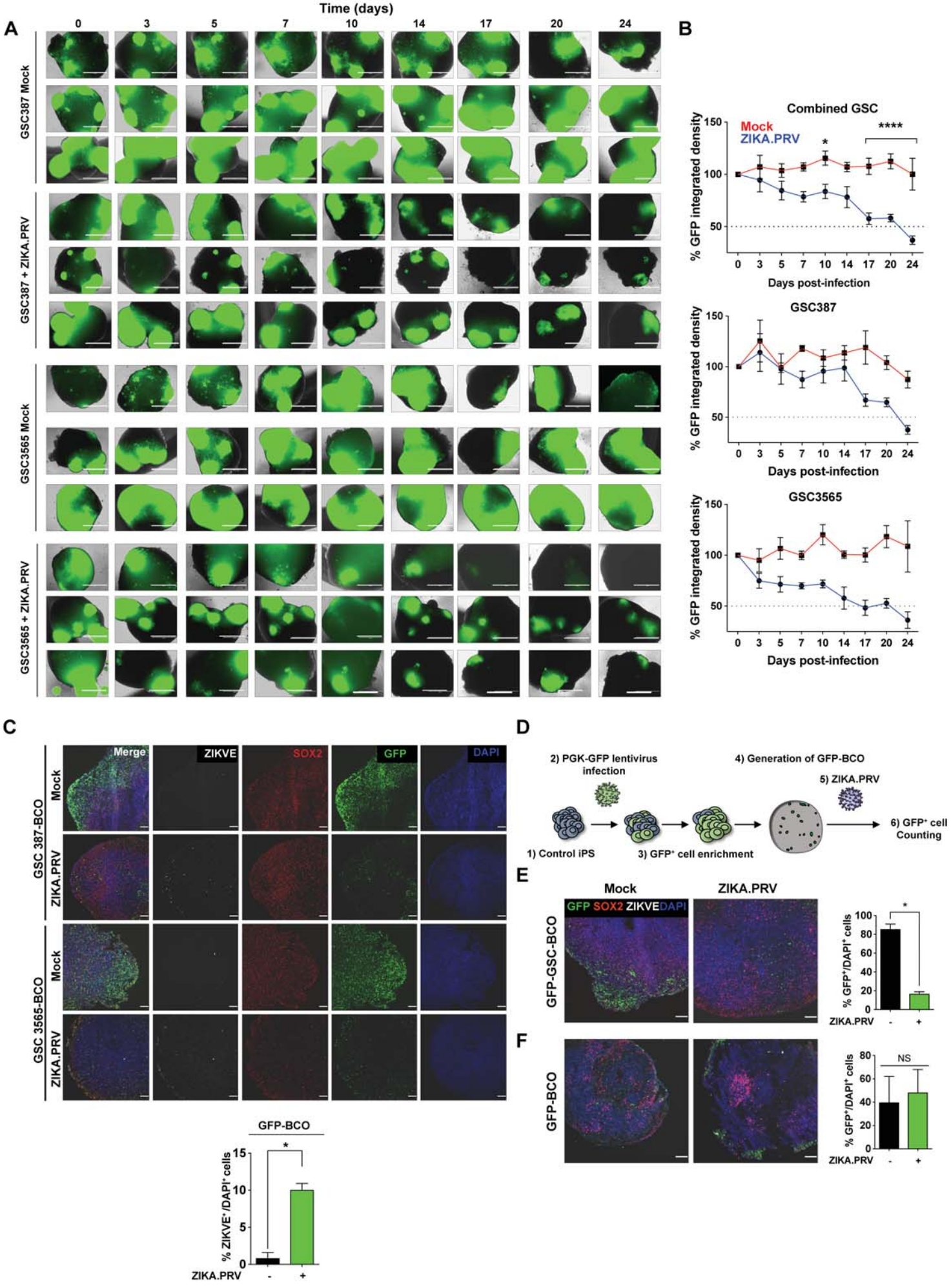
A
Time (days)
0
3
5
7
10
14
17
20
24
GSC387 Mock
GSC387 + ZIKA.PRV
GSC3565 Mock
GSC3565 + ZIKA.PRV
B
Combined GSC
Mock
ZIKA.PRV
*
****
% GFP integrated density
Days post-infection
GSC387
GSC3565
C
Merge
ZIKVE
SOX2
GFP
DAPI
GSC 387-BCO
GSC 3565-BCO
Mock
ZIKA.PRV
GFP-BCO
% ZIKVE+ /DAPI+ cells
ZIKA.PRV
D
2) PGK-GFP lentivirus infection
4) Generation of GFP-BCO
5) ZIKA.PRV
1) Control iPS
3) GFP+ cell enrichment
6) GFP+ cell Counting
E
Mock
ZIKA.PRV
GFP-GSC-BCO
GFP SOX2 ZIKVE DAPI
% GFP+/DAPI+ cells
F
GFP-BCO
NS

**Supplemental Figure 7, refers to Figure 7. ZIKV infection preferentially targets GBM in GSC-brain cortical organoids models**

**A.** Brain cortical organoids were derived from induced pluripotent stem cells then confronted with GFP-labeled GSCs (GSC387 or GSC3565), permitting integration. Brightfield images showing GSC-brain cortical organoids after being subjected to mock conditions or infection with ZIKA.PRV (MOI: 5 FFU/cell) were taken over a time course until day 24. Scale bars, 1 mm.

**B.** GFP integrated density shown in A was measured using ImageJ software. Mock infection vs. ZIKA.PRV infection. Day 10: $p = 0.03$; *, $p < 0.05$; days 17, 20 and 24: ****, $p < 0.0001$ by two-way ANOVA.

**C.** Representative images of GSC-brain cortical organoids with or without ZIKV immunostained with NS1, staining for ZIKV, SOX2, GFP and DAPI (GSC387 top panel, GSC3565 bottom panel). Scale bars, 50 μm. The quantification of $ZIKV^+$ (quantified by NS1 immunostaining) within all cells and $ZIKV^+$ cells within the $GFP^+$ cells in GSC-brain cortical organoid (BCO) mock vs GSC-BCO ZIKV respectively. Significance was assessed by two tailed Student's t-test, experiments were performed in two batches with 12 organoids per group, per batch (*$p < 0.05$).

**D.** Schematic of GFP-brain cortical organoid (BCO) generation. Control iPS were firstly infected with a lentivirus containing the PGK-GFP vector, then the $GFP^+$ cells were enriched using FACs sorting to generate brain cortical organoids by sorted GFP-iPS. These organoids were then infected with ZIKA.PRV (MOI: 5 FFU/cell) and the $GFP^+$ cells were counted.

**E.** GFP-BCO and GFP-GSC-BCO were immunostained with SOX2, ZIKVE and DAPI antibodies with or without ZIKV. Quantification of $GFP^+$ cells in GFP-brain cortical organoid (BCO) with or without ZIKV infection respectively. Scale bars, 100 μm. Significance was assessed by two tailed Student's t-test, experiments were performed in two batches with 12 organoids per group for each GSCs cell line (GSC387 and GSC3565), per batch (*$p < 0.05$; NS, no significance). Experiments were performed in two batches with 12 organoids per group, per batch.

196 **Table S1. All Cell lines used in the manuscript.**

197

| Glioblastoma Stem Cell Model or Tissue | Patient Age (Years) | Patient Sex | Tumor Grade |
|---|---|---|---|
| **GSC387** | 76 | Female | Glioblastoma (Grade IV) |
| **GSC3565** | 32 | Male | Glioblastoma (Grade IV) |
| **GSC23** | 63 | Male | Recurrent Glioblastoma (Grade IV) |
| **MGG8** | Restricted by Institutional Requirements | Female | Glioblastoma (Grade IV) |
| **GSC1517** | 54 | Female | Glioblastoma (Grade IV) |
| **3752** | 5 | Female | Pontine Glioma(Milde *et al.*, 2011) |
| **007** | 6 | unknown | Pontine Glioma |
| **CH-157MN** | 41 | Female | Meningioma |
| **IOMM-Lee** | 61 | Male | Meningioma |
| **DAOY** | 4 | Male | Medulloblastoma |
| **D283** | 6 | Male | Medulloblastoma |
| **HDMB03** | 3 | Male | Medulloblastoma |
| **D341** | 3.5 | Male | Medulloblastoma |

198

199

200 **Table S2. Primers and Oligos for PCR and shRNA assay.**

| Gene Name | Forward Primer | Reverse Primer |
|---|---|---|
| SOX2 | 5’-GCCGAGTGGAAACTTTTGTCG-3’ | 5’-GGCAGCGTGTACTTATCCTTCT-3’ |
| OLIG2 | 5’-CCAGAGCCCGATGACCTTTTT-3’ | 5’-CACTGCCTCCTAGCTTGTCC-3’ |
| GFAP | 5’-CTGCGGCTCGATCAACTCA-3’ | 5’-TCCAGCGACTCAATCTTCCTC-3’ |
| ITGAV | 5’-ATCTGTGAGGTCGAAACAGGA-3’ | 5’-TGGAGCATACTCAACAGTCTTTG-3’ |
| ITGB1 | 5’-CCTACTTCTGCACGATGTGATG-3’ | 5’-CCTTTGCTACGGTTGGTTACATT-3’ |
| ITGB3 | 5’-GTGACCTGAAGGAGAATCTGC-3’ | 5’-CCGGAGTGCAATCCTCTGG-3’ |
| ITGB5 | 5’-TCTCGGTGTGATCTGAGGG-3’ | 5’-TGGCGAACCTGTAGCTGGA-3’ |
| ITGB6 | 5’-TCCATCTGGAGTTGGCGAAAG-3’ | 5’-TCTGTCTGCCTACACTGAGAG-3’ |
| ITGB8 | 5’-ACCAGGAGAAGTGTCTATCCAG-3’ | 5’-CCAAGACGAAAGTCACGGGA-3’ |
| TLR3 | 5’-TTGCCTTGTATCTACTTTTGGGG-3’ | 5’-TCAACACTGTTATGTTTGTGGGT-3’ |
| ISG20 | 5’-CTCGTTGCAGCCTCGTGAA-3’ | 5’-CGGGTTCTGTAATCGGTGATCTC-3’ |
| IFITM1 | 5’-CCAAGGTCCACCGTGATTAAC-3’ | 5’-ACCAGTTCAAGAAGAGGGTGTT-3’ |
| MX1 | 5’-GTTTCCGAAGTGGACATCGCA-3’ | 5’-CTGCACAGGTTGTTCTCAGC-3’ |
| ISG15 | 5’-CGCAGATCACCCAGAAGATCG-3’ | 5’-TTCGTCGCATTTGTCCACCA-3’ |
| RSAD2 | 5’-TGGGTGCTTACACCTGCTG-3’ | 5’-GAAGTGATAGTTGACGCTGGTT-3’ |
| OAS2 | 5’-CTCAGAAGCTGGGTTGGTTTAT-3’ | 5’-ACCATCTCGTCGATCAGTGTC-3’ |
| IRF1 | 5’-ATGCCCATCACTCGGATGC-3’ | 5’-CCCTGCTTTGTATCGGCCTG-3’ |
| IFNAR1 | 5’-AACAGGAGCGATGAGTCTGTC-3’ | 5’-TGCGAAATGGTGTAAATG AGTCA-3’ |

| | | |
|---|---|---|
| IFIT1 | 5’-TTGATGACGATGAAATGCCTGA-3’ | 5’-CAGGTCACCAGACTCCTCAC-3’ |
| ZIKV835 | 5’-TTGGTCATGATACTGCTGATTGC-3’ | |
| ZIKV911c | 5’-CCTTCCACAAAGTCCCTATTGC-3’ | |
| ZIKV860FAM | 5’-CGGCATACAGCATCAGGTGCATAG GAG-3’ | |
| **Gene Name and start site of shRNA targeting** | **shRNA sequence** | |
| ShAXL-2 | 5’-CCGGCGTGGAGAACAGCGAGATTTACTCGAGTAAATCTCGCTGTTCTCCACGTTTTTTG-3’ | |
| ShAXL-3 | 5’-CCGGCCTAAGCATCTAAGTTATAAGCTCGAGCTTATAACTTAGATGCTTAGGTTTTTTG-3’ | |
| ShSOX2-52 | 5'-CCGGGAAGAAGGATAAGTACACGCTCTCGAGAGCGTGTACTTATCCTTCTTCTTTTT-3' | |
| ShSOX2-53 | 5'-CCGGCTGCCGAGAATCCATGTATATCTCGAGATATACATGGATTCTCGGCAGTTTTT-3' | |
| ShITGB1-1 | 5’-CCGGGCCTTGCATTACTGCTGATATCTCGAGATATCAGCAGTAATGCAAGGCTTTTTG-3’ | |
| ShITGB1-2 | 5’-CCGGGCCCTCCAGATGACATAGAAACTCGAGTTTCTATGTCATCTGGAGGGCTTTTTG-3’ | |
| ShITGB3-3 | 5’-CCGGGTCGTCAGATTCCAGTACTATCTCGAGATAGTACTGGAATCTGACGACTTTTT-3’ | |
| ShITGB3-2 | 5’-CCGGCCACGTCTACCTTCACCAATACTCGAGTATTGGTGAAGGTAGACGTGGTTTTT-3’ | |
| ShITGB5-1 | 5’-CCGGGGCTCGCAGGTCTCAACATATCTCGAGATATGTTGAGACCTGCGAGCCTTTTTG-3’ | |
| ShITGB5-3 | 5’-CCGGGGATCAGCCTGAGGATCTTAACTCGAGTTAAGATCCTCAGGCTGATCCTTTTTG-3’ | |
| ShITGB6-1 | 5’-CCGGGCCTCCAAACATTCCCATGATCTCGAGATCATGGGAATGTTTGGAGGCTTTTTG-3’ | |
| ShITGB6-2 | 5’-CCGGCCATTGACAAATGATGCTGAACTCGAGTTCAGCATCATTTGTCAATGGTTTTTG-3’ | |
| ShITGB8-1 | 5’-CCGGGCTCAGTTGATTCAATAGAATCTCGAGATTCTATTGAATCAACTGAGCTTTTTG-3’ | |
| ShITGB8-2 | 5’-CCGGCGAGCAATGATGAAGTTCTTTCTCGAGAAAGAACTTCATCATTGCTCGTTTTTG-3’ | |

**Table S3. ChIP-PCR primers, refers to Figure 3.**

| Target Name | Target Region (hg19) | Forward Primer | Reverse Primer |
|---|---|---|---|
| Negative Control #1 | chr11:35,158,607-35,159,750 | AGGGTGAGGGCTCTGAAGAT | GCCATCCCCCTATGCATTCA |
| SOX2 Enhancer Primer #1 | chr2:187,477,736-187,478,211 | AGGACCACTGGAATTGCTCA | GCAGAACCAGAGGAAAACAGG |
| SOX2 Enhancer Primer #2 | chr2:187,477,736-187,478,211 | GGCCTGTATTCTTTGTGCTGC | AGCTCATTTCACTGGGATTGGT |

**Table S4. sgRNA sequences and plasmids used in the manuscript**

| Target Name | Forward Sequence | CRISPR Type |
|---|---|---|
| Non-Targeting | CACCGCTCTGCTGCGGAAGGATTCG | LentiCrisprV2 (Addgene #52961) |
| ITGAV Gene 1 | GGAATTGATAGCGTATCTGC | LentiCrisprV2 (Addgene #52961) |

| | | |
|---|---|---|
| ITGAV Gene 2 | AGGCAATAGAGATTATGCCA | LentiCrisprV2 (Addgene #52961) |
| ITGAV Gene 3 | GCCTTAACAATCAATGTCAG | LentiCrisprV2 (Addgene #52961) |
| ITGB3 Gene 1 | GCGAGGTGAGCCCAGAGGCA | LentiCrisprV2 (Addgene #52961) |
| ITGB3 Gene 2 | TCACAGCGAGGTGAGCCCAG | LentiCrisprV2 (Addgene #52961) |
| ITGB3 Gene 3 | TTCTCCTTCAGGTCACAGCG | LentiCrisprV2 (Addgene #52961) |
| ITGB5 Gene 1 | TTTTTCCCTGCCTAGGACTT | LentiCrisprV2 (Addgene #52961) |
| ITGB5 Gene 2 | ACCGAGAGGTGATGGACCGT | LentiCrisprV2 (Addgene #52961) |
| ITGB5 Gene 3 | CACCGAGAGGTGATGGACCG | LentiCrisprV2 (Addgene #52961) |
| ITGA6 Gene 1 | CGGATCGAGTTTGATAACGA | LentiCrisprV2 (Addgene #52961) |
| ITGA6 Gene 2 | TTTCCAGTTATAAGTACCCG | LentiCrisprV2 (Addgene #52961) |
| ITGA6 Gene 3 | GGAGCTCCGTATGATGACTT | LentiCrisprV2 (Addgene #52961) |

206